Amorphous Metal-Free Organic Phosphors for Sensor Applications

by

Dongwook Lee

A dissertation submitted in partial fulfillment
of the requirements for the degree of
Doctor of Philosophy
(Macromolecular Science and Engineering)
in The University of Michigan
2015

Doctoral Committee:

Associate Professor Jinsang Kim, Chair
Professor L. Jay Guo
Professor John Kieffer
Associate Professor Anne McNeil

ACKNOWLEDGEMENTS

First, I would like to thank my advisor, Prof. Jinsang Kim, for his insightful advice on research and writing. I could not have achieved my research products without his support. He always encouraged me and suggested prospective ideas when I was stuck in my experiments. My scientific writing improved a lot from his intense revision and advice. I cannot imagine having a better advisor for my Ph.D. study. I would also like to thank committee members, Prof. John Kieffer, Prof. L. Jay Guo, and Prof. Anne McNeil. Their comments were helpful in shaping research ideas and refining my dissertation even though I was sometimes challenged from their keen questions.

I would like to express my gratitude to my employer LG Chem., and Dr. Inseok Hwang for allowing me to pursue my Ph.D. and warm support. I also appreciate Prof. Chongrae Park and Prof. Hyuk Yu for their warm recommendation and encouragement.

I thank my former lab member, Dr. Eun Jeong Jeong, for her assistance and knowledge in organic synthesis. I also thank Dr. David Bilby and Dr. Sungbaek Seo for their contribution to the lab. They always showed great ownership and sacrificed them in order to better the lab environment. I thank Andrew Phillips and Apoorv Shanker for revising my poor English. Also, I thank other lab members and Korean friends for their helpful advice and pleasure. I really enjoyed my life in Ann Arbor with them.

Last, but most importantly, I must thank my family. My precious wife, Youngah Lee, sacrificed a lot and allowed me to spend much time in the lab. My lovely daughter Seohyung and

sweet son Joonhyung made me smile. I could overcome difficulties due to their warmness whenever I was exhausted and frustrated. I feel sorry that I didn't spend much time with them and swear that I should from now. I must also thank my parents and parents-in-law for their warm encouragements. I specially thank Prof. Sung Kyun Park and his family for sharing joy and sadness. I would like to thank God and Korean bible study group "Moses". I learned love and wisdom from their heart and prayer.

TABLE OF CONTENTS

CHAPTER 3. Room Temperature Phosphorescence of Metal-Free Organic Materials in Amorphous Polymer Matrices……………................... 38

CHAPTER 4. Tailoring Intermolecular Interactions for Efficient Room Temperature Phosphorescence from Purely Organic Materials in Amorphous Polymer Matrices……………………….................... 55

LIST OF FIGURES

LIST OF TABLES

ABSTRACT

Phosphorescent organic light-emitting diodes (PhOLED) are promising for many applications such as display and solid-state lighting because they can reach 100% theoretical internal quantum efficiency. However, most organic materials only exhibit fluorescence because long-lived excited electrons are usually consumed as a form of heat by vibration in a shorter time regime. Therefore, in order to realize bright purely organic phosphors, efficiently promoting intersystem crossing from singlet to triplet and suppressing vibrational dissipation of triplets must be achieved. In this dissertation, I systematically investigated the two critical processes, i.e., singlet to triplet conversion through spin-orbit coupling and vibration suppression, and devised some strategies to achieve bright room temperature purely organic phosphorescence in amorphous films and optical ozone sensors based on phosphorescence phenomena.

Controlling the conjugation length of organic phosphors is a powerful tool to tune the emission color and establishing an understanding on the conjugation length effects on the spin-orbit coupling and consequential phosphorescent emission intensity is important. The effects of the conjugation length of the purely organic phosphors on the spin-orbit coupling efficiency for singlet to triplet conversion were systematically studied using a combined experimental and computational approach. The results showed that phosphorescence intensity decreased with red-shifted emission as the conjugation length increased, which has more correlation with intersystem crossing rate determined by spin-orbit coupling strength rather than singlet-to-triplet energy difference.

High quality doped crystals of purely organic phosphors have shown bright room temperature phosphorescence, however, they still have practical limitations such as required high quality crystal preparation and possible property alteration under operation conditions. Amorphous organic phosphorescence can be an attractive alternative to overcome those limitations. Embedding organic phosphors into amorphous glassy polymer was investigated as the first strategy to efficiently suppress the triplet vibration by restricting molecular motion of the

embedded organic phosphors. The vibration character of local segment of the matrix polymer represented by beta transition was identified as an important parameter largely affecting the emissive intensity of the embedded phosphors. Bright room temperature phosphorescence quantum yield of 7.5% was achieved by this strategy. This system showed temperature dependent phosphorescence attributed to changing vibrational characteristics of the matrix polymer. An optical temperature sensor integrated in a microfluidic device was devised and demonstrated. Incorporating strong hydrogen bonding between a newly devised purely organic phosphor and a hydrogen bonding capable matrix polymer, polyvinyl alcohol (PVA), was the second strategy, which suppresses vibration much more efficiently resulting in much brighter phosphorescence up to 24% quantum yield. Modulation of hydrogen bonding by water molecules showed unique reversible phosphorescence-to-fluorescence switching behavior, which was utilized to develop a ratiometric water sensor.

The knowledge and understanding established through fundamental studies have been utilized in applications. Based on the finding that the phosphorescence intensity of the purely organic phosphors is sensitive to environmental ozone concentration, I systematically investigated and revealed that the origin of the ozone sensitivity is due to oxidation of the aldehyde moiety of the organic phosphors and devised highly sensitive and convenient optical ozone sensors by utilizing the observed inverse linear correlation between the phosphorescence emission intensity and the ozone concentration. The obtained knowledge regarding the role of intermolecular interactions for vibration suppression was adapted to achieve high thermal conductivity in amorphous polymers by rationally designing hydrogen bonding donating and accepting polymer pairs, providing uniformly distributed strong interpolymer linkage so that thermal energy can find a continuous pathway to propagate. Thermal conductivity of $1.5 Wm^{-1}K^{-1}$ was achieved, which is one order of magnitude higher than that of conventional polymers.

CHAPTER 1

Introduction and Background

This chapter will describe the Organic Light Emitting Diodes (OLEDs) industry with a focus on OLED displays and solid-state lighting. The concepts of phosphorescence and fluorescence will be discussed through a Jablonski diagram. The two critical processes required to achieve phosphorescence, spin-orbit coupling and vibration suppression, will be reviewed. The most commonly used organometallic phosphors will be introduced in terms of the molecular design principle, technical limitations, and alternatives. Aromatic ketone compounds as purely organic phosphors will be discussed with a focus on intersystem crossing rate. A brief review on recent progress in purely organic, room-temperature phosphorescence in crystals and the Ph.D research objectives will be presented.

1.1. OLED Industry

1.1.1. OLED Displays

Organic Light Emitting Diodes (OLEDs) have attracted much attention due to their potential applications in flat panel displays and solid-state lighting.[1-4] Compared to LCD displays, OLEDs have many advantages such as high contrast and a large viewing angle. Moreover, they do not need a backlight, unlike other displays, which makes them the most energy efficient displays. Recently, OLED-based full-HD televisions and smartphones have been released in the market and have gained growing interest.[5, 6] OLEDs can be transparent[7] or flexible[8] if they are manufactured with transparent or flexible substrates, which provides a capability to realize smart windows[9] and paper displays[10].

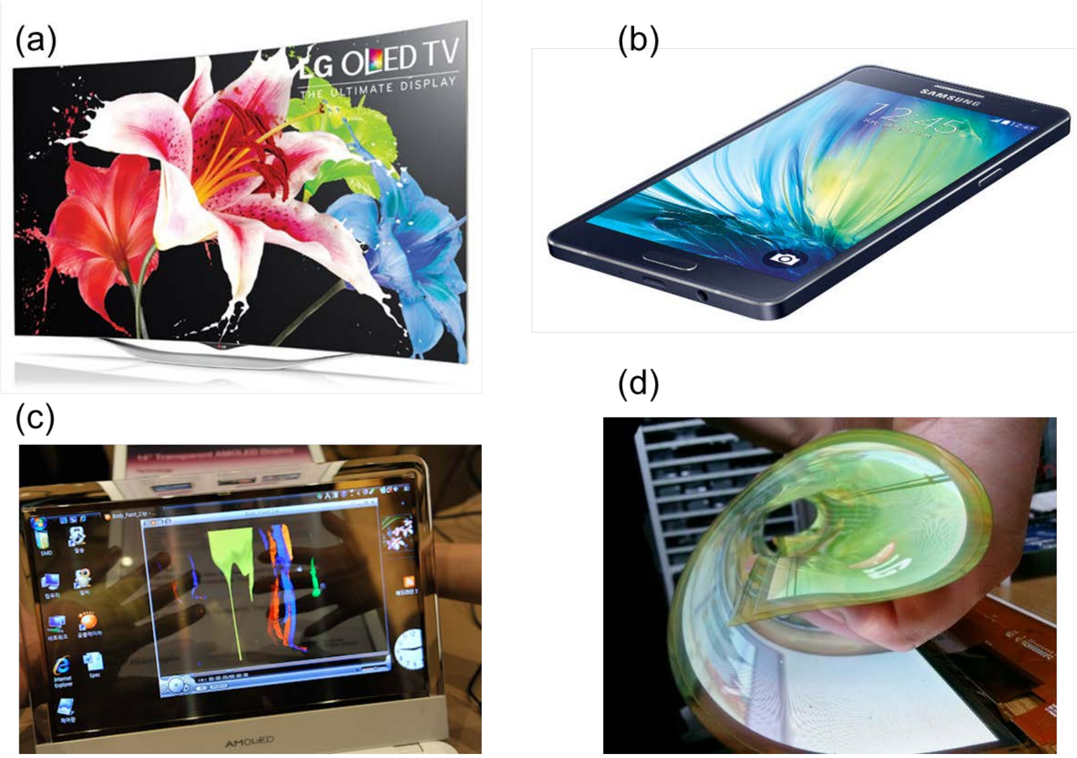

Figure 1.1. OLED-based television and smartphone. (a) LG's 55-inch Full-HD OLED TV[5], (b) Samsung's 5-inch 720p smartphone[6], (c) Samsung's 14-inch see-through display[7], and (d) LG's 18-inch flexible transparent display[8].

1.1.2. OLED Lighting

OLED lighting is another emerging industry because it is much more efficient and has a much smaller form factor than conventional incandescent or fluorescent lamps. An additional merit for OLED lighting is the flexibility because very thin flexible solid substrates can be used for construction. These characteristics, combined with the performance, make OLED lighting competitive with inorganic LED counterparts. Recently, German lighting expert Hella showed a new automobile rear light module which uses curved flexible OLEDs.[11] The module uses flexible OLED lighting panels (made by LG Chem) that were bent so each is shaped differently and so it creates a unique 3D structure. LG Chem has also developed the world's first OLED-based room light panel with a high luminous efficacy and long-lasting performance that can compete with inorganic LED lights.[12, 13]

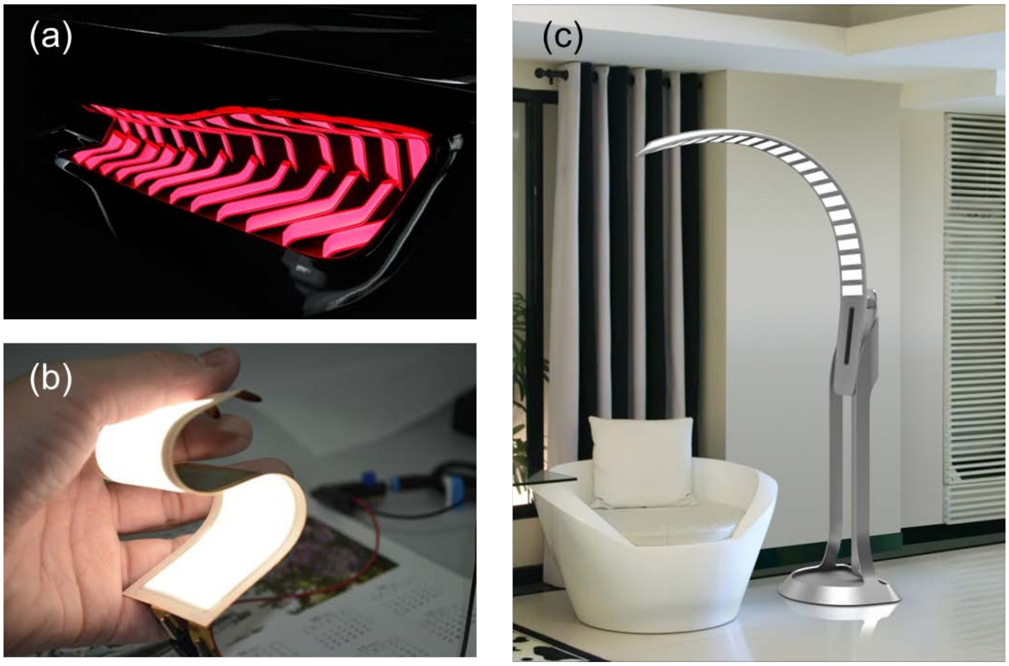

Figure 1.2. OLED-based lighting. (a) Hella's rear light module equipped in BMW[11], (b) LG Chem's flexible lighting prototype[12], and (c) Acuity brands flexible lighting using LG Chem's OLED panel[13].

1.2. Phosphorescence-based OLED

1.2.1. Phosphorescence vs. Fluorescence

Phosphorescent organic light-emitting diodes based on phosphors can, in theory, approach a 100% internal quantum efficiency by harvesting both singlet and triplet excitons simultaneously through intersystem crossing (ISC), which overcomes the limitation of 25% efficiency of conventional fluorescent OLEDs with the nature of emission from pure singlet excitons.[14-17] In order to produce phosphorescent light, unlike in fluorescence, excited photons undergo intersystem crossing from the singlet state to the triplet state, which causes long phosphorescence lifetimes (over hundreds of nanosecond). However, most organic materials only exhibit fluorescence because long-lived excited electrons are usually consumed as a form of heat by vibration in a shorter time regime (under tens of nanosecond) as shown in Figure 1.3. Therefore, in order to realize bright phosphorescence, efficiently promoting intersystem crossing from singlet to triplet and suppressing vibrational dissipation of triplets should be achieved.

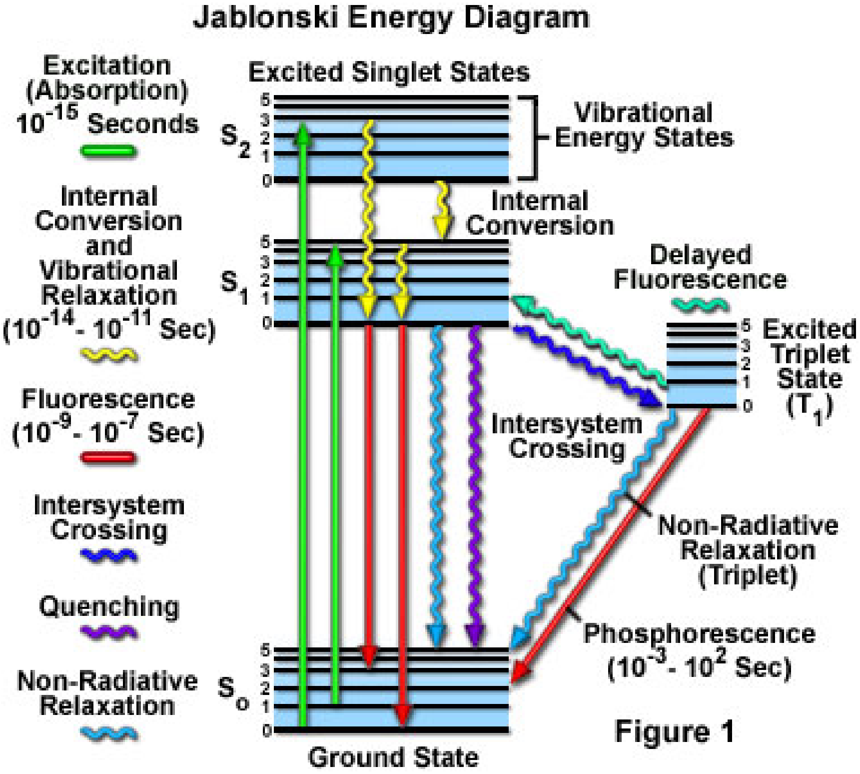

Figure 1.3. Jablonski diagram (from http://www.olympusmicro.com).

1.2.2. Intersystem Crossing

To be phosphorescent, first, the triplets must be efficiently generated by intersystem crossing from singlet to triplet. However, this is not a common case for organic materials because while singlet decay by fluorescence and internal conversion are fast, intersystem crossing is very slow due to the fact that conversion from a singlet excited electron to a triplet excited electron requires a change in spin angular momentum, which is forbidden. The intersystem crossing rate is proportional to the magnitude of spin-orbit coupling and inversely proportional to the energy gap between the lowest lying singlet and triplet as given by the following equation (1).

$$\text{intersystem crossing} \sim \frac{\mathrm{Eso}}{\Delta \mathrm{E_{ST}}} \qquad (1)$$

Also, spin-orbit coupling is determined by equation (2),

$$\mathrm{E_{SO}} = {}^{1}\Psi \left| H_{SO} \right| {}^{3}\Psi \qquad (2)$$

where ${}^{1}\Psi$ and ${}^{3}\Psi$ are the wavefunctions of singlet and triplet states, respectively, H_{SO} is the spin-orbit Hamiltonian. This equation indicates that a greater spin-orbit Hamiltonian provides a larger spin-orbit coupling and a larger intersystem crossing rate.

The spin-orbit Hamiltonian can be expressed as in equation (3).

$$H_{so} = -\frac{Z^4 e^2}{8\pi\varepsilon_0 m_e{}^2 c^2}\mathbf{l}\cdot\boldsymbol{s} \qquad (3)$$

Spin-orbit coupling occurs when the spin of an electron is influenced by the electron's motion around a nucleus. Based on equation (3), spin-orbit coupling is most prevalent in heavy atoms whose nuclei are large and as given by the Hamiltonian equation (3) is strongly proportional to the size of the atom.[18]

1.2.3. Vibration Suppression

In order for the triplet to survive long enough to phosphoresce, the phosphor must not suffer vibrational dissipation from triplet states. The simplest way to suppress vibration in organic phosphors is for triplet generating compounds to be cooled to 77K or lower. At these temperatures nuclear motion is highly restricted and many weakly or non-emissive room-temperature phosphors become very bright. However, this is not practically useful for any applications at ambient conditions. Alternative ways for room temperature phosphorescence of organic phosphors have been reported only if they are confined in inorganic crystals[19], micelles[20], or macromolecules[21], which provide a rigid environment to the embedded organic phosphors.

1.3. Phosphorescence in Organics

1.3.1. Organometallic Phosphor

Organometallic complexes are the most popular organic phosphors being used currently even though they are not purely organic. The heavy metal of organometallic complexes promotes spin-orbit coupling of electronic states, resulting in efficient intersystem crossing, short triplet lifetimes, and ensuing strong phosphorescent emission at room temperature. As illustrated in Figure 1.4, organometallic complexes of Pt, Ir, Ru, and Os have so far been heavily investigated as the emitting species in phosphorescent OLEDs.[22-24]

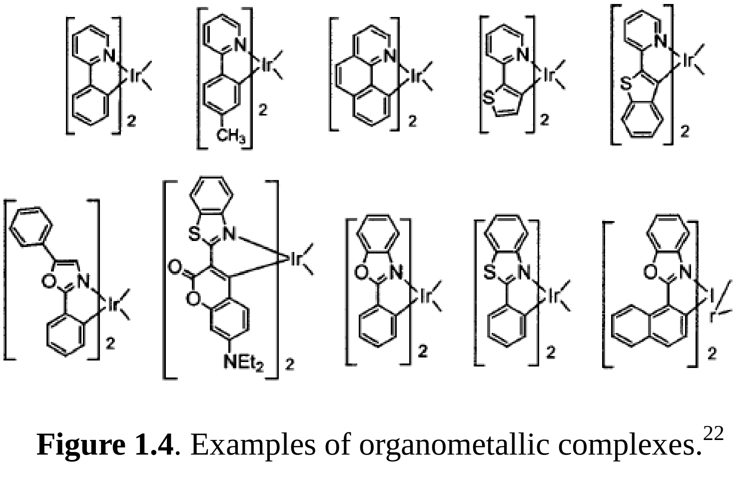

Figure 1.4. Examples of organometallic complexes.[22]

By designing ligands with specific excited state energies, the metal-ligand charge transfer is altered and the emission color can be tuned. Ligand structure can also be used to modulate the solid state properties of the chromophores, such as sublimation condition, charge transport properties, and surface morphology.[25, 26] Even though changing the ligands attached to the metal center can tune the emissive color, the required vacuum deposition process largely raise the manufacturing cost. In order to reduce the fabrication cost, small molecules have been doped into polymer matrices to be solution processed as shown in Figure 1.5.[27] These solution processable systems also have limitations such as aggregation-induced quenching[28] and inefficient energy transfer though.[29] To overcome these problems, phosphors are covalently bonded to a conjugated polymer backbone as shown in Figure 1.6.[30-32] In this system, researchers have focused on optimizing energy transfer by modulating excited energy states of phosphors. Schulz et al. firstly reported the effect of modifying the triplet energy of the polymer main chain to reduce triplet quenching of phosphorescent complexes.[33]

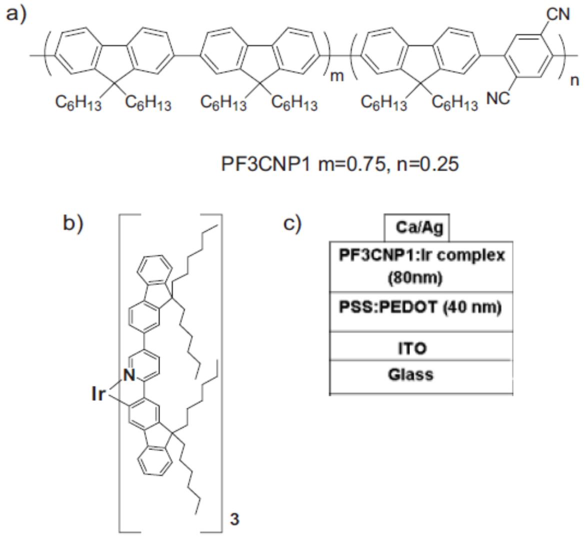

Figure 1.5. Example of solution processable phosphorescence. a) host polymer, b) Iridium complex, and c) device configuration.[27]

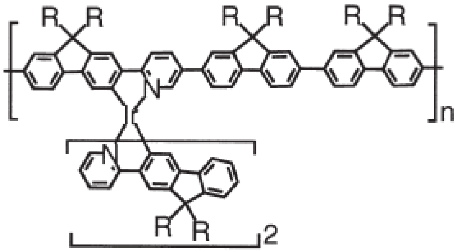

Figure 1.6. Example of covalently bonded polymer-iridium complex.[32]

Among the organometallic compounds, iridium complexes are most popular due to high quantum yield, desirable phosphorescent lifetimes, and relatively easy chemical synthesis. However, organometallic phosphors still have practical limitations such as limited metal choice and ligand design for color tuning. Also, higher energy emission at blue and near UV regions requires very high energy metal-ligand bonds, which have poor stability and short longevity[34], which is a critical issue all organometallic phosphors suffers from. Therefore, purely organic phosphors are very attractive as an alternative in terms of synthesis flexibility, good stability and easy color control by modulating the conjugation length.

1.3.2. Aromatic Ketones

Among purely organic phosphor, aromatic ketones have been well-known phosphorescent materials for several decades.[35] Excited spin of aromatic ketone is flipped from S_1 to T_2 at nearly one hundred percent efficiency because it has a triplet level (T_2) that is close in energy to S_1 and it satisfies the El-Sayed rule due to the orbital difference between S_1 (n-π*) and T_2 (π–π*).[36] Figure 1.7 illustrates this with the rates measured for benzophenone at 77 K.[37] The reason that these compounds are phosphorescent to some degree is the phenomenon of strong spin-orbit coupling at the carbonyl oxygen induced by small singlet-triplet energy difference.[38]

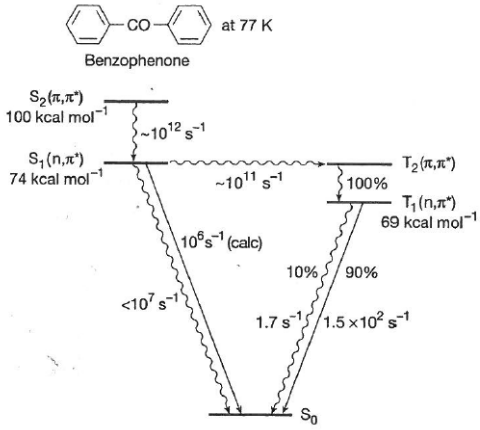

Figure 1.7. State diagram for benzophenone at 77 K.[37]

However, estimating ΔE_{ST} for intersystem crossing is complicated. El-Sayed's selection rule states that the rate of intersystem crossing is relatively large when molecule orbital type changes during the transition.[39] According to the rule, singlet (π,π^*) could transfer to triplet (n,π^*) but not to triplet (π,π^*) and vice versa. Figure 1.8 schematically shows that ΔE_{ST} in intersystem crossing is quite different based on the molecular structures. Therefore, aromatic carbonyl group is the important design factor to reduce ΔE_{ST}. However, it cannot guarantee efficient intersystem crossing. In Chapter 6, intersystem crossing rate will be further discussed through investigating a series of aromatic ketones with varying conjugation length.

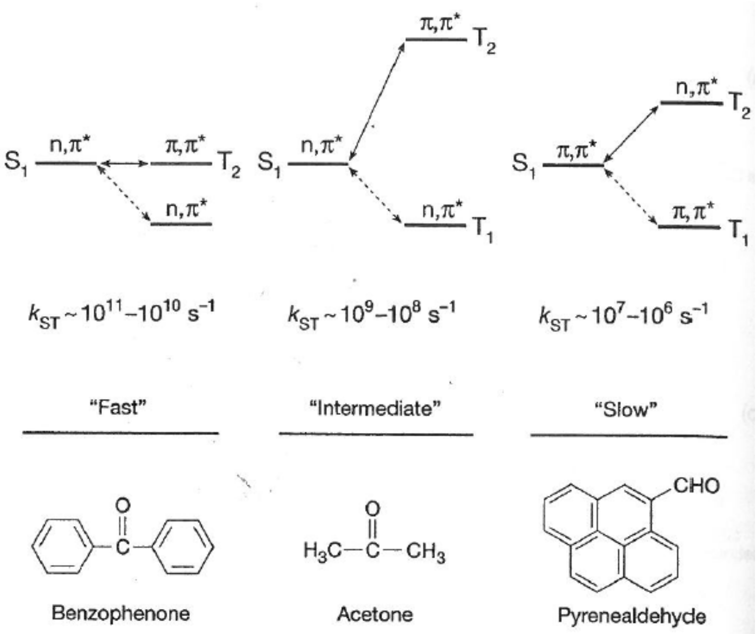

Figure 1.8. Examples of different rates of intersystem crossing for S_1(n,π*) → T(π,π*), S_1(n,π*) → T(n,π*), and S_1(π,π*) → T(π,π*) of carbonyl compounds.[37]

1.3.3. Phosphorescence in Crystals

Phosphorescence has rarely been observed in purely organic molecules at room temperature due to lack of heavy atom effect. Recently, metal-free organic phosphorescence at room temperature was reported by Yuan et al.[40] They observed crystallization induced phosphorescence from benzophenone and its halogenated derivatives whose chemical structures are shown in Figure 1.9. High quantum yield up to 40% was achieved by growing crystals in common solvents such as ethanol, DCM, and n-hexane. Figure 1.10 shows the color of crystals under ambient laboratory light and 365nm UV light at room temperature, respectively. This phenomenon was explained due to the restriction of vibrational motion by the rigid crystal structures. While their efforts can be a breakthrough in designing metal-free phosphors, it is still not practically useful because slow crystal growing process is inevitable and no color tuning strategy was devised.

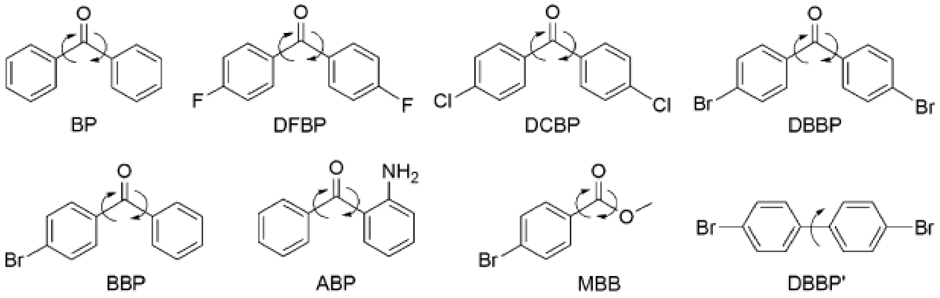

Figure 1.9. Phosphorescent chromophores grown to crystals.[40]

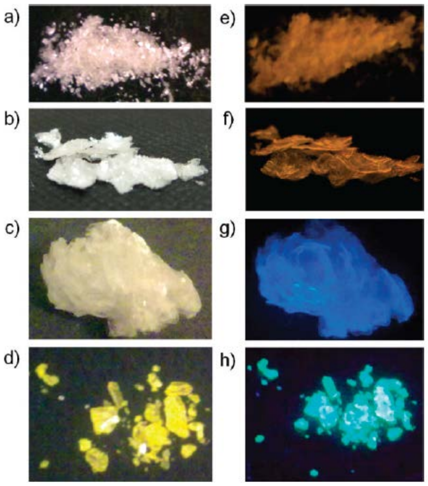

Figure 1.10. Crystals of DCBP, DBBP, BBP, and ABP taken (a-d) under laboratory lighting, and (e-h) under 365nm UV light at room temperature.[40]

More attractive room temperature phosphorescence was reported by Bolton et al.[41] They presented a directed heavy atom effect by halogen bonding between host matrix and phosphor. Aromatic aldehyde chromophores in solution (Figure 1.11a) are solely fluorescent without phosphorescent emission. Due to the weak spin-orbit coupling, triplet generation is not efficient and vibrational loss of the triplet is dominant. On the contrary, in a crystalline state (Figure 1.11b), phosphorescence is activated through enhanced spin-orbit coupling and reduced vibrational dissipation by intermolecular halogen bonding. Crystals of pure chromophore (Figure 1.11c) have a moderate emission quantum yield of 2.9% because of excimer-induced self-quenching. Mixed crystals with a proper host molecule providing strong halogen bonding show much brighter emission by preventing self-quenching (Figure 1.11d). Despite varying quantum yields depending on the crystal quality, mixed crystals have a considerably high value (~ 55%).

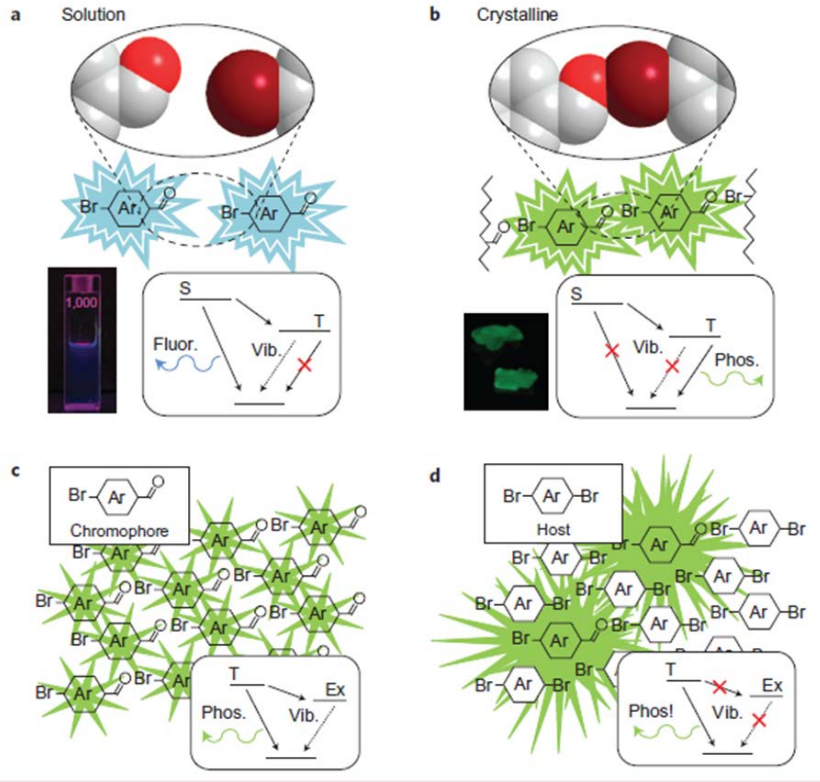

Figure 1.11. Directed heavy atom organic phosphorescence and its design principle.[41]

The color of the mixed crystal (Figure 1.12) can be easily tuned by modulating the conjugation length and/or electron density of chromophores and host compounds. However, the blue and red crystals are dimmer (1% of quantum yield) than the green one. The photophysical properties of these metal-free organic phosphors will be further investigated in Chapter 2 showing quantum yield optimization and fine color tuning via compositional variations in mixed crystals.

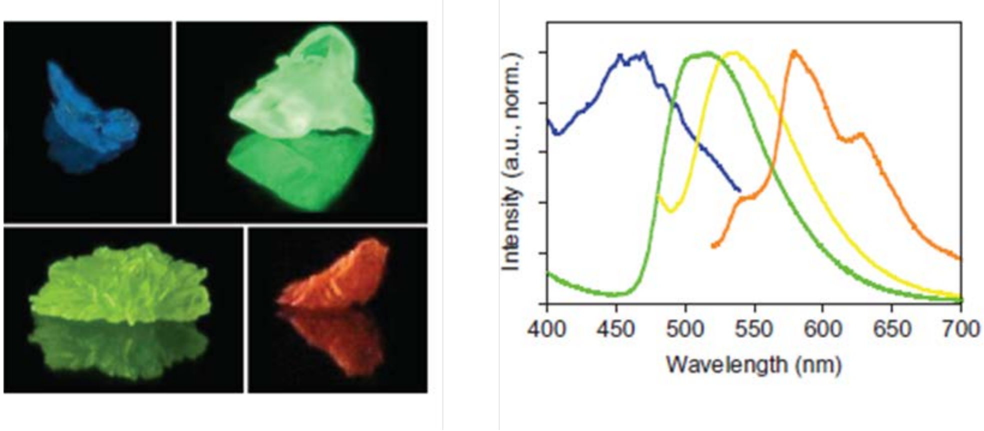

Figure 1.12. Photographs of crystals under 365nm UV light, and emission spectra of color-tuned aromatic aldehydes.[41]

1.4. Objectives

Though these approaches are very promising for developing metal-free organic phosphors, they still have limitations in practical applications because they stringently require crystalline materials. Film forming materials, such as polymers and amorphous solids, would be more attractive for device fabrication and processing; however, a means must be found in these systems to induce vibrational suppression that is on par with that generated by crystals. In Chapter 3, amorphous polymer matrix will be used in order to suppress triplet vibration of organic phosphors. Due to temperature-dependent rigidity of polymer, this system can be applied as a temperature sensor, and such an optical temperature sensor in microfluidic devices is demonstrated. In Chapter 4, more efficient vibration suppression will be discussed by introducing strong hydrogen bonding between polymer matrix and organic phosphors. By water or moisture absorption, phosphorescence turns to fluorescence in this system due to hydrogen bond cleavage, providing a potential of humidity sensor or optical recording media. In Chapter 5, unique optical ozone sensing property will be discussed compared to conventional conductance-based inorganic sensors. In Chapter 6, I will discuss conjugation length effect on phosphorescence at low temperature in terms of intersystem crossing rate and electron density calculation.

1.5. References

1. Yersin, H.; Rausch, A. F.; Czerwieniec, R.; Hofbeck, T.; Fischer, T. *Coord. Chem. Rev.* **2011**, *255*, 2622-2652.
2. Evans, R. C.; Douglas, P.; Winscom, C. J. *Coord. Chem. Rev.* **2006**, *250*, 2093-2126.
3. Xiao, L.; Chen ,L.; Qu, B.; Luo, J.; Kong, S.; Gong, Q.; Kido, J. *Adv. Mater.* **2011**, *23*, 926-952.
4. You, Y.; Han, Y.; Lee, Y.-M.; Park, S. Y.; Nam, W.; Lippard, S. J. *J. Am. Chem. Soc.* **2011**, *133*, 11488.
5. http://recombu.com/digital/news/lg-launches-new-55-inch-oled-tv.
6. http://www.oled-info.com/oled_devices/mobile_phones.
7. http://thetechjournal.com/electronics/laptop/samsung-developed-transparent-see-through-oled-screen.xhtml.
8. http://www.geeky-gadgets.com/lg-announced-flexible-transparent-oled-display-10-07-2014.
9. http://news.oled-display.net/samsung-display-flexible-transparent-and-stretchable-oled-concepts.
10. http://goodereader.com/blog/e-paper/lg-quietly-becoming-a-flexible-e-paper-juggernaut.
11. http://www.oled-info.com/hella-uses-lg-chems-flexible-oleds-develop-automobile-rear-light-module-prototype.
12. http://www.oled-info.com/lg-chem-plastic-based-truly-flexible-oled-prototype-photo.

13. http://www.koreaherald.com/view.php?ud=20140911000901.
14. Tang, C. W.; VanSlyke, S. A. *Appl. Phys. Lett*. **1987**, *51*, 913-915.
15. Baldo, M. A.; O'Brien, D. F.; You, Y.; Shoustikov, A.; Sibley, S.; Thompson, M. E.; Forrest, S. R. *Nature* **1998**, *395*, 151-154.
16. Adachi, C.; Baldo, M. A.; Forrest, S. R.; Thompson, M. E. *Appl. Phys. Lett*. **2000**, *77*, 904-906.
17. Reineke, S.; Lindner, F.; Schwartz, G.; Seidler, N.; Walzer, K.; Lussem, B.; Leo, K. *Nature* **2009**, *459*, 234-238.
18. Atkins, P. W.; Friedman, R. S. *Molecular Quantum Mechanics* (Oxford University Press, New York, NY, **1997**).
19. Kahr, B.; Gurney, R. W. *Chem. Rev*. **2001**, *101*, 893-951.
20. Love, L. J. C.; Skrillec, M.; Habarta, J. G. *Anal. Chem*. **1980**, *52*, 754-759.
21. Turro, N. J.; Obuko, T.; Chung, C. *J. Am. Chem. Soc*. **1982**, *104*, 1789-1794.
22. Lamansky, S.; Djurovich, P.; Murphy, D.; Abdel-Razzaq, F.; Lee, H.; Adachi, C.; Burrows, P. E.; Forrest, S. R.; Thompson, M. E. *J. Am. Chem. Soc*. **2001**, *123*, 4304-4312.
23. Niu, Y.; Tung, Y.; Chi, Y.; Shu, C.; Kim, J. H.; Chen, B.; Luo, J.; Carty, A. J.; Jen, A. K. *Chem. Mater*. **2005**, *17*, 3532-3536.
24. Yang, J.; Gordon, K. C. *Synth. Met*. **2005**, *152*, 213-216.
25. Burn, P. L.; Lo, S. C.; Samuel, I. D. W. *Adv. Mater*. **2007**, *19*, 1675-1688.
26. Ding, J.; Gao, J.; Cheng, Y.; Xie, Z.; Wang, L.; Ma, D.; Jing, X.; Wang, F. *Adv. Funct. Mater*. **2006**, *16*, 575-581.

27. Gong, X.; Ostrowski, J. C.; Bazan, G. C.; Moses, D.; Heeger, A. J.; Liu, M. S.; Jen, A. K. *Adv. Mater*. **2003**, *15*, 45-49.
28. Sandee, A. J.; Williams, C. K.; Evans, N. R.; Davies, J. E.; Boothby, C. E.; Kohler, A.; Friend, R. H.; Holmes, A. B. *J. Am. Chem. Soc*. **2004**, *126*, 7041-7048.
29. Zhen, H.; Jiang, C.; Yang, W.; Jiang, J.; Huang, F.; Cao, Y. *Chem. Eur. J*. **2005**, *11*, 5007-5016.
30. Chen, X.; Liao, J. L.; Liang, Y.; Ahmed, M. O.; Tseng, H. E.; Chen, S. A. *J. Am. Chem. Soc*. **2003**, *125*, 636-637.
31. Jiang, J.; Jiang, C.; Yang, W.; Zhen, H.; Huang, F.; Cao, Y. *Macromolecules* **2005**, *38*, 4072-4080.
32. Ito, T.; Suzuki, S.; Kido, J. *Polym. Adv. Technol.* **2005**, *16*, 480-483.
33. Schulz, G. L.; Chen, X.; Chen, S. A.; Holdcroft, S. *Macromolecules* **2006**, *39*, 9157-9165.
34. Kawamura, Y.; Yanagida, S.; Forrest, S. R. *J. Appl. Phys*. **2002**, *92*, 87-93.
35. Kearns, D. R.; Case, W. A. *J. Am. Chem. Soc*. **1966**, *88*, 5087-5097.
36. Kiritani, M.; Yoshii, T.; Hirota, N.; Baba, M. *J. Chem. Phys*. **1994**, *98*, 11265-11268.
37. Turro, N.J. *Modern Molecular Photochemistry* (University Science Books, Sausalito CA, **1991**).
38. M. Klessinger, J. Michl, *Excited States and Photochemistry of Organic Molecules* (VCH Publishers, **1995**)
39. El-Sayed, M. A. *Acc. Chem. Res*. **1968**, *1*, 8-16.

40. Yuan, W. Z.; Shen, X. Y.; Zhao, H.; Lam, J. W. Y.; Tang, L.; Lu, P.; Wang, C.; Liu, Y.; Wang, Z.; Zheng, Q.; Sun, J. Z.; Ma, Y.; Tang, B. Z. *J. Phys. Chem. C* **2010**, *114*, 6090−6099.

41. Bolton, O.; Lee, K.; Kim, H.-J.; Lin, K. Y.; Kim, J. *Nat. Chem*. **2011**, *3*, 205−210.

CHAPTER 2

Tuning the Photophysical Properties of Metal-Free Room Temperature Organic Phosphors via Compositional Variations in Bromobenzaldehyde/Dibromobenzene Mixed Crystals

This chapter describes photophysical properties of phosphorescent mixed crystals in detail in terms of quantum yield optimization and fine color tuning via compositional variations of dibromo host material and bromobenzaldehyde emitter. Quantum yield is maximized when emitter and host are identically sized and emitter concentration is present at 1-10 wt %. XRD data reveals the crystal structure of host material is not ruined much to be responsible for quantum yield drop by inclusion of mismatched emitter. In order to fine-tune emission color, altering halogen substitution of the emitter provides sequential 5-30 nm changes to emission maxima in the green region. These findings elucidate the complex optical and solid state behavior these materials exhibit and illustrate the influence that material preparation has on their performance.

Parts of this chapter appear in: Bolton*, O.; Lee*, D.; Jung, J.; Kim, J. *Chem. Mater*. **2014**, *26*, 6644-6649.

2.1. Introduction

Until recently phosphorescence from metal-free purely organic materials was regarded as an intractably inefficient phenomenon, leading these compounds to receive little attention from relevant applications,[1] such as phosphorescent organic light emitting diode (PhOLED)[2-6] and photovoltaic fields.[7-9] More recently, however, reports have begun to awaken interest in purely organic phosphorescence for applications in sensing[10-13] and potential uses in optoelectronic devices.[14-19] Several families of purely organic phosphors including fluoroborons,[20-22] acenes,[23-25] thiones,[26-27] and classic aromatic ketones[28-29] are emerging or re-emerging with promise for use in optical applications. One such family of purely organic phosphors that has emerged from the growing field of crystal engineering[30-36] and has received recent attention is that of bromobenzaldehyde / dibromobenzene-style crystal phosphors reported recently by our group.[14] These materials feature robust high room temperature quantum efficiency and tunable emission color from simple small molecules. Realizing the attractive functional qualities of these materials, however, depends greatly on optimizing crystal and chemical structures, a combination that is non-trivial. Here we report phosphorescent quantum efficiency and fine color tuning of the first members of this family of organic phosphor by varying compositions and chemical structures. These organic materials consist primarily of an emitter compound that features an aromatic aldehyde with bromine substitution. These emitters are non-phosphorescent when in solution or liquid states, but they produce photoluminescent phosphorescence when crystallized. This, we have hypothesized, is because the bromine atoms in their structures both promote intersystem crossing via the heavy atom effect and prevent carbonyl vibration via a halogen bond.[37-39] This hypothesis is built upon the existing understanding of the heavy atom effect,[40] the spin-orbit coupling activity of aromatic carbonyls,[41] and the fact that all phosphorescent crystal structures in this family feature such halogen-carbonyl oxygen contact. Also, the phosphorescent efficiency of these materials has been observed to correlate with crystal quality, suggesting that the emission mechanism is influenced by the solid state condition of this compound.[14]

When these aldehyde emitters are condensed into their pure crystals, they suffer greatly from self-quenching and produce suboptimal phosphorescence. It is to avoid this consequence that a mixing approach is taken: a non-carbonyl, dibromo host crystal provides the desired crystal lattice and halogen contact while allowing the emitter to emit in functional isolation. Compounds 2,5-dihexyloxy-4-bromobenzaldehyde (Br6A) and 2,5-dihexyloxy-1,4-dibromobenzene (Br6) are such a combination of emitter and host, respectively. These compounds (Figure 2.1a) represent one of the simplest and brightest emitter/host combinations in this young family of phosphors. Pure Br6A crystals are only weakly emissive but when Br6A is doped into crystals of Br6, which are otherwise completely non-emissive, phosphorescent emission from Br6A becomes very bright (Figure 2.1b).

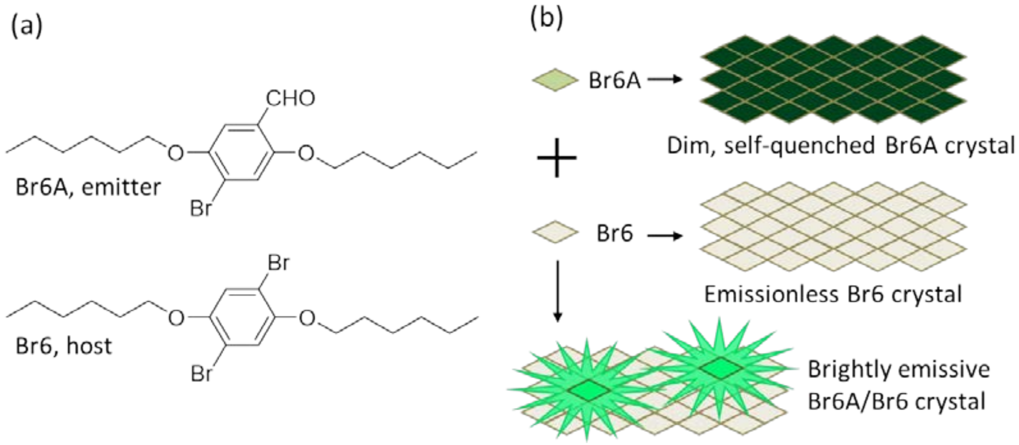

Figure 2.1. Bromobenzaldehyde purely organic phosphorescent crystals. (a) Benchmark aldehyde emitter and host, Br6A and Br6, respectively. (b) Schematic illustration of dim Br6A (emitter) crystals, non-emissive Br6 (host) crystals, and bright phosphorescent Br6A/Br6 (mixed crystals).

Our hypothesis that Br6A becomes included into the Br6 crystal lattice by substitution, and thus experiences the same order and halogen contact, is supported by the fact that phosphorescent emission from Br6A/Br6 mixed crystals is polarized, indicating that Br6A is ordered in the Br6 crystal (Figure 2.2).

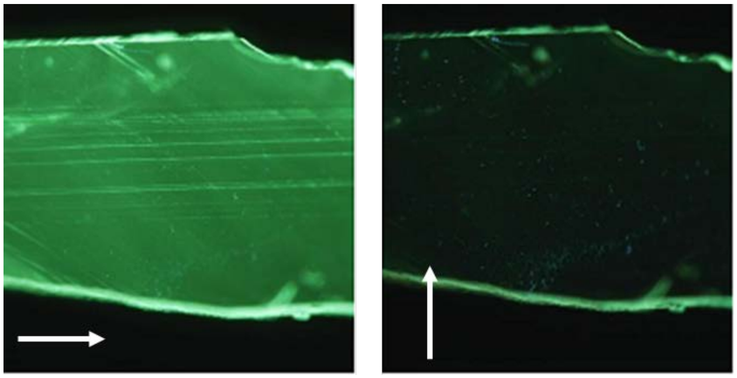

Figure 2.2. Microscope images of polarized phosphorescent emission from a thin Br6A/Br6 crystal. Arrows indicate relative polarizer direction.

Unfortunately, the emitter/host relationship that gives these materials their high quantum efficiency also complicates optimization. An ideal system features emitter substituted perfectly into a high quality host crystal and, unfortunately, though the emitter is very similar to the host, it is not identical. It is an impurity in the host crystal and, thus, not thermodynamically favored in the host crystal. This renders these mixed crystal phosphors susceptible to a number of emission-reducing conditions (Figure 2.3). Optimizing quantum efficiency thus requires optimizing mixing so that the maximum population of emitters present are isolated and ordered within the host crystal.

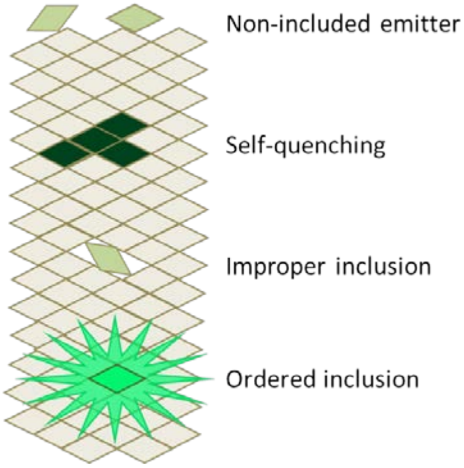

Figure 2.3. Sources of reduced quantum efficiency in mixed crystal pure organic phosphors (upper three) and the emissive outcome of a perfectly included and isolated emitter (bottom).

2.2. Experimental Section

2.2.1. Materials

Synthesis of 2,5-dihexyloxybenzaldehyde (H6A). 2-Bromo-1,4-dihexyloxybenzene (1 equiv.) was loaded into a two-neck round bottomed flask and vacuum purged with argon three times. Anhydrous tetrahydrofuran was added by syringe (ca. 25 mL solvent / g reagent) and the vessel was placed into a bath of dry ice and 2-propanol at -78 °C. A solution of *n*-Butyllithium in hexanes (2.5 M, 1 equiv.) was added dropwise via syringe and the reaction was then stirred at -78 °C for 1 hour. Anhydrous DMF (4 equiv.) was then added and the reaction was allowed to warm to 23 °C for three hours. The reaction was quenched carefully with water and extracted with diethyl ether. The organic layer was collected and dried over $MgSO_4$ before being filtered and the solvent removed by rotary evaporation. Products were purified by column chromatography with ethyl acetate/hexane (1:30) eluent. Viscous oil eventually crystallizing into a white solid was collected at a yield of 79%. ^{1}H NMR (500 MHz, $CDCl_3$): δ 10.47 (s, 1H, C*H*O), 7.31 (d, $^4J_{(H-H)} = 3.0$ Hz, 1H, Ar-*H*), 7.11 (q, $^4J_{(H-H)} = 3.0$ Hz, $^3J_{(H-H)} = 4.0$ Hz, 1H, Ar-*H*), 6.92 (d, $^3J_{(H\text{-}H)}$ = 4.0 Hz, 1H, Ar-*H*), 4.03 (t, $^3J_{(H\text{-}H)}$ = 6.5 Hz, 2H, OC*H*$_2$), 3.94 (t, $^3J_{(H\text{-}H)}$ = 6.5 Hz, 2H, OC*H*$_2$), 1.81 (m, 2H, C*H*$_2$), 1.55 (m, 2H, C*H*$_2$), 1.42 (m, 4H, C*H*$_2$), 1.32 (m, 8H, C*H*$_2$), 0.91 (t, $^3J_{(H\text{-}H)}$ = 6.0 Hz, 6H, C*H*$_3$). ^{13}C NMR (100 MHz, CDCl$_3$): δ 14.0, 22.5, 25.6, 29.2, 31.5, 68.7, 69.2, 110.8, 114.4, 124.1, 125.1, 153.0, 156.3, 189.8. HRMS (ESI)$^+$ *m/z* 307.2273 ($C_{19}H_{31}O_3$ [M+H]$^+$ requires 307.2268).

Synthesis of 4-chloro-2,5-dihexyloxybenzaldehyde (Cl6A). Cl6A was made by formylation of 4-chloro-2,5-dihexyloxy-1-iodobenzene in a method similar to that used to produce H6A. White crystals were collected at a yield of 59%. ^{1}H NMR (400 MHz, CDCl$_3$): δ 10.41 (s, 1H, C*H*O), 7.36 (s, 1H, Ar-*H*), 7.04 (s, 1H, Ar-*H*), 4.02 (t, $^3J_{(H\text{-}H)}$ = 6.4 Hz, 2H, OC*H*$_2$), 4.01 (t, $^3J_{(H\text{-}H)}$ = 6.4 Hz, 2H, OC*H*$_2$), 1.82 (m, 4H, C*H*$_2$), 1.48 (m, 4H, C*H*$_2$), 1.34 (m, 8H, C*H*$_2$), 0.91 (t, $^3J_{(H\text{-}H)}$ = 6.0 Hz, 6H, C*H*$_3$). ^{13}C NMR (100 MHz, CDCl$_3$): δ 14.0, 22.5, 25.6, 29.0, 31.4, 69.4, 69.7, 111.1, 115.4, 123.6, 131.0, 148.9, 155.8, 188.8. HRMS (ESI)$^+$ *m/z* 341.1884 ($C_{19}H_{30}ClO_3$ [M+H]$^+$ requires 341.1878).

Synthesis of 2,5-dihexyloxy-4-iodobenzaldehyde (I6A). I6A was made by lithiation of 1,4-diiodo-2,5-dihexyloxybenzene in a method similar to that used to produce H6A and Cl6A. White crystals were collected at a yield of 31%. ^{1}H NMR (400 MHz, CDCl$_3$): δ 10.42 (s, 1H, C*H*O), 7.46 (s, 1H, Ar-*H*), 7.19 (s, 1H, Ar-*H*), 4.02 (t, $^3J_{(H\text{-}H)}$ = 6.0 Hz, 2H, OC*H*$_2$), 4.00 (t, $^3J_{(H\text{-}H)}$ = 6.0 Hz, 2H, OC*H*$_2$), 1.82 (m, 4H, C*H*$_2$), 1.49 (m, 4H, C*H*$_2$), 1.35 (m, 8H, C*H*$_2$), 0.91 (t, $^3J_{(H\text{-}H)}$ = 6.8 Hz, 6H, C*H*$_3$). ^{13}C NMR (100 MHz, CDCl$_3$): δ 14.0, 16.2, 22.5, 22.6, 25.6, 25.7, 29.0, 31.4, 69.5, 69.9, 108.8, 124.5, 125.1, 152.1, 155.8, 189.3. HRMS (ESI)$^+$ *m/z* 433.1232 ($C_{19}H_{30}IO_3$ [M+H]$^+$ requires 433.1234).

2.2.2. Measurement and Characterization

Proton NMR was conducted on a Varian Inova 500 equipped with a Varian indirect detection probe using $CDCl_3$ solvent with chemical shifts identified relative to 0.05 v/v% tetramethylsilane standard (0.00 ppm). ^{13}C NMR was conducted on a Varian MR400 equipped with a Varian 5 mm PFG AutoX Dual Broadband probe using $CDCl_3$ for which the solvent peak was used to calibrate. Anhydrous tetrahydrofuran was generated by distilling over sodium metal and benzophenone, collected only from deep purple solution.

UV-Vis electronic absorption measurements were collected using a Varian Cary 50 Bio spectrometer with solution samples held in a quartz cuvette. Photoluminescent (PL) emission, excitation, and quantum yield data were collected using a Photon Technologies International (PTI) Quantamaster system equipped with an integrating sphere. Gated photoluminescence was collected with a delay time of 150 μs after 365 nm excitation of each sample at room temperature. X-ray diffraction for dropcast mixed crystals was carried by a Rigaku Rotating Anode X-ray Diffractometer (X-ray wavelength: 1.54 Å). Microscope images were collected on an Olympus BX51 W/DP71 fluorescent microscope equipped with cross-polarizers.

Quantum yield (QY) was measured using an integrated sphere whose accuracy was verified using a 10 mM Rhodamine 6G/ethanol solution.[42] Samples for quantum yield measurement were prepared by dropping 0.1 g/mL chloroform solutions of the desired compounds, mixed in the weight ratios reported, onto an unmodified glass substrate. Crystal "film"' would form as the solvent evaporated. Each sample had a total mass of 2 mg. Absorption and emission inside the sphere was determined by comparison to a blank sample (glass only). A neutral density filter was used to allow for maximization of the emission signal without saturating the photomultiplier tube detector with excitation light. Each sample type was run in quadruplicate (or more) with each quantum yield measurement coming from a freshly dropcast sample. Measurements proved highly repeatable, and errors are given as ± 1 standard deviation.

2.3. Results and Discussion

The limits of inclusion efficiency were probed via a size exclusion experiment. In order to perturb mixing, a series of analogous aldehydes and hosts were synthesized with alkoxy chain lengths variable from five to eight carbon atoms (Figure 2.4a). These were intermixed in crystals grown by dropcasting chloroform solutions containing 1 wt % aldehyde, and their photoluminescence quantum efficiencies were measured using an integrating sphere. As expected, emission was brightest when aldehyde and host were the same size. Mismatched emitter and host combinations were seen to mix surprisingly well, though distinctly worse than ideally matched pairs, with quantum efficiency dropping as the size difference grows. This was true for both undersized and oversized emitters, though when the emitter was larger than the host the quantum efficiency was markedly lower than in the opposite case. This can be seen in Figure 2.4b, where the lower left corner of the image is qualitatively darker and quantitatively weaker than the upper right.

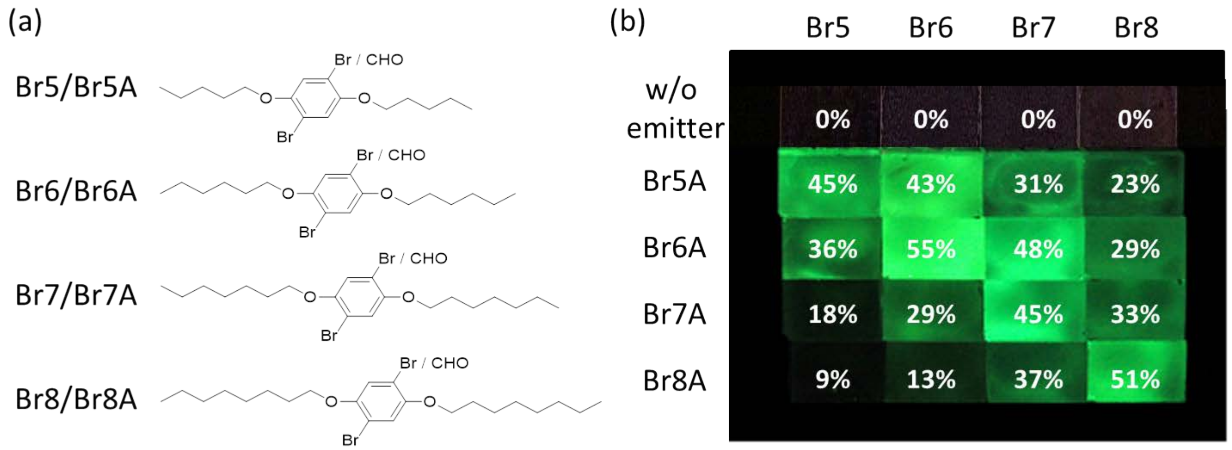

Figure 2.4. Emitter inclusion perturbed by size exclusion. (a) Chemical structures of emitters Br(5-8)A and hosts Br(5-8). (b) Photograph of dropcast crystals made of mixed aldehyde and host compounds illuminated by 365 nm light. Quantum efficiencies measured from samples of the same compositions and growth conditions.

The fact that phosphorescence is generated from mismatched emitter-host pairs, some dramatically mismatched, indicates that inclusion is kinetically quite favorable, even if not thermodynamically so. This is made especially clear when oversized emitters, in some cases six methylene carbons and 7.5 Å longer than their hosts, produce appreciable emission even when mixed with undersized hosts. This experiment also suggests, for these compounds and this growth method, a possible optimum empirical quantum efficiency of ca. 45-55%, as each ideally-matched combination is in near agreement. XRD was performed for mixed crystals grown from each emitter Br(5-8)A as a guest in Br6 host in order to examine how the size mismatch affects the crystal packing of host Br6. XRD data were analyzed based on the XRD pattern of Br6 single crystal. As shown in Figure 2.5, they show three characteristic peaks appearing at 10.15, 20.5, and 23.7^{o} corresponding to (001) plane from Br-Br contact, (110) plane from H-Br contact, and (020) plane from H-Br contact, respectively, which indicates that by the inclusion of 1 wt % mismatched guest emitter the crystal structure of Br6 is not significantly altered to be responsible for the reduced quantum efficiency. The emission lifetime of bromobenzaldehyde guests also remains in a similar range regardless of the size mismatch as shown in Table 2.1.

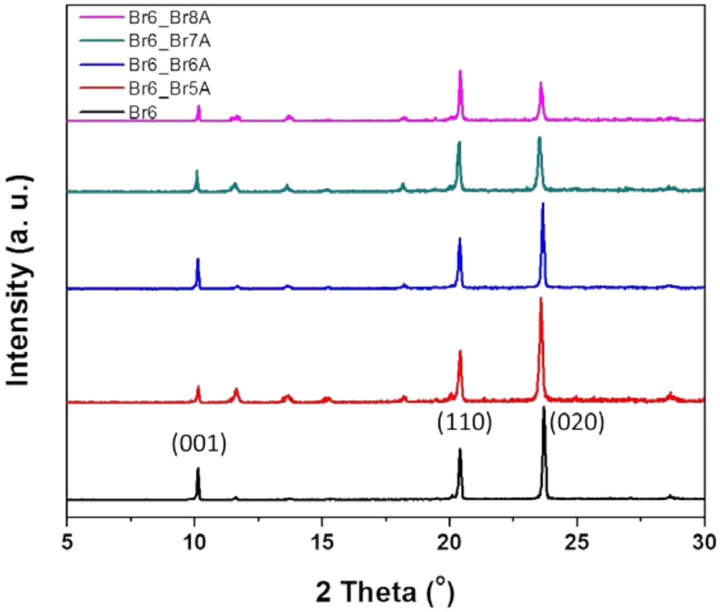

Figure 2.5. XRD pattern of mixed crystal with different emitters in Br6 prepared by dropcast on a glass substrate. Data were analyzed based on the XRD pattern of Br6 single crystal. Doping concentration was 1 wt % for all experiments.

Table 2.1. Photophysical properties of mixed crystals. Phosphorescence lifetime was collected from time-resolved measurement of 515 nm emission with single decay curve fitting

	τ_T (ms)	Φ_p (%)	k_p (s^{-1})
Br5_Br7A	4.45	17.53	3.94×10^3
Br6_Br7A	7.41	28.65	3.87×10^3
Br7_Br7A	8.96	44.70	4.99×10^3
Br8_Br7A	6.82	32.60	4.78×10^3

In order to determine an optimal mixing ratio of emitter and host, several samples were made with varying concentrations of Br6A in Br6. Both compounds were mixed in a chloroform solution to the desired amounts before being dropcast onto unmodified glass slides. Br6A content was varied from 0.0001 wt % to 100 wt %, as total solids. No fewer than four samples were made from each combination and these were measured for quantum efficiency in an integrating sphere. Efficiencies were charted showing a mixing ratio of 1 wt % Br6A to produce the brightest samples, though samples of 10 wt % Br6A were in close agreement (Figure 2.6a). A rapid reduction in quantum efficiency was observed as Br6A concentration was either increased or decreased. Quantum efficiency tapered from a maximum of 55% at 1 wt % Br6A to 0.1% at 100 wt % Br6A and 0.4% at 0.0001 wt % Br6A. Gated phosphorescence spectra (Figure 2.6b) of the samples used for this mixing ratio study confirm that the green emission is phosphorescence emission from the embedded Br6A.

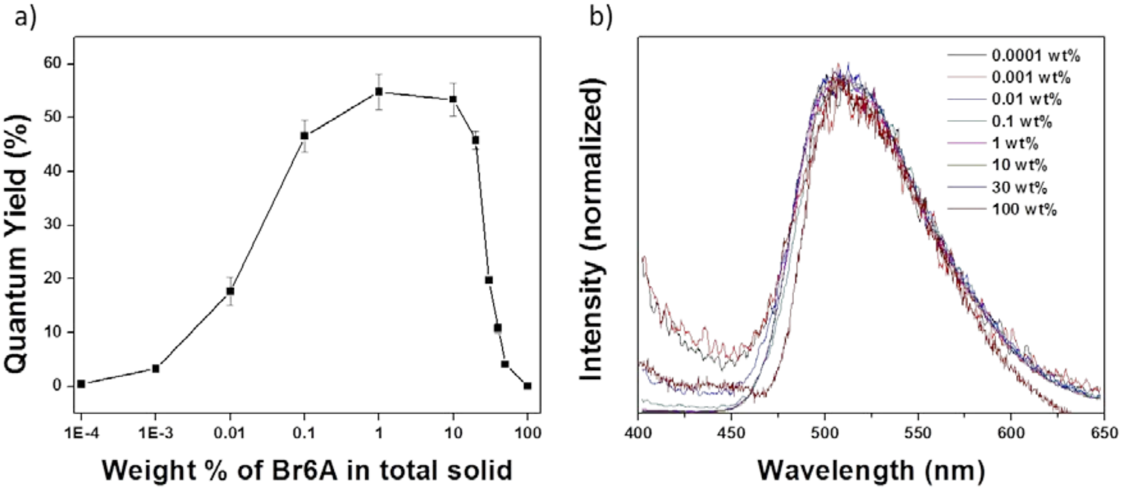

Figure 2.6. a) Phosphorescent quantum efficiency versus weight percentage of Br6A in Br6A/Br6 mixed crystal sampled from dropcast. Error bars represent ± one standard deviation. b) Normalized gated PL emission was collected with a delay time of 150 μs after 365 nm excitation of each sample at room temperature.

Regardless of the side chain length the same trend was observed in all cases where emitter from Br5A to Br8A was intermixed at varying concentration from 0.01 wt % to 30 wt % with its matching host from Br5 to Br8 (Figure 2.7). Substituting different solvents for drop casting and dropcast solution concentration, and changing substrate temperature and hydrophobicity did not make any meaningful change in the maximum phosphorescence quantum yield of 55% (Figure 2.8).

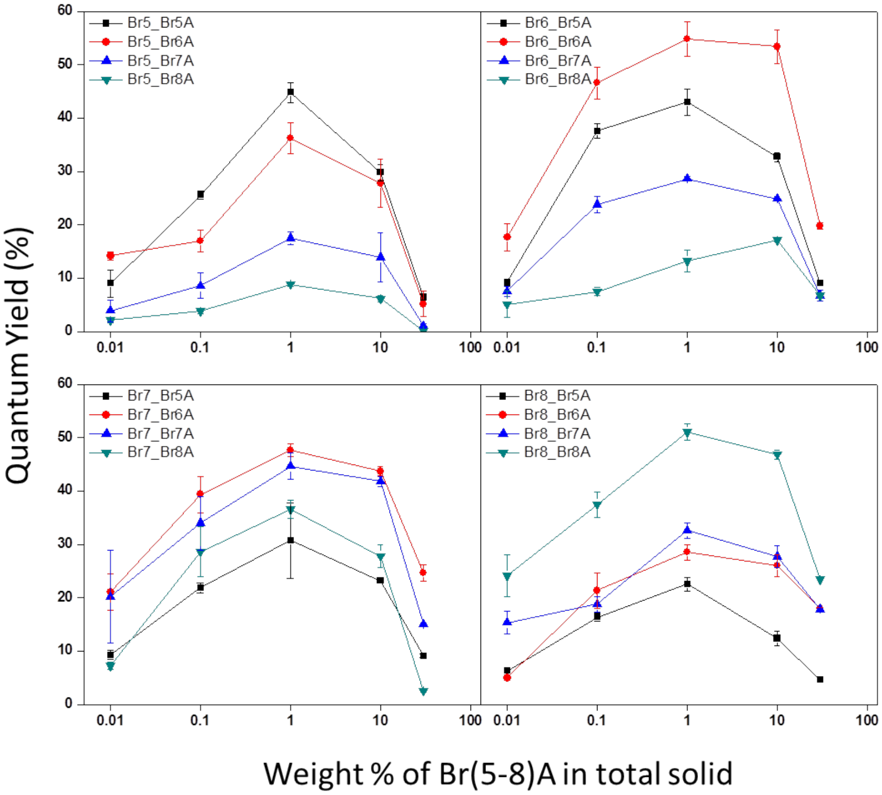

Figure 2.7. Phosphorescence quantum yield as a function of weight percentage of emitters Br(5-8)A in mixed crystal with hosts Br(5-8). Error bars represent ± one standard deviation.

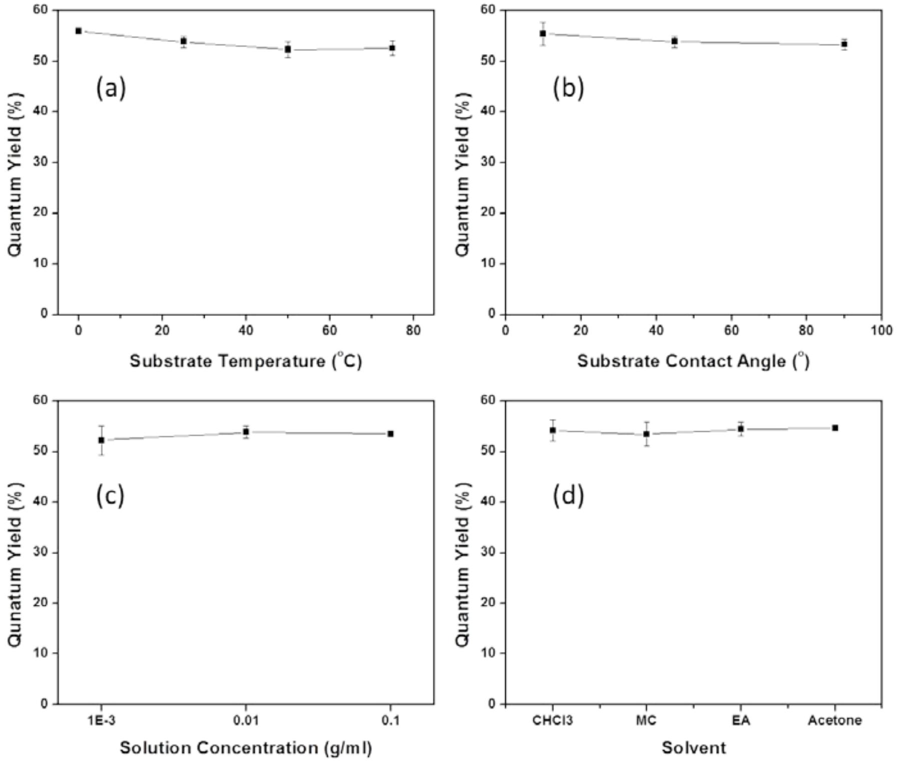

Figure 2.8. Phosphorescence quantum yield of Br6A/Br6 mixed crystal dropcast on a glass substrate under different conditions. (a) Temperature effect, (b) the glass substrates were treated with sulfuric acid and Hexamethyldisilazane (HMDS) to make hydrophilic (contact angle 10^o) or hydrophobic (contact angle 90^o) surface, respectively. (c) Solution concentration was changed based on total solids per solvent amount, and (d) different solvent was used. Doping concentration was 1 wt % for all experiments.

While it is not unexpected that quantum efficiency would drop as Br6A content increases, a drop as Br6A content decreases is surprising. At high concentrations of Br6A self-quenching is anticipated as Br6A-Br6A contact becomes more likely and the sample trends toward pure Br6A. The same is not true at low concentrations of Br6A where emitter isolation becomes extremely likely. Simple statistical analysis eliminates the possibility that this trend is evidence that a dimer or multi-aldehyde interaction is facilitating phosphorescence because, for example, at concentrations of 1 wt % Br6A the likelihood of Br6A-Br6A contact in the crystal is far below

55%, the quantum efficiency measured at that loading of Br6A. We hypothesize that quantum efficiency loss at low Br6A concentration is due to poor inclusion of the increasingly sparse Br6A into the increasingly pure Br6 crystals. Phosphorescence microscopy reveals that Br6A/Br6 crystals are brightest near nucleation sites (Figure 2.9) and often feature sharp drop-offs in emission brightness. This indicates that the inclusion rate is not constant throughout the growth of the host crystals. If Br6A molecules are not leaving solution soon enough to catch Br6 crystals in early growth in the dropcast films, as would likely be the case when Br6A concentrations are low, inclusion will suffer. So, just as recrystallization is done in the wet lab successively to purify crystalline materials, at these low levels of Br6A the emitter is less likely to become included into the relatively pure Br6 crystal formed from dropcast.

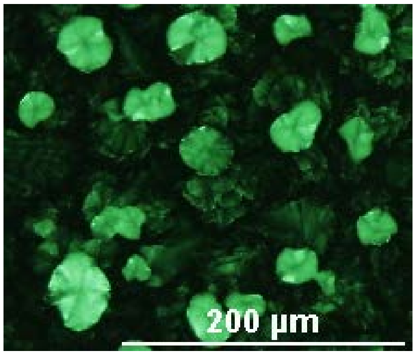

Figure 2.9. Markedly brighter regions surrounding apparent nucleation sites in Br6A/Br6 mixed crystals.

Note that because these samples were made by dropcast, crystal quality is worse than that of crystals grown slowly from supersaturated solution. This is why pure Br6A here (dropcast) measured a quantum efficiency of 0.1% while Br6A reported in our earlier work, there measured as high quality single crystals, exhibited a quantum efficiency of 2.9%. While that trend is true for pure crystals, dropcasting is preferable to solution growth for mixed crystals because the likelihood of kinetically entrapped inclusion of the emitter into the host is much better in the faster process, dropcasting. Based on this understanding and our observations, it follows that inclusion, and thus quantum efficiency, appears to prefer fast crystal growth. Also supporting this hypothesis, attempts to thermally anneal Br6A/Br6 mixed crystals led to reduced quantum efficiency in all cases.

Achieving efficient inclusion also becomes an issue in color tuning. In earlier work broad changes to emission color were accomplished by altering the electron density of the emitter through the addition of electron deficient or rich atoms or extended conjugation.[14] As these chemical structures strayed from the original models inclusion became more complicated and quantum efficiencies suffered. For example, in the case of the blue-emitting alkyl substituted compounds, inclusion efficiency was problematically low, in large part because the aldehyde had a freezing point below room temperature. A more elegant, and subtler, approach to color tuning would be to simply vary the halogen atom of the emitters. Such compounds were synthesized to explore the effects halogen variation would have on emission color. Alternative emitters 4-chloro-2,5-dihexyloxybenzaldehyde (Cl6A) and 2,5-dihexyloxy-4-iodobenzaldehyde (I6A) have non-bromine halogens while 2,5-dihexyloxybenzaldehyde (H6A) was designed to be halogen-free (Figure 2.10a). Even though H6A is a halogen-free molecule it has the same core benzaldehyde unit that will form halogen bonding with bromine of matrix Br6, which activates the heavy atom effect. We excluded fluoride version because F does not form halogen bonding. These compounds alter the electron density of the emitter in ways that have less effect on the size, shape, and electronic character of the molecule and are thus less likely to alter pertinent materials properties such as the crystal growth mechanism and freezing temperature.

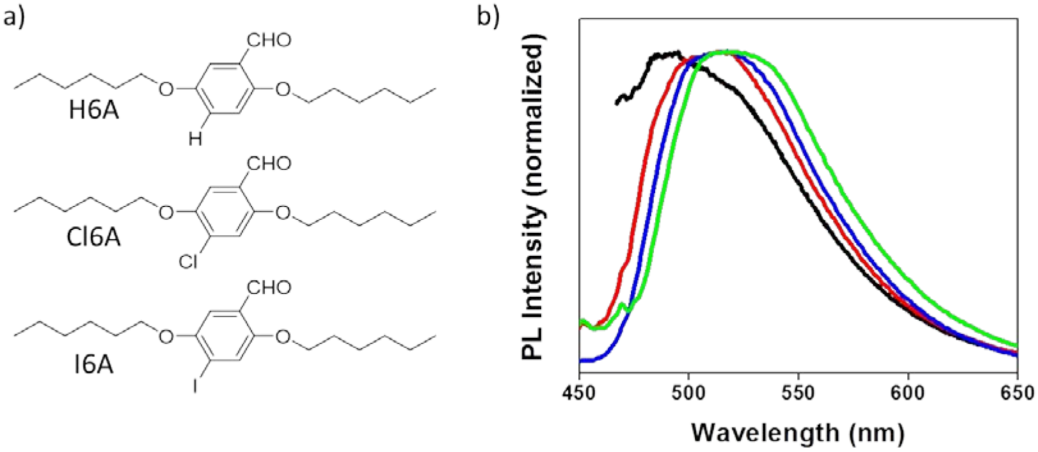

Figure 2.10. (a) Halogen-variable emitters for fine color tuning. (b) Emission (each excited at 365 nm) of crystals grown from solutions containing a 1 wt % ratio of the emitter in Br6. H6A (black), Cl6A (red), Br6A (blue), and I6A (green).

Each alternative aldehyde was included into Br6 host crystals and measured spectrally. Br6 was chosen as the host when it was observed to produce brighter samples than either 1,4-dichloro-2,5-dihexyloxybenzne (Cl6) or 1,4-diiodo-2,5-dihexyloxybenzene (I6). Mixed crystals of Br6 were grown by dropcasting chloroform solutions of 1 wt % emitter/Br6 onto unmodified glass. As shown in Figure 2.10b, varying the halogen from chlorine to bromine to iodine shifts the emission spectrum in sequential 5 nm steps ($\lambda_{\text{max, Cl6A}}$: 510nm, $\lambda_{\text{max, Br6A}}$: 515nm, $\lambda_{\text{max, I6A}}$: 520nm) commensurate with the varying electron density afforded by the halogen. Halogen-free emitter, H6A, produces an emission spectrum with a more dramatic 30 nm blue shift ($\lambda_{\text{max, H6A}}$: 485nm), which is because of the more dramatically reduced electron density this emitter exhibits for having no halogen.

We measured phosphorescence lifetime of guest emitters (Cl6A, Br6A, and I6A) in their analogous hosts (Cl6, Br6, and I6) at room temperature (Table 2.2). The phosphorescence lifetime of guest emitters decreases when the halogen of the host becomes heavier from Cl6 through Br6 to I6 likely due to enhanced heavy atom effect between halogen atom of the host and oxygen of the emitter. This lifetime decrease was maximized at I6/I6A mixed crystals because it contains the heaviest atom, iodine, both in host and emitter. When combined with the broader color shifts presented in earlier work, these fine tuning steps give this family of organic phosphors the capability to fine-tune emission color with both breadth and precision.

Table 2.2. Phosphorescence lifetime (ms) of mixed crystals was estimated at room temperature by means of time-resolved phosphorescence measurement of 515 nm emission with single decay curve fitting

	Cl6	Br6	I6
Cl6A	6.62	6.19	4.76
Br6A	7.95	7.60	3.33
I6A	0.65	0.56	0.05

2.4. Conclusions

In summary, we have demonstrated the optimization of the quantum efficiency and fine-tuning of emission color from emerging metal-free purely organic phosphors. Quantum efficiency optimization relies on attaining efficient inclusion of the emitter into the host crystal, which is a kinetic equilibrium maximized when both components are similarly sized and the emitter is present at 1-10 wt %. Replacing or removing the halogen on the emitter facilitates sequential 5-30 nm steps in green emission region, allowing the designer to fine-tune the emission spectrum with minimal change to the chemical structure. These findings elucidate the complex optical and solid state behavior these materials exhibit and illustrate the extreme influence that material preparation has on their performance.

2.5. References

1. Xiao, L.; Chen ,L.; Qu, B.; Luo, J.; Kong, S.; Gong, Q.; Kido, J. *Adv. Mater.* **2011**, *23*, 926-952.
2. Yersin, H.; Rausch, A. F.; Czerwieniec, R.; Hofbeck, T.; Fischer, T. *Coord. Chem. Rev.* **2011**, *255*, 2622-2652.
3. Reineke, S.; Lindner, F.; Schwartz, G.; Seidler, N. Walzer, K.; Lüssem, B.; Leo, K. *Nature* **2009**, *459*, 234-239.
4. Evans, R. C.; Douglas, P.; Winscom, C. J. *Coord. Chem. Rev.* **2006**, *250*, 2093-2126.
5. Baldo, M. A.; Lamansky, S.; Burrows, P. E.; Thompson, M. E.; Forrest, S. R. *Appl. Phys. Lett.* **1999**, *75*, 4-6.
6. Baldo, M. A.; O’Brien, D. F.; You, Y.; Shoustikov, A.; Sibley, S.; Thompson, M. E.; Forrest, S. R. *Nature* **1998**, *395*, 151-154.
7. Wong, W.-Y.; Ho, C.-L. *Acc. Chem. Res.* **2010**, *43*, 1246-1256.
8. Dennler, G.; Scharber, M. C..; Brabec, C. J. *Adv. Mater.* **2009**, *21*, 1323-1338.
9. Shao, Y.; Yang, Y. *Adv. Mater.* **2005**, *17*, 2841-2844.
10. Ma, X.; Cao, J.; Wang, Q.; Tian, H. *Chem. Comm.* **2011**, *47*, 3559-3561.
11. Zhang, G.; Palmer, G. M.; Dewhirst, M. W.; Fraser, C. L. *Nat. Mater*. **2009**, *8*, 747-751.
12. Soutar, I.; Swanson, L.; Adamson, P. G.; Flint, N. J. *Macromol.* **2009**, *42*, 9153-9160.
13. Lammers, I.; Buijs, J.; van der Zwan, G.; Arinese, F.; Gooijer, C. *Anal. Chem.* **2009**, *81*, 6226-6233.
14. Bolton, O.; Lee, K.; Kim, H.-J.; Lin, K. Y.; Kim, J. *Nat. Chem.* **2011**, *3*, 205-210.
15. Lee, D.; Bolton, O.; Kim, B. C.; Youk, J. H.; Takayama, S.; Kim, J. *J. Am. Chem. Soc*. **2013**, *135*, 6325-6329.

16. Hirata, S.; Totani, K.; Zhang, J.; Yamashita, T.; Kaji, H.; Marder, S. R.; Watanabe, T.; Adachi, C. *Adv. Funct. Mater*. **2013**, *23*, 3386-3397.

17. Kwon, M. S.; Lee, D.; Seo, S.; Jung, J.; Kim, J. *Angew. Chem. Int. Ed*. **2014**, *53*, 11177-11181.

18. Xu, J.; Takai, A.; Kobayashi, Y.; Takeuchi, M. *Chem. Commun*. **2013**, *49*, 8447-8449.

19. Climent, C.; Alemany, P.; Lee, D.; Kim, J.; Casanova, D. *J. Phys. Chem. A* **2014**, *118*, 6914-6921.

20. Jäkle, F. *Chem. Rev.* **2010**, *110*, 3985-4022.

21. Zhang, G.; Fiore, G.L.; St. Clair, T. L.; Fraser, C.L. *Macromol.* **2009**, *42*, 3162-3169.

22. Zhang, G.; Chen, J.; Payne, S. J.; Kooi, S. E.; Demas, J. N.; Fraser, C. L. *J. Am. Chem. Soc.* **2007**, *129*, 8942-8943.

23. Chaudhuri, D.; Wettach, H.; van Schooten, K. J.; Liu, S.; Sigmund, E.; Höger, S.; Lupton, J. M. *Angew. Chem. Int. Ed.* **2010**, *49*, 7714-7717.

24. Gao, L.; Peay, M. A.; Partyka, D. V.; Updegraff, J. B.; Teets, T. S.; Esswein, A. J.; Zeller, M.; Hunter, A. D.; Gray, T. G. *Organometallics* **2009**, *28*, 5669-5681.

25. Burress, C. N.; Bodine, M. I.; Elbjeirami, O.; Reibenspies, J. H.; Omary, M. A.; Gabbai, F. P. *Inorg. Chem.* **2007**, *46*, 1388-1395.

26. Jayaraj, N.; Maddipatla, M. V. S. N.; Prabhakar, R.; Jockusch, S.; Turro, N. J.; Ramamurthy, V. *J. Phys. Chem. B* **2010**, *114*, 14320-14328.

27. Evans, R.C.; Douglas, P.; Winscom, C. J. *J. Fluorescence* **2009**, *19*, 169-177.

28. Kuzmanich, G.; Simoncelli, S.; Gard, M. N.; Spänig, F.; Hender Henderson, B. L.; Guldi, D. M.; Garcia-Garibay, M. A. *J. Am. Chem. Soc.* **2011**, *133*, 17296-17306.

29. Yuan, W. Z.; Shen, X. Y.; Zhao, H.; Lam, J. W. Y. ; Tang, L. ; Lu, P.; Wang, C.; Liu, Y.; Wang, Z.; Zheng, Q.; Sun, J. Z.; Ma, Y.; Tang, B. Z. *J. Phys. Chem. C* **2010**, *114*, 6090-6099.
30. Kabe, R.; Lynch, V. M.; Anzenbacher, P., Jr. *CrystEngComm* **2011**, *13*, 5423−5427.
31. Shen, Q. J.; Wei, H. Q.; Zou, W. S.; Sun, H. L.; Jin, W. J. *CrystEngComm* **2012**, *14*, 1010-1015.
32. Yan, D.; Delori, Am.; Lloyd, G. O.; Friščić, T.; Day, G. M.; Jones, W.; Lu, J.; Wei, M.; Evans, D. G.; Duan, X. *Angew. Chem. Int. Ed.* **2011**, *50*, 12483-12486.
33. Li, J.; Takaishi, S.; Fujinuma, N.; Endo, K.; Yamashita, M.; Matsuzaki, H.; Okamoto, H.; Sawabe, K.; Takenobu, T.; Iwasa, Y. *J. Mater. Chem.* **2011**, *21*, 17662-17666.
34. Maity, S. K.; Bera, S.; Paikar, P.; Pramanik, A.; Haldar, D. *Chem. Commun*. **2013**, *49*, 9051-9053.
35. Martinez-Martinez, V.; Llano, R. S.; Furukawa, S.; Takashima, Y.; Arbeloa, I. L.; Kitagawa, S. *ChemPhysChem* **2014**, *15*, 2517-2521.
36. Wang, H.; Hu, R. X.; Pang, X.; Gao, H. Y.; Jin, W. J. *CrystEngComm* **2014**, *16*, 7942-7948.
37. Voth, A. R.; Hays, F. A.; Ho, P. S. *Proc. Natl. Acad. Sci.* **2007**, *104*, 6188-6193.
38. Politzer, P.; Lane, P.; Concha, M. C.; Ma, Y.; Murray, J. S. *J. Mol. Model* **2007**, *13*, 305-311.
39. Hassel, O. *Science* **1970**, *170*, 497-502.
40. Turro, N. J. *Modern Molecular Photochemistry*; University Science Books, 1991, pp 125.
41. Kearns, D. R.; Case, W. A. *J. Am. Chem. Soc.* **1966**, *88*, 5087-5097.
42. Fischer, M.; Georges, J. *Chem. Phys. Lett.* **1996**, *260*, 115-118.

CHAPTER 3

Room Temperature Phosphorescence of Metal-Free Organic Materials in Amorphous Polymer Matrices

This chapter suggests one valid strategy to efficiently suppress triplet vibration of purely organic phosphor. Bright room temperature phosphorescence is reported by embedding an organic phosphor into an amorphous glassy polymer matrix. Our study implies that the reduced beta-relaxation of isotactic PMMA most efficiently suppresses vibrational decay and allows achieving 7.5% phosphorescence quantum yield. This novel phosphorescent material shows temperature dependent emission property if temperature approaches polymer’s glass transition temperature because polymer is not rigid at that temperature. This feature enables to be utilized as a temperature sensor in microfluidic devices having a number of advantages such as simple structure, reversible response, and no need for additional sensing agent.

Parts of this chapter appear in: Lee, D.; Bolton, O.; Kim, B. C.; Youk, J. H.; Takayama, S.; Kim, J. *J. Am. Chem. Soc*. **2013**, *135*, 6325-6329.

3.1. Introduction

Phosphorescent materials have attracted much attention due to potential applications in display, solid state lighting, optical storage and sensors because they can theoretically realize threefold higher internal quantum efficiency than fluorescent alternatives by harvesting triplet excitons through intersystem crossing.[1-4] There are two critical processes in photoluminescent (PL) phosphorescence: (i) spin flipping from an excited singlet state to a triplet state and (ii) radiative decay from the excited triplet state to the ground state. Many organometallic compounds are efficient phosphors since both processes are promoted by spin-orbit coupling present in metals.[5,6] While these materials exhibit high quantum efficiency, they require rare and expensive elements such as platinum and iridium. In contrast, purely organic phosphorescent compounds are cheaper but generally weaker and relatively rare because they exhibit long-lived triplets that are easily consumed by vibrational effects, preventing emissive decay. Thus, one of the challenges that organic compounds must overcome in order to become competitive with organometallic phosphors is finding a way to suppress vibration in order to achieve bright emission.

Aromatic ketones such as benzophenone are well-known phosphorescent materials that have been studied for several decades.[7] Excited state electrons in aromatic ketones cross from S_1 to T_2 at very high efficiency because of strong spin−orbit coupling and triplet T_2 levels that are often close in energy to S_1.[8] This spin−orbit coupling is localized at the carbonyl oxygen.[9] Because of this, aromatic ketones are an attractive moiety for designing metal-free organic phosphors. In order for the triplet to survive long enough for phosphorescence, vibrational dissipation from T_1 to the ground state must be suppressed as it competes with phosphorescent decay. Adequately suppressing vibration is perhaps the most important and challenging aspect of achieving efficient organic phosphorescence at room temperature.

Yuan et al. observed purely organic phosphorescence from benzophenone and its halogenated derivatives by growing crystals in common organic solvents.[10] Moreover, Bolton et al. developed color-tunable organic phosphorescence materials by implementing a directed heavy atom effect with halogen atoms also in crystalline systems.[11] In this material design, strong halogen bonding between the oxygen atom of an aromatic carbonyl and bromine promotes spin−orbit coupling and suppresses vibrational dissipation at the same time by the strict order of the crystal states of the materials. Though these approaches are very promising for developing metal-free organic phosphors, they still have limitations to practical applications because they stringently require crystalline materials.[12] Film forming materials, such as polymers and amorphous solids, would be more attractive for device fabrication and processing; however, a means must be found to induce in these systems vibrational suppression that is on par with that generated by crystals.

Herein we report our systematic investigation to deconvolute the suppression of the vibrational dissipation from the spin orbit coupling enhancement by embedding a purely organic triplet-generating small molecule into a glassy polymer film and demonstrate bright metal-free organic phosphorescence from amorphous materials. The polymer serves as a rigid matrix to suppress vibration in the small molecule phosphor, as would a crystal, and thus allows the long-living triplets of the organic compound to survive long enough to emit. This phenomenon was studied using a single phosphorescent compound in various glassy polymer matrixes. We systematically investigated the correlation between the emission intensity of the embedded organic phosphors and physicochemical properties of the matrix polymers. Our study reveals that solubility parameter matching between the phosphorescent compound and the polymer matrix is a critical requirement to achieve a well-mixed embedding of the chromophore into the polymer and facilitate emission. Also, phosphorescence efficiency is strongly dependent on polymer tacticity because each arrangement exhibits a different degree of β-relaxation, which greatly affects the vibrational dissipation of the excited state triplets. This lifts the stringent crystalline requirement for metal-free organic phosphorescence materials and provides more process-friendly medium and a more physically tunable matrix.

We also demonstrated the use of amorphous purely organic phosphor films as a temperature sensor in a microfluidic device. Accurate temperature control is essential in such devices as they are often used for biological applications.[13] In this application, organic phosphors have many advantages over other conjugated polymer-based temperature sensors: (i) simple device structures, that is, no need for additional inlet to feed temperature sensing agents, (ii) brighter emission from phosphorescence as compared with polydiacetylene (PDA)-based fluorescence, (iii) a wholly reversible thermal response, and (iv) tunable temperature sensing ranges by using different polymer. This is the first example showing metal-free organic phosphorescence in an amorphous material, demonstrating its attractiveness as a temperature sensor in microfluidic devices. Moreover, we expect that this system can also be utilized in other biomedical applications due to the biocompatibilities of each component. Furthermore, developing appropriate conducting polymers as a glassy matrix for the organic phosphorescence materials may realize bright, color tunable, and flexible phosphorescent organic light emitting diodes as well.

3.2. Experimental Section

3.2.1. Materials

Isotactic PMMA (iPMMA) (Aldrich, M_w = 120 kg/mol), syndiotactic PMMA (sPMMA) (Aldrich, M_w = 996 kg/mol), atactic PMMA (aPMMA) (Aldrich, M_w = 15 kg/mol), Polypropylene (PP) (Aldrich, M_w = 174 kg/mol), and poly(hexamethylene adipamide) (Nylon 6/6, Aldrich) were used as polymer matrix without further purification. 2,2,2-Trifluoroethanol (Aldrich) and toluene (Aldrich) were used as solvents for Nylon 6/6 and PP, respectively, without further purification. An organic phosphor, Br6A, was synthesized following previously reported synthetic routes.[11]

3.2.2. Solubility Parameter Calculation

Solubility parameter of Br6A was calculated by group contribution method.[31] The dispersive, polar, and hydrogen-bonding parameters from the Hoftyzer and van Krevelen's table were used by simple additive rules. Hildebrand parameter of PP, poly(hexamethylene adipamide) (Nylon 6/6) and PMMA was used to estimate polymer's solubility parameter.[32]

3.2.3. PL and QY Measurement

PL emission, excitation and quantum yield (QY) were collected using a Photon Technologies International (PTI) Quantamaster system equipped with an integrating sphere. Samples for quantum yield measurement were prepared by dropping mixed solution with chloroform onto an unmodified glass substrate followed by annealing at 90 °C for 20 min. Absorption and emission inside the sphere were determined by comparison to a blank sample (glass only). A neutral density filter was used to allow for maximization of the emission signal without saturating the photomultiplier tube detector with excitation light. Each sample type was run in quadruplicate with each quantum yield measurement coming from a freshly drop cast sample. Measurements proved highly repeatable, and errors are given as ±1 standard deviation.

3.2.4. Microfluidic Device Preparation

A “Y” shaped microchannel structure was fabricated using a conventional soft lithography technique. A transparent mask (CAD Art Inc.) bearing the channel pattern was transferred to SU-8 (Microchem Inc.) deposited on a silicon wafer. A 10:1 mixture of PDMS (Sylgard 184, Dow corning) and curing agent was poured onto the mold and cured at 60 °C for at least 4 h before use. Phosphorescence layer was prepared by homogeneously drop casting 100:1 mixture of iPMMA and Br6A on a slide glass followed by annealing at 90 °C for 20 min. Afterward, the PDMS layer and the phosphorescence layer were bonded together by plasma treatment (COVANCE-MP, Femto-science Inc.). The microchannel device was soaked in a hot water bath, heated up to 60 °C to reduce the emitted light intensity from the device. Then hot (60 °C) and cold (4 °C) water was supplied through two separate inlets into the microchannel to generate laminar flow inside the channel with a thermal gradient induced at the boundary. Emitted light intensity from the device was measured by a fluorescence microscope (Ti, Nikon).

3.2.5. Temperature Dependent Emission Measurement

Emitted light intensity from a film of 100:1 mixture of iPMMA and Br6A was measured using a plate reader (BioTeck Synergy Neo plate reader) under controlled temperature conditions. Repetitive measurements of the emission were conducted to record the cyclic intensity changes between high temperature and low temperature conditions.

3.3. Results and Discussion

The weakly emitting organic phosphor, 2,5-dihexyloxy-4-bromobenzaldehyde (Br6A, Figure 3.1a), was embedded into atactic poly(methyl methacrylate) (aPMMA) resulting in a thin film with green phosphorescence. Alone, microcrystalline films of Br6A produce very weak emission that is largely dominated by the weak blue fluorescence of the compound seen at 425 nm. In films the phosphorescent quantum yield of Br6A increased from essentially zero to detectable level of 0.7% at room temperature. The increase in phosphorescent emission at 520 nm from the polymer film is evidence that the PMMA is acting to suppress vibration and enhance emissive triplet relaxation (Figure 3.1b).

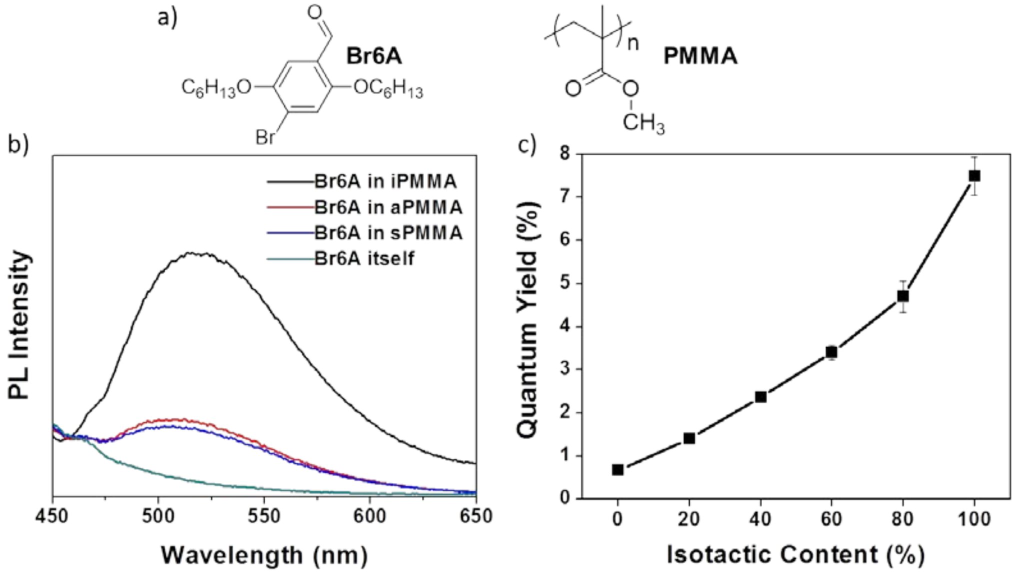

Figure 3.1. (a) Structure of a phosphor (Br6A) and polymer (PMMA). (b) PL emission spectra of Br6A and Br6A embedded in iPMMA, aPMMA and sPMMA. (c) Phosphorescence quantum yield with various isotactic content. The excitation wavelength was 365 nm.

Assuming that a more well-ordered rigid polymer would restrict vibration even more efficiently, we tested polymers with higher degrees of crystallinity such as polypropylene (PP) and poly(hexamethylene adipamide) (Nylon 6/6). However, the quantum yield for these films was below our detection limit (<0.1%) for both cases. We believe that this is because the solubility parameter of these polymers (16.0 MPa$^{1/2}$ and 27.8 MPa$^{1/2}$, respectively) does not match with that of the phosphor (18.8 MPa$^{1/2}$) and, thus, the phosphor does not become sufficiently embedded into these polymer films. As a result, the phosphor molecules do not get the benefit of the polymer rigidity and are not emissive due to vibrational dissipation. On the contrary, PMMA has a solubility parameter of 19.0 MPa$^{1/2}$ that is similar to that of the phosphor, indicating that the phosphor is well mixed into that polymer matrix.

Notably, we found that the quantum efficiency of Br6A in PMMA strongly depends on polymer tacticity. Br6A embedded in isotactic PMMA (iPMMA) shows 10-fold brighter phosphorescence at room temperature than the same amount of Br6A in aPMMA or syndiotactic PMMA (sPMMA), as shown in Figure 3.1b. Indeed, as the relative amount of iPMMA present in the host polymer increases from 0 to 100% an exponential trend is observed as the quantum efficiency climbs from 0.7 to 7.5% (Figure 3.1c). This is attributed to the β-relaxation behavior of these polymers. β-Relaxation is considered to be the onset of motions that initiate the long-range segmental motions occurring at T_g.[14] In PMMA, this is caused by the onset of rotation of the ester side group, appearing around 285−300 K.[15] The intensity of the β-relaxation in amorphous PMMA increases with increasing syndiotacticity but decreases with increasing isotacticity.[16] Dominant β-relaxation in aPMMA and sPMMA means there is independent motion of the carbonyl dipole in the ester side group. As the isotacticity increases, the β loss peak vanishes, indicating that the carbonyl dipole motion is locked. The rotation energy was calculated by using Allinger "MM2" force field model, showing that the rotating side group of iPMMA must force the two adjacent ester groups to undergo torsional oscillations of ±16° to relieve the stress during rotation of the central group leading to more activation energy (110 kJ mol^{-1}) than aPMMA (80 kJ mol^{-1}) and sPMMA (91 kJ mol^{-1}).[15]

Figure 3.2 shows the effect of β-relaxation. As sample temperatures decrease, phosphorescence intensity increases. The previously reported rigidity spectra show that the most significant β-relaxation appears around at 300 K and decreases with decreasing temperature.[17]

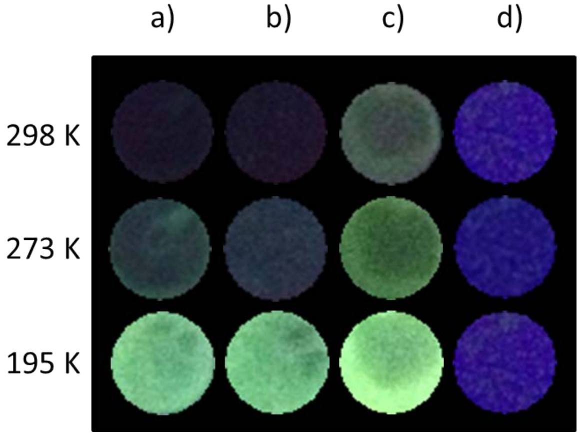

Figure 3.2. Phosphorescence emission of Br6A embedded in (a) aPMMA, (b) sPMMA, and (c) iPMMA at different temperatures. (d) Blue fluorescence emission of pure Br6A visible in part due to a lack of green phosphorescence also at these temperatures. The excitation wavelength was 365 nm.

We can see bright emission at lower temperatures from samples on ice (273 K) or on dry ice (195 K). However, even when the temperature is dropped to 195 K, the phosphor itself (not in PMMA) does not emit brightly, as shown in Figure 3.2d where only the inherent deep-blue fluorescence of Br6A is visible, which is indicative of disordered chromophores.[11] From these observations, we hypothesize that phosphorescence efficiency is dependent on the degree of β-relaxation and, thus, can be enhanced by lowering temperature, which restricts β-relaxation.

An optimum phosphor concentration was found to be 1 wt % versus polymer mass as shown in Figure 3.3a. At high concentrations of phosphor, self-quenching is expected and is believed to cause the observed low emission. At very low concentrations, there is much less opportunity for molecules of Br6A to find one another and realize the emission enhancing benefits of halogen bonding. So, though the aforementioned solubility parameter matching indicates that a high degree of miscibility is required to achieve adequate phosphor/polymer mixing, this result suggests that phosphor molecules can also suffer from too much isolation/mixing, indicating that some phosphor contact is necessary to achieve phosphorescence.

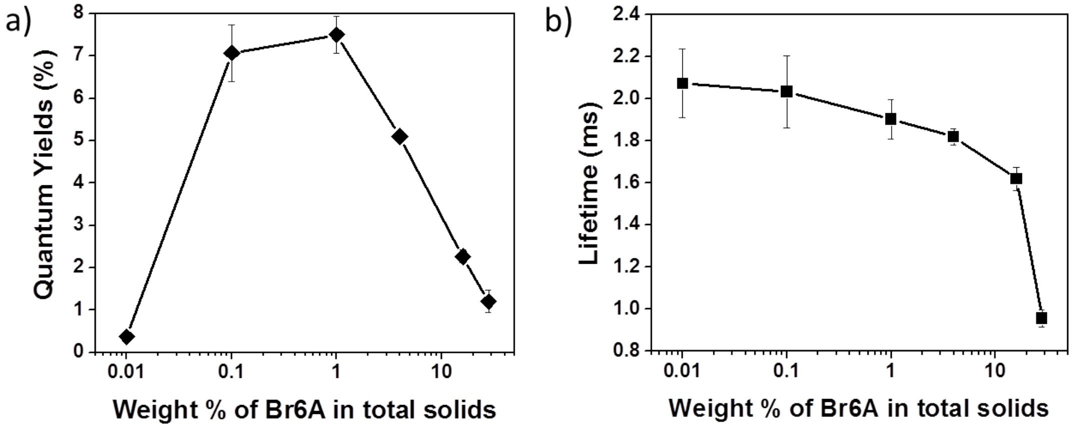

Figure 3.3. (a) Phosphorescence quantum yield at different phosphor concentrations for Br6A embedded in iPMMA. (b) Phosphorescence lifetime at different phosphor concentrations. Samples were annealed at 90 °C for 20 min. The excitation wavelength was 365 nm, and lifetime was monitored by the emission wavelength at 520 nm.

At lower concentrations, as the concentration increases the chance for the halogen bonding increases, resulting in more efficient heavy atom effect and halogen bonding. To prove this hypothesis, we measured the phosphorescence lifetime of various concentrations of Br6A mixed into PMMA. As the phosphor concentration increases, the phosphorescence quantum yield increases, indicating that more halogen bonding facilitates intersystem crossing. Increasing halogen bonding up to a 1 wt % mixing ratio made radiative decay more dominant, resulting in high quantum yield and relatively short lifetime. But at higher concentrations nonradiative self-quenching dominates over radiative decay, the overall radiative rate decreases, and quantum yield falls faster than lifetime does.

In this study, we found solubility parameter matching and suppressing β-relaxation to be key components to reduce vibrational loss of phosphor triplets. Also, bright phosphorescence was realized by choosing a proper polymer matrix, iPMMA, and optimized mixing ratio between an organic phosphor and a polymer matrix. Moreover, we expect that this system can be utilized in organic light emitting diodes if a phosphor is embedded in appropriate conducting polymers as a glassy matrix.

This novel amorphous phosphorescence is strongly dependent on ambient temperature so that it can be useful as a temperature sensor. Accurate temperature measurements are difficult but critical in microfluidic devices performing biological processes such as polymerase chain reaction (PCR), temperature gradient focusing (TGF), and enzyme-activated reactions.[18–22] PDA-based conjugated polymers have been recently demonstrated as potential microfluidic temperature sensors by reporting fluorescent intensities correlated to the temperature of the PDA droplet.[13] Composite blends of PDA and a proper polymer matrix enable reversible fluorescence by increasing the stability of the PDAs.[23,24] However, the PDA must be kept separate from the reaction mixture and complicated channel structure must be used to make an additional inlet to feed PDA molecules. Polymer-based microfluidic devices feature low manufacturing costs and can be made from a wider range of materials that can be tailored for specific applications, as opposed to glass or silicon.[25] Polymers such as PMMA are popular construction materials for such microfluidic devices due to good processability, chemical resistance against acids and oils, and low cost.[26–28] Coining in situ temperature sensing in devices made from such a material would, ideally, not compromise the attractive qualities of the polymer, be easy to incorporate without the need of new device structure, and be economically on par with low-cost plastics.

While organometallic phosphors exhibit high quantum efficiency they are often, due to the short lifetimes of their triplets, relatively unaffected by temperature changes in the biologically relevant 30−60 °C range.[29,30] Also the vibrational freedoms of crystalline systems are largely unaffected by noncryogenic temperature changes below their melting points, making them poor near-ambient temperature sensors in their crystalline forms. However, embedding similar organic phosphor compounds into more temperature-sensitive matrices, such as polymers, offers the possibility of enhancing the effect of temperature on phosphorescent emission intensity in ways that can be exploited for temperature sensing. Thus, these PMMA films of purely organic phosphors were explored as sensitive, inert, and cheap temperature sensors. As the sample temperature approaches the glass transition point of iPMMA, 55 °C, phosphorescence intensity decreases nearly linearly. As is shown in Figure 3.4, this creates a dramatic and predictable change in emission intensity across the temperature range of approximately 30−60 °C.

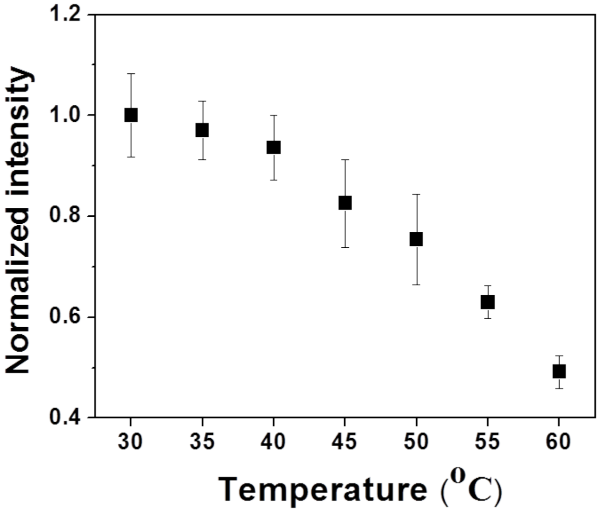

Figure 3.4. Normalized emission intensities for Br6A embedded in iPMMA at different temperatures excited at 365 nm.

The in situ phosphorescence spectra in a heating and cooling cycle in the temperature range of 30−60 °C were recorded in order to monitor thermal response reversibility. Faster decrease in phosphorescent intensity as temperature increases with relatively slower increases in phosphorescent intensity as temperature decreases were observed (Figure 3.5a). Incomplete intensity recovery seen in the first cooling cycle is probably ascribed to residual transitional motion of the fresh polymer occurring at higher temperatures. Following the first heating, reversible phosphorescence was repeated in six consecutive cycles, indicating that temperature sensing in microfluidic devices using this system can be reusable (Figure 3.5b).

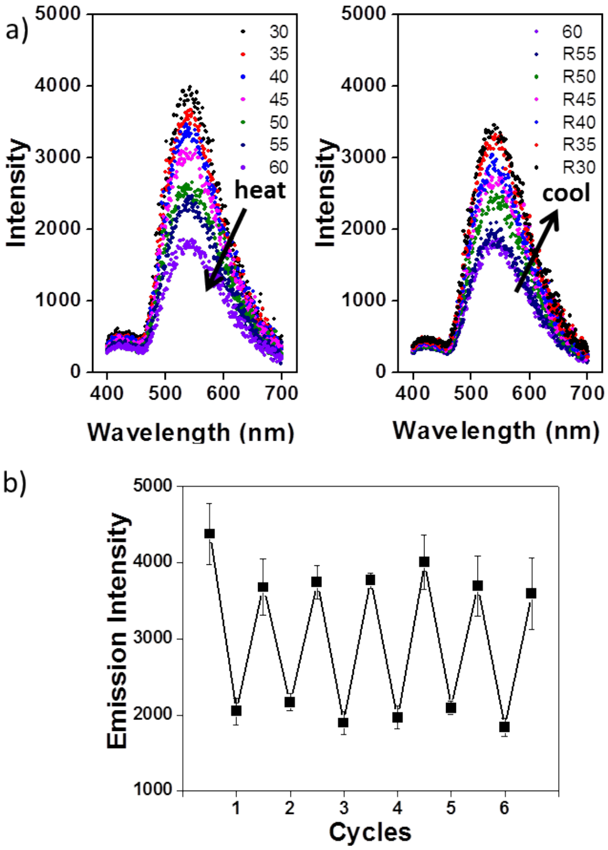

Figure 3.5. (a) In situ phosphorescence spectra in a heating and cooling cycle in the temperature range of 30−60 °C. (b) In situ phosphorescence intensities during six cycles. The excitation wavelength was 365 nm.

In Figure 3.6 is demonstrated a microfluidic device composed of a polydimethylsiloxane (PDMS) channel on a glass slide coated with Br6A embedded in iPMMA. The microchannel device was soaked in a hot water bath heated to 60 °C to reduce the phosphorescence emission intensity from the device. Next, hot (60 °C) and cold (4 °C) water was supplied through two separate inlets into the microchannel to generate laminar flow inside the channel with a thermal gradient induced at the boundary. As shown in the fluorescence microscope image and the inserted graph, due to the temperature gradient created across the 200 µm wide channel, the phosphorescence emission intensity increases linearly from the side of the channel having hot water to the cold side of the channel.

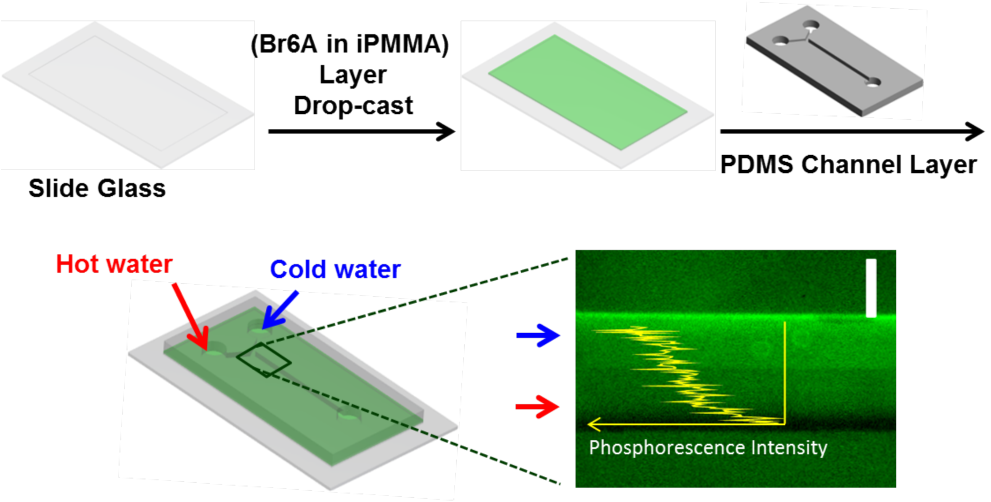

Figure 3.6. Schematic fabrication process and operation of a microfluidic device composed of a phosphorescence layer (Br6A in iPMMA) and a PDMS channel layer. Phosphorescence emission intensity under 365 nm UV light increases linearly from the hot side of the channel to the cold side channel. Scale bar = 100 µm.

3.4. Conclusions

In summary, we have realized efficient phosphorescence at room temperature by embedding a purely organic phosphor, Br6A, into glassy PMMA matrices. The activation of phosphorescence is likely due to fairly efficient restriction of vibrational decay due to the rigidity of the polymer matrix. Through systematic investigation we found that the tacticity of PMMA strongly affects quantum efficiency of the embedded organic phosphors. Our study implies that the reduced β-relaxation of iPMMA most efficiently suppresses the vibrational decay and allows the embedded organic phosphors to achieve a bright 7.5% phosphorescence quantum yield. We also demonstrated a novel temperature sensor based on metal-free organic phosphorescence which is established by embedding a phosphor in a glassy polymer matrix, iPMMA. Organic phosphors are useful here because emission from the long-lived triplets they generate is dictated by vibrational suppression in the temperature-sensitive polymer matrix. This unique system has many advantages over conjugated polymer-based alternatives. This is also the first example showing amorphous metal-free organic phosphorescence, which is uniquely practical as a temperature sensor in microfluidic devices. We expect that this system can be especially useful in biomedical applications due to biocompatibilities of each component.

3.5. References

1. Tang, C. W.; VanSlyke, S. A. *Appl. Phys. Lett.* **1987**, *51*, 913−915.
2. Baldo, M. A.; O'Brien, D. F.; You, Y.; Shoustikov, A.; Sibley, S.; Thompson, M. E.; Forrest, S. R. *Nature* **1998**, *395*, 151−154.
3. Adachi, C.; Baldo, M. A.; Forrest, S. R.; Thompson, M. E. *Appl. Phys. Lett.* **2000**, *77*, 904−906.
4. You, Y.; Han, Y.; Lee, Y.-M.; Park, S. Y.; Nam, W.; Lippard, S. J. *J. Am. Chem. Soc.* **2011**, *133*, 11488−11491.

5. Lamansky, S.; Djurovich, P.; Murphy, D.; Abdel-Razzaq, F.; Lee, H.; Adachi, C.; Burrows, P. E.; Forrest, S. R.; Thompson, M. E. *J. Am. Chem. Soc*. **2001**, *123*, 4304−4312.
6. Niu, Y.; Tung, Y.; Chi, Y.; Shu, C.; Kim, J. H.; Chen, B.; Luo, J.; Carty, A. J.; Jen, A. K. *Chem. Mater*. **2005**, *17*, 3532−3536.
7. Kearns, D. R.; Case, W. A. *J. Am. Chem. Soc*. **1966**, *88*, 5087−5097.
8. Kiritani, M.; Yoshii, T.; Hirota, N.; Baba, M. *J. Chem. Phys*. **1994**, *98*, 11265−11268.
9. Klessinger, M.; Michl, J. *Excited States and Photochemistry of Organic Molecules*; VCH Publishers: New York, **1995**; pp 266−271.
10. Yuan, W. Z.; Shen, X. Y.; Zhao, H.; Lam, J. W. Y.; Tang, L.; Lu, P.; Wang, C.; Liu, Y.; Wang, Z.; Zheng, Q.; Sun, J. Z.; Ma, Y.; Tang, B. Z. *J. Phys. Chem. C* **2010**, *114*, 6090−6099.
11. Bolton, O.; Lee, K.; Kim, H.-J.; Lin, K. Y.; Kim, J. *Nat. Chem*. **2011**, *3*, 205−210.
12. Kabe, R.; Lynch, V. M.; Anzenbacher, P., Jr. *CrystEngComm* **2011**, *13*, 5423−5427.
13. Ryu, S.; Yoo, I.; Song, S.; Yoon, B.; Kim, J.-M. *J. Am. Chem. Soc*. **2009**, *131*, 3800−3801.
14. Mark, J. E., Ed. *Physical Properties of Polymers Handbook*; Springer: New York, **2007**, pp 217−232.
15. Cowie, J. M. G.; Ferguson, R. *Polymer* **1987**, *28*, 503−508.
16. Gillham, J. K.; Boyer, S. J. R. F. *Polymer* **1976**, *17*, 996−1008.
17. Gillham, J. K.; Stadnicki, S. J. *J. Appl. Polym. Sci*. **1977**, *21*, 401−424.
18. Lagally, E. T.; Medintz, I.; Mathies, R. A. *Anal. Chem*. **2001**, *73*, 565−570.
19. Mao, H.; Yang, T.; Cremer, P. S. *J. Am. Chem. Soc*. **2002**, *124*, 4432−4435.

20. Ross, D.; Gaitan, M.; Locascio, L. E. *Anal. Chem.* **2001**, *73*, 4117−4123.
21. Ross, D.; Locascio, L. E. *Anal. Chem.* **2002**, *74*, 2556−2564.
22. Kim, S. M.; Sommer, G. J.; Burns, M. A; Hasselbrink, E. F. *Anal. Chem.* **2006**, *78*, 8028−8035.
23. Lee, S.; Lee, J.; Kim, H. N.; Kim, M. H.; Yoon, J. *Sens. Actuators, B* **2012**, *173*, 419−425.
24. Wang, X.-D.; Song, X.-H.; He, C.-Y.; Yang, C. J.; Chen, G.; Chen, X. *Anal. Chem.* **2011**, *83*, 2434−2437.
25. Becker, H.; Locascio, L. E. *Talanta* **2002**, *56*, 267−287.
26. Henry, A. C.; Tutt, T. J.; Galloway, M.; Davidson, Y. Y.; McWhorter, C. S.; Soper, S. A.; McCarley, R. L. *Anal. Chem.* **2000**, *72*, 5331−5337.
27. McCormick, R. M.; Nelson, R. J.; Alonso-Amigo, M. G.; Benvegnu, D. J.; Hooper, H. H. *Anal. Chem.* **1997**, *69*, 2626−2630.
28. Becker, H.; Heim, U. *Sens. Actuators, A* **2000**, *83*, 130−135.
29. Borisov, S. M.; Wolfbeis, O. S. *Anal. Chem.* **2006**, *78*, 5094−5101.
30. Borisov, S. M.; Vasylevska, A. S.; Krause, C.; Wolfbeis, O. S. *Adv. Funct. Mater.* **2006**, *16*, 1536−1542.
31. Brandrup, J., Immergut, E. H., Grulke, E. A., Eds. *Polymer Handbook*; Wiley-Interscience, New York, **1999**; pp 682−686.
32. Barton, A. F. M. *Handbook of Polymer-Liquid Interaction Parameters and Solubility Parameters*; CRC Press: Boca Raton, FL, **1990**; pp 265−284.

CHAPTER 4

Tailoring Intermolecular Interactions for Efficient Room-Temperature Phosphorescence from Purely Organic Materials in Amorphous Polymer Matrices

This chapter describes more efficient strategy to suppress triplet vibration of purely organic phosphor. Rather than using Van der Waals interaction between polymer matrix and phosphor discussed in Chapter 3, we introduced strong hydrogen bonding by synthesizing a functionalized phosphor and choosing a new polymer having hydrogen bonding capability. In this work, 24% of high phosphorescence is demonstrated. Interestingly, modulation of hydrogen bonding by water molecules showed unique reversible phosphorescence-to-fluorescence switching behavior, which can be utilized as a ratiometric water sensor.

Parts of this chapter appear in: Kwon*, M. S.; Lee*, D.; Seo, S.; Jung, J.; Kim, J. *Angew. Chem. Int. Ed.* **2014**, *53*, 11177-11181.

4.1. Introduction

Purely organic materials that show room-temperature phosphorescence (RTP) are attractive alternatives to organometallic phosphors. They have a few potential advantages over their organometallic counterparts: Organometallic compounds are expensive and conceivably toxic owing to the presence of metals, and are also intrinsically unstable in the case of high-energy blue emitters.[1] However, unfortunately, purely organic RTP has been only observed from particular organic molecules[2–4] and under stringent conditions[5–8] because triplet excitons are not commonly generated in light-element organic materials, and those few are mostly consumed through radiationless processes, such as vibrational dissipation and oxygen-mediated quenching, under ambient conditions.[9, 10]

The key factors for the construction of efficient purely organic RTP materials are 1) the promotion of both singlet to-triplet and triplet-to-singlet intersystem crossing, and 2) suppression of the nonradiative quenching processes from the triplet to the ground state. Within this context, several research groups have shown that “crystal”[11–14] and/or “engineered crystal”[15] can be used to induce efficient purely organic RTP. The rigidity and oxygen-barrier properties of crystals suppress the nonradiative deactivation pathways of triplet excitons, and, as in our previous study, the directed intermolecular halogen bonding promotes the intersystem crossing processes by enhancing spin–orbit coupling.[12, 19]

Amorphous purely organic RTP systems, for example, phosphors embedded in polymers and/or amorphous solids, would be more promising for practical applications, such as organic light-emitting diodes (OLEDs), solid-state lightning, and sensors. However, bright organic RTP is a challenging goal in the amorphous phase because active vibration/diffusion motions, for example, b and a transitions, are generally inevitable in an amorphous matrix under ambient conditions. This unfavorable amorphous environment promotes the vibrational dissipation of long-lived triplets of embedded phosphors, thus resulting in the complete quenching of phosphorescence.[16, 17] Therefore, it remains a demanding and challenging task to devise a way of minimizing diffusional motion in an amorphous matrix to obtain highly emissive organic RTP. Recently, Adachi and co-workers developed a unique amorphous purely organic RTP system by adopting a highly deuterated fluorene derivative as a phosphorescent guest and its steroid analogue as a host matrix.[18] The considerable rigidity of the steroidal matrix combined with the heavy deuteration of phosphors synergistically suppressed the vibrational dissipation of long-lived triplets. Our research group recently demonstrated RTP in an amorphous organic material by embedding 2,5-dihexyloxy-4-bromobenzaldehyde (Br6A), an organic phosphor, in isotactic poly(methyl methacrylate) (iPMMA), a rigid polymer matrix, without b relaxation.[19] Although these strategies demonstrated that the restriction of vibration of both the matrix and phosphors is critically important for amorphous purely organic RTP, a more generally applicable and practically useful strategy to enable efficient suppression of vibration is highly desired.

Herein, we describe our rational and systematic approach to the development of an efficient amorphous purely organic RTP system. To minimize both the diffusion motion of the matrix and the vibration of phosphors, we intentionally included two types of strong intermolecular non-covalent interactions in the material (Figure 4.1). First, intermolecular halogen bonds between phosphors were introduced to facilitate intersystem-crossing processes as well as to suppress the vibration of phosphors. Second, strong intermolecular hydrogen bonds (H-bonds) between matrix polymers as well as between matrix polymers and phosphors were incorporated to restrict the vibration/diffusion motion of the matrix and phosphors more efficiently. Thus, we designed a new organic phosphor (G1) with a bromobenzaldehyde core and carboxylic acid side chains as a dopant. The bromobenzaldehyde core was expected to provide the structural basis for strong halogen bonding in the assembly as well as for triplet-exciton generation. The carboxylic acid periphery was expected to enable the formation of strong H-bonds between the phosphor and the selected amorphous matrix, that is, poly(vinyl alcohol) (PVA), which has H-bonding capability.

As anticipated, we observed strong RTP from G1–PVA blend films with phosphorescence quantum yield of up to 24% at ambient conditions, which is three times as high as that of previously reported Br6A–iPMMA blend amorphous films (Φ_{ph} = 7.5%). We also found that modulation of the H-bonding strength in the G1–PVA system by water molecules produced unique reversible “phosphorescence-to-fluorescence” switching behavior. Unlike traditional organometallic phosphors, our purely organic phosphors emit RTP not from an isolated species but from molecular assemblies because of the necessary intermolecular halogen bonding to enhance spin-orbit coupling. Thus, if external stimuli can break up the molecular assembly, the efficiency of spin–orbit coupling drops, thus resulting in fluorescence rather than phosphorescence emission. On the basis of this interesting stimuli-responsive change in optical properties, we could successfully demonstrate reversible direct writing of a fluorescent watermark and moisture sensing.

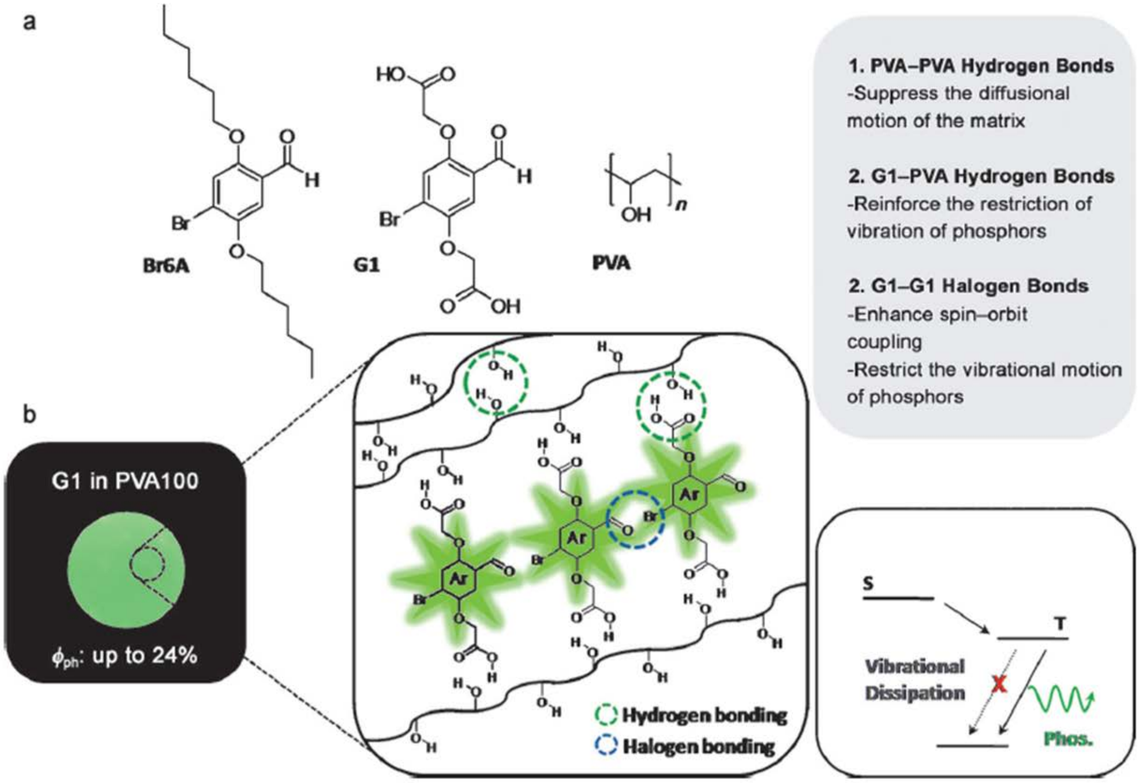

Figure 4.1. a) Chemical structures of Br6A, G1, and PVA. b) Phosphorescence image of G1 embedded in PVA100 under UV light (λ=365 nm; left) and schematic illustration of phosphorescence processes in the G1–PVA composite (right).

4.2. Experimental Section

4.2.1. Synthetic Procedure

2,2'-(2-bromo-5-formyl-1,4-phenylene)bis(oxy)diacetic acid (G1). Lithium hydroxide (38 mg, 0.780 mmol) dissolved in water (2.4 mL) was added to a solution of diethyl 2,2'-(2-bromo-5-formyl-1,4-phenylene)bis(oxy)diacetate (200 mg, 0.52 mmol) in THF (2.4 mL) and methanol (1.2 mL) at 0 °C. The solution was stirred at 0 ^{o}C for 4 h, and then poured into 1 M HCl aqueous solution. The resulting white precipitates were filtered and washed with water and methanol (158 mg, 92%). ^{1}H NMR (400 MHz, DMSO-d_6): δ 10.34 (s, 1H), 7.58 (s, 1H), 7.16 (s, 1H), 4.90 (s, 2H), 4.82 (s, 2H). ^{13}C NMR (100 MHz, DMSO-d_6): δ 188.4, 169.9, 169.7, 154.7, 149.0, 124.2, 120.0, 119.4, 110.0, 66.0, 65.6. MS *m/z* (EI, relative intensity): 332 (M^+, 3), 288 (4), 241 (2), 252 (69), 229 (14), 215 (87), 192 (52), 178 (32), 165 (99), 149 (67), 137 (69), 121 (25), 107 (44), 93 (14), 80 (100), 65 (21). HRMS $(ESI)^+$ *m/z* 331.9533 ($C_{11}H_9BrO_7$ [M^+] requires 331.9531).

2,2'-(2,5-dibromo-1,4-phenylene)bis(oxy)diacetic acid (G2). Lithium hydroxide (33 mg, 1.36 mmol) dissolved in water (1.8 mL) was added to a solution of diethyl 2,2'-(2,5-dibromo-1,4-phenylene)bis(oxy)diacetate (200 mg, 0.455 mmol) in THF (1.8 mL) and methanol (0.9 mL) at 0 °C. The solution was stirred at 0 ^{o}C for 8 h, and then poured into 1 M HCl aqueous solution. The resulting white precipitates were filtered and washed with water and methanol (160 mg, 86%). ^{1}H NMR (400 MHz, DMSO-d_6): δ 13.10 (s, 2H), 7.28 (s, 2H), 4.79 (s, 4H). ^{13}C NMR (100 MHz, DMSO-d_6): δ 169.8, 148.9, 118.0, 110.0, 65.8. MS *m/z* (EI, relative intensity): 410 (M^+, 16), 384 (1), 353 (7), 333 (31), 283 (5), 266 (16), 229 (3), 201 (6), 159 (2), 125 (3), 97 (9), 73 (63), 58 (44). HRMS $(ESI)^+$ *m/z* 409.8996 ($C_{12}H_{12}Br_2O_6$ [M^+] requires 409.9001).

4.2.2. Sample Preparation

Isotactic PMMA (iPMMA) (Aldrich, M_w = 120,000 g/mol), polyvinyl alcohol 80% hydrolyzed (PVA80) (Aldrich, M_w = 9,000 – 10,000 g/mol), polyvinyl alcohol 100% hydrolyzed (PVA100) (Aldrich, M_w = 89,000 – 98,000 g/mol), and polyvinyl acetate (PVAc) (Aldrich, M_n = 167,000 g/mol) were used as polymer matrix without further purification. Br6A was synthesized following previously reported synthetic routes.[12] Samples for quantum yield measurement were prepared by dropcasting chloroform solution on the unmodified glass.

4.2.3. Measurement and Characterization

^{1}H-NMR spectrum was recorded on a Varian MR400 (400 MHz) in DMSO-d_6 solution and ^{13}C-NMR spectrum was recorded on a Varian MR400 (100 MHz) in DMSO-d_6 solution. Chemical shift values were identified relative to 0.05 v/v% tetramethylsilane as an internal standard (0.00 ppm). Mass spectra were recorded on an Agilent Q-TOF 6520 system using electrospray in positive ion detection $(ESI)^+$ mode. Significant fragments are reported in the following fashion: *m/z* (relative intensity). Elemental analysis was carried out using a CE instruments, EA1110 elemental analyzer. UV-vis absorption spectra were measured at room temperature by using a Varian Cary 50 UV-vis spectrophotometer. Photoluminescence, Absolute quantum yield and Time-resolved fluorescence lifetime were obtained using a Photon Technologies International (PTI) Quanta master spectrophotometer equipped with an integrating sphere and a laser excitation system. The relative fluorescence quantum yield was measured using Rhodamine B in Ethanol as a standard reference (1×10^{-7} M, $\Phi_F = 95\%$). Absorption and emission inside the sphere were determined by comparison to a blank sample (glass only). A neutral density filter was used to allow for maximization of the emission signal without saturating the photomultiplier tube detector with excitation light. Each sample type was run in quadruplicate with each quantum yield measurement coming from a freshly drop cast sample. Measurements proved highly repeatable, and errors are given as ±1 standard deviation.

4.3. Results and Discussion

We first examined the solution-state luminescence properties of G1. An aqueous solution of G1 under ambient conditions showed blue fluorescence emission at 460 nm (Figure 4.2) with a quantum yield of 11.5% and a lifetime of 2.18 ns. We did not observe any phosphorescence emission from an aqueous solution of G1 even under oxygen-free conditions. However, when the solution was cooled to 77 K, strong green phosphorescence emission at 510 nm was detected, with a long lifetime of 5.9 ms (Figure 4.3). The solution was diluted to 10^{-5} M to rule out intermolecular interactions between molecules. At this cryogenic temperature, solvents are frozen, which greatly suppresses the vibrational dissipation of triplets and thus allows phosphorescence emission. A G1-doped PVA film was prepared by simple drop casting from an aqueous solution of G1 with 80% hydrolyzed PVA (denoted PVA80; 1 wt % of G1 in PVA80). PVA is a polyhydroxy polymer and can efficiently form intermolecular H-bonds with various polymers[20] and functionalized small-molecular dopants[21, 22] as well as inter and intramolecular H-bonds with PVA itself at room temperature.[23] These unique characteristics of PVA enabled the use of PVA as a host material for the newly synthesized phosphor, G1.

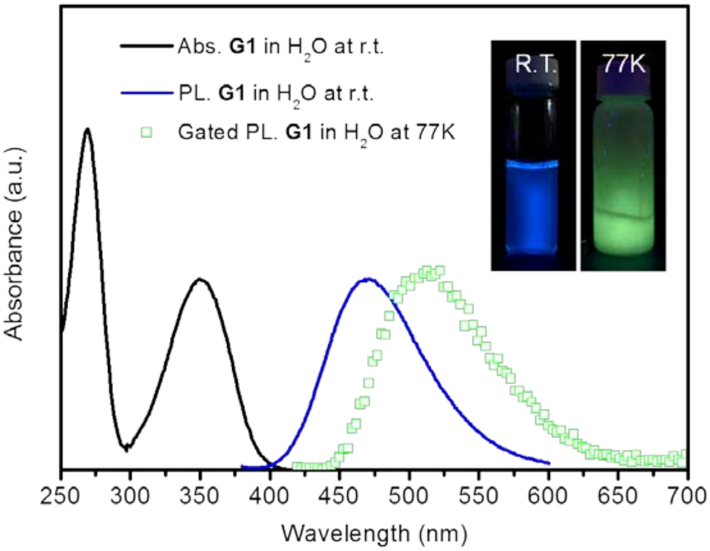

Figure 4.2. UV/Vis absorption (black line), PL (blue line), and gated PL spectra (green squares) of an aqueous solution of G1. The inset shows photoluminescence images of an aqueous solution of G1 at room temperature and at 77 K.

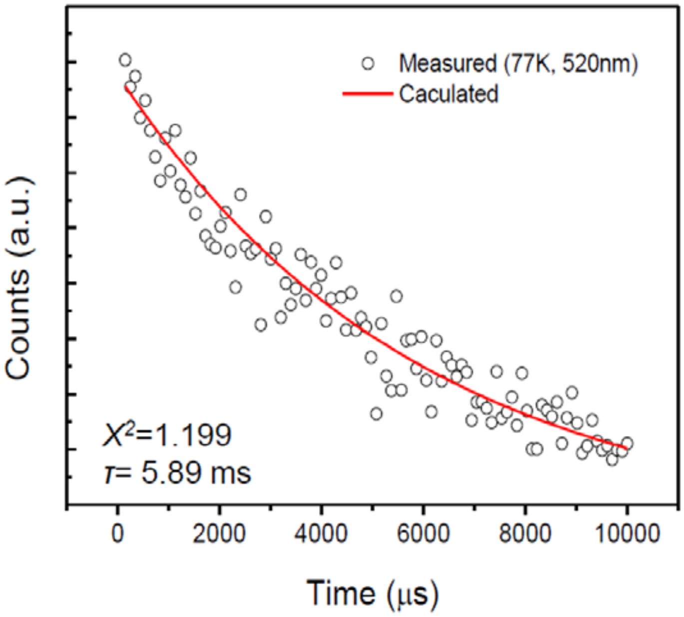

Figure 4.3. Time-resolved measurement of 530 nm emission from **G1** solution (H_2O, 1 × 10^{-5} M) at 77 K with fit to long-lived component. Lifetime and X^2 are indicated.

The resulting thin film showed strong phosphorescence with λ_{max} = 530 nm and only a soft shoulder in the fluorescence region at around 430 nm (Figure 4.4a). The gated photoluminescence (PL) spectrum (Figure 4.4a) and long lifetime of 4.7 ms clearly confirmed that the emission at 530 nm was phosphorescence. Notably, the phosphorescence quantum efficiency reached 13%, which is approximately 1.5 times that of the Br6A–iPMMA thin film. We believe that this large enhancement in phosphorescence quantum efficiency can be attributed to the strong self H bonding of the rigid polymer matrix in combination with the restriction of vibrational motion by the intermolecular H-bonds between PVA80 and G1.

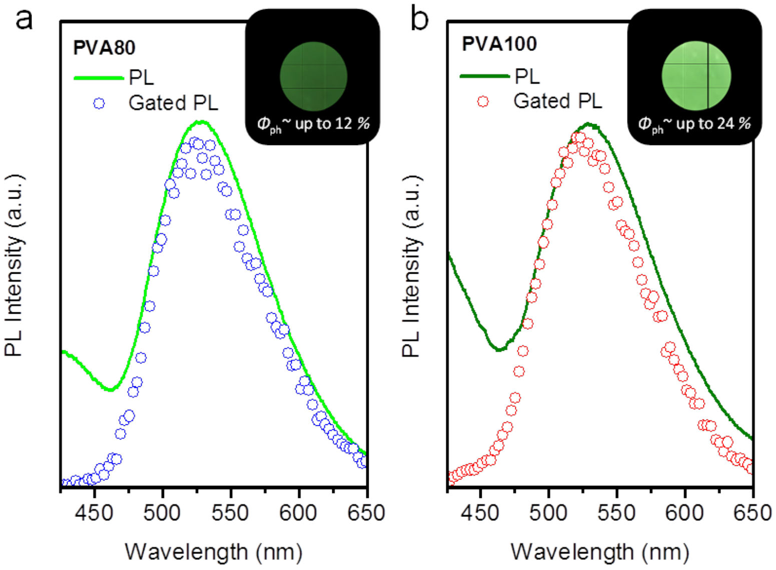

Figure 4.4. PL and gated PL spectra of a) a PVA80 thin film doped with 1 wt % G1 and b) a PVA100 thin film doped with 1 wt % G1. Insets show phosphorescence images of the corresponding G1-doped PVA80 and PVA100 thin films.

We further improved the intermolecular H-bonding efficiency by using 100% hydrolyzed PVA (denoted PVA100). PVA100 has 25% more H-bonding sites than PVA80, which lead to more efficient interpolymer H-bonding and consequentially enhanced rigidity of the PVA matrix. Furthermore, the increased number of H-bonding sites also provides more opportunities for the formation of H-bonds between PVA100 and G1. Thus, PVA100 was expected to suppress rotational and vibrational motion more efficiently than PVA80. Figure 4.4b displays PL and gated PL spectra as well as a photograph of the PVA100 thin film with embedded G1. As expected, the film produced significantly enhanced phosphorescence emission with a quantum yield of up to 24%. This result clearly demonstrates that our intermolecular H-bonding strategy to suppress vibration dissipation is a very effective method to achieve bright organic RTP in the amorphous state. We tested the Br6A–PVA80 system to deconvolute the role of the H-bonding interactions of G1–PVA and PVA–PVA on phosphorescence. Br6A molecules cannot form H-bonds with the PVA matrix because of the absence of a carboxylic acid periphery. In contrast, PVA–PVA H-bonds are retained in the Br6A–PVA system. Br6A–PVA80 thin films (1 wt % Br6A) were fabricated from a solution of PVA80 and Br6A in N,N-dimethylformamide (DMF) by means of solution drop casting. The Br6A-doped PVA80 thin films produced green phosphorescence at room temperature. However, the phosphorescence quantum efficiency was only 2.2%, thus indicating that the H-bonds between G1 and PVA play a critical role in restricting the vibration and movement of G1 in the PVA matrix.

We investigated the effect of the polymer matrix to further prove our hypothesis. We prepared poly(vinyl acetate) (PVAc)/PVA80 blend films with various blend ratios. (Since PVA100 is soluble only in water, but PVAc is not soluble in water, we used PVA80 instead, and dissolved PVA80 with PVAc in DMF.) Each polymer blend was dissolved with G1 and used to make thin-layer PVAc/PVA80 films with embedded G1. The phosphorescence quantum yield of G1 deceased from 13 to 0.5% as the weight percent of PVAc increased from 0 to 100% (Figure 4.5). Unlike the hydroxyl functional group of PVA, the acetyl moiety of PVAc is a weak H-bonding acceptor. Although PVAc can form H-bonds with PVA and G1, the H-bonding strength is weaker than that possible with PVA. Moreover, PVAc cannot form H-bonds with itself because it does not have a H-bond-donor group. Thus, an increase in PVAc content leads to a drop in both the strength and number of H-bonds between matrix polymers as well as between polymers and G1, which results in significant activation of vibrational dissipation and consequent phosphorescence quenching.

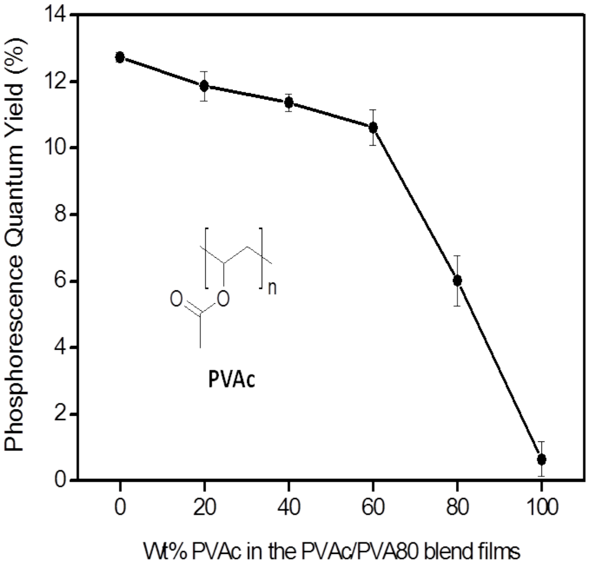

Figure 4.5. Phosphorescence quantum yield of G1 in PVAc/PVA80 blend films with various blend ratios. The chemical structure of PVAc is also shown.

Figure 4.6 shows the effect of the doping concentration of G1. An optimum G1 concentration was identified to be 1 wt % relative to the polymer mass. At a higher concentration than 1 wt %, self-quenching caused the observed low emission yield.[12, 19] At a very low concentration, the number of G1 molecules is too small to enable the necessary halogen bonding between G1 molecules for efficient spin–orbit coupling, thus resulting in the observed minimal phosphorescence quantum efficiency. This hypothesis could be proved by additionally doping the G1–PVA80 system with G2, a dibromo analogue of G1. (Unlike G1, G2 is not soluble in water. Thus, we used PVA80 as the polymer matrix and DMF as the solvent). G2 does not produce RTP even in the PVA matrix by itself, because G2 lacks the triplet-generating benzaldehyde structure. However, it can readily form strong halogen bonds with G1, which significantly enhances spin–orbit coupling and suppresses the vibration of G1. Figure 4.6b clearly shows the effect of the co-dopant on the phosphorescence quantum yield. When the 0.01 and 0.1 wt % G1–PVA80 system was co-doped with an additional 0.1 and 1 wt % of G2, the phosphorescence quantum yield increased from 0.5 and 2% to 2 and 9%, respectively.

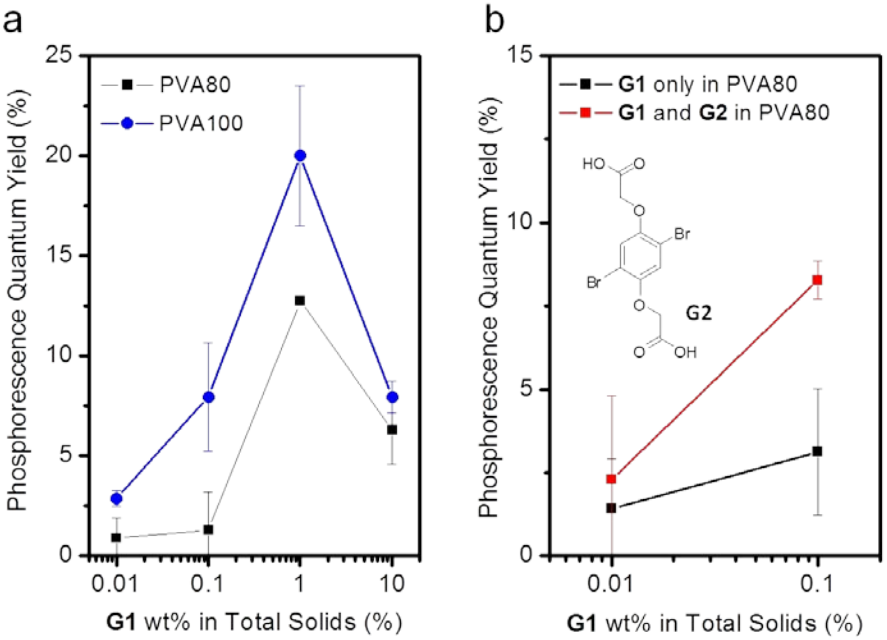

Figure 4.6. a) Phosphorescence quantum yield at different phosphor concentrations for G1-doped PVA80 and PVA100. b) Phosphorescence quantum yield of G1-doped PVA80 and G1/G2-doped (1:10, w/w) PVA80. The chemical structure of G2 is also shown.

The intensity of phosphorescence emission of the G1–PVA system was strongly dependent on the air humidity (Figure 4.7a). As the humidity increased, the phosphorescence intensity decreased linearly (Figure 4.7b), whereas the fluorescence emission peak at 437 nm remained unchanged. We can deduce that at higher humidity, more water is absorbed by the G1–PVA system, and that the absorbed water can efficiently break the H-bonds between PVA molecules and between G1 and PVA. Breaking of the H-bonds consequently enhances the motion of PVA and vibrational motion of G1, thus resulting in the significant decrease observed in the phosphorescence quantum efficiency. In contrast, the fluorescence intensity is not dependent on humidity because the radiative decay rate of singlet exciton is much faster than that of triplet exciton. Interestingly, the phosphorescence of G1–PVA was readily converted into blue fluorescence when water was dropped onto the G1–PVA film.

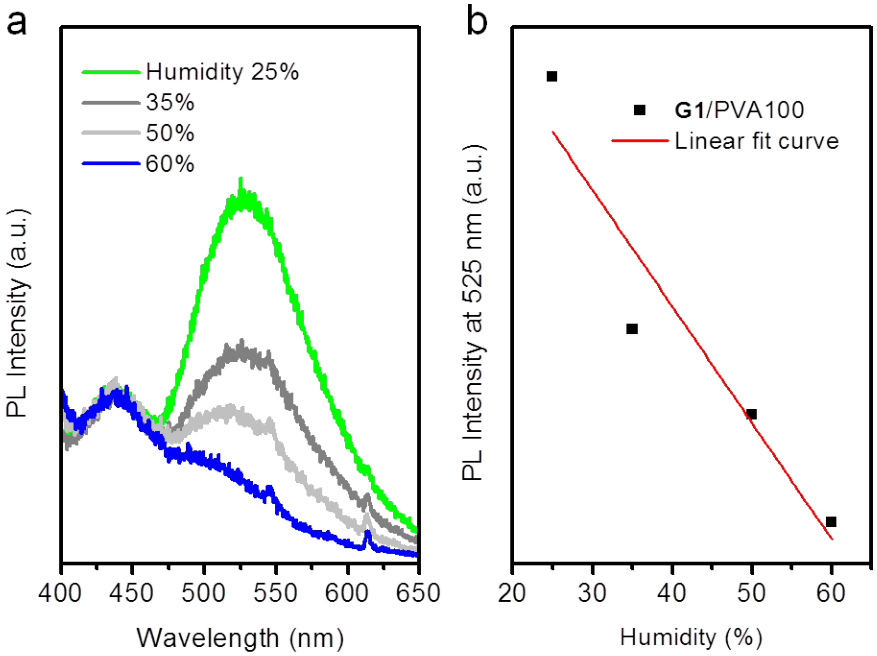

Figure 4.7. a) PL spectra of 1 wt% G1–PVA100 thin film at various humidities. b) Correlation of the PL intensity at 525 nm versus humidity. The black line is the linear fitting curve. The excitation wavelength was 365 nm.

On the basis of this behavior, we successfully demonstrated the use of our material as an "optical recording medium": The characters "UM" were written on the surface of the G1–PVA film (10 wt % G1/100% hydrolyzed PVA) with a water-soaked pen (Figure 4.8a). Unlike the response to humidity, water not only breaks the PVA–PVA and PVA–G1 H-bonds, but also breaks the halogen bonds between phosphors and thus finally dissolves the matrix and phosphors. The dissolved phosphors now emit strong fluorescence, not phosphorescence (Figure 4.8b). This unique system can be utilized as a ratiometric water sensor. We demonstrated several real applications, such as a water indicator for fuel or organic solvents (Figure 4.9) and residual-water monitoring in root-canal treatment in dentistry (Figure 4.10).

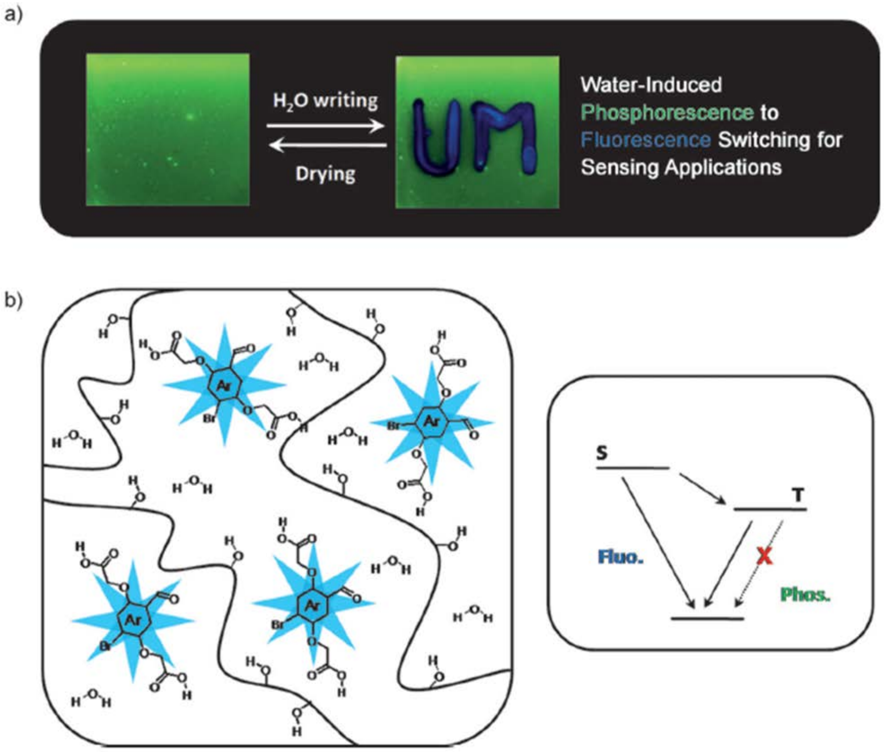

Figure 4.8. a) Reversible direct writing of a fluorescent watermark on a PVA film embedded with G1. The characters “UM” were written with a water-soaked pen. b) Schematic illustration of phosphorescence processes in the G1–PVA composite.

Our phosphorescence system can be also used as a water indicator to in fuel or organic solvents. It is well known that fuel injector inside the automobile engine is easily damaged by presence of water. We investigated the correlation between the ‘phosphorescence to fluorescence’ switching time of G1-PVA100 thin films (10 wt % G1) and the water content in commercial gasoline. As the amount of water in gasoline increases, the response time decreases linearly as shown in Figure 4.9, allowing quantitative analysis. Because the prepared G1-PVA100 thin films respond not to other organic solvents but to only water they can be used as a water indicator in organic solvents as well.

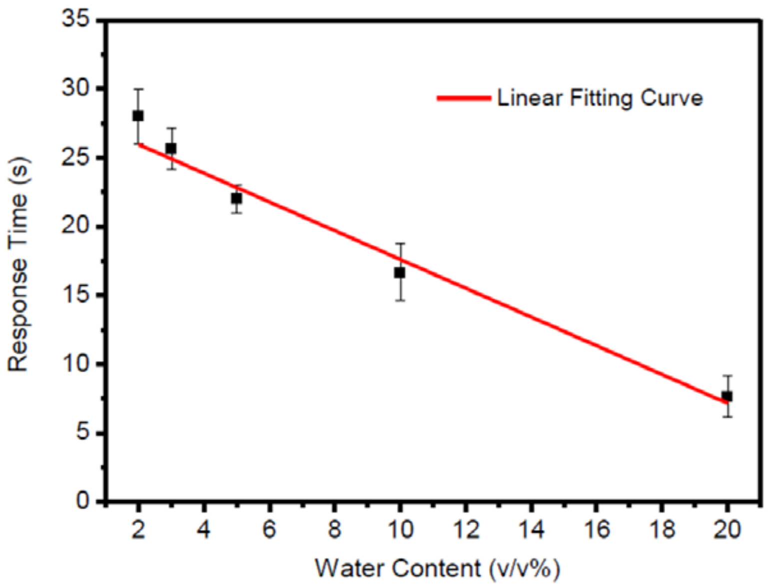

Figure 4.9. Correlation curve of water content in gasoline versus response time for water-in-fuel sensing application.

Residual water monitoring is an important procedure during root canal treatment in dentistry and thus a simple water sensing kit would provide great convenience. We constructed phosphorescence hydrogel prepared by UV-polymerization of an aqueous solution of G1-PVA80 (10 wt % G1 relative to PVA80), polyethylene glycol diacrylate (PEGDA), and 2-hydroxy-2-methylpropiophenone (HMPP) (Figure 4.10a). In this formulation, PEGDA was used as a monomer and HMPP was employed as a photoinitiator for making hydrogel with PVA80. Pristine hydrogel bearing water emitted strong blue fluorescence. However, once the gel was dried completely it showed green phosphorescence (Figure 4.0b). The hydrogel was readily swollen by small amount of water and subsequently changed the emission color from green phosphorescence to blue fluorescence.

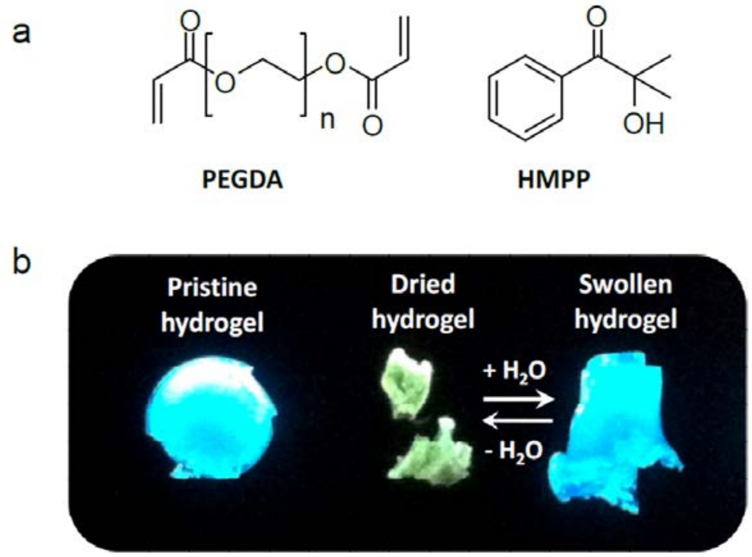

Figure 4.10. (a) Chemical structures of PEGDA and HMPP (b) Photoluminescence images of **G1**-PVA80 embedded hydrogel.

4.4. Conclusions

In summary, we successfully developed a highly efficient purely organic RTP system with an amorphous polymer matrix by introducing rationally designed strong intermolecular interactions. Through systematic investigation, we demonstrated that strong non-covalent interactions, that is, hydrogen and halogen bonds, between the newly designed organic phosphor (G1) and the PVA matrix efficiently suppress the vibrational dissipation of triplet electrons and thus allow a high phosphorescence quantum yield of 24%. We also discovered a unique phosphorescence-to-fluorescence switching phenomenon in the G1–PVA system in response to water. Because, RTP is emitted from a molecular assembly in the G1–PVA system, when water molecules break up the molecular assembly of G1–PVA, the efficiency of spin–orbit coupling drops, thus resulting in fluorescence rather than phosphorescence emission. We believe that the demonstrated strategy based on intermolecular interaction to enable bright RTP from a purely organic material can be utilized for the development of novel phosphors for ratiometric water sensing as well as phosphorescent organic light-emitting diodes for real applications.

4.5. References

1. Sivasubramaniam, V.; Brodkorb, F.; Hanning, S.; Loebl, H. P.; van Elsbergen, V.; Boerner, H.; Scherf, U.; Kreyenschmidt, M. *J. Fluorine Chem*. **2009**, *130*, 640-649.
2. Kearns, D. R.; Case, W. A. *J. Am. Chem. Soc*. **1966**, *88*, 5087-5097.
3. Clark, W. D. K.; Litt, A. D.; Steel, C. *J. Am. Chem. Soc*. **1969**, *91*, 5413-5415.
4. Xu, J.; Takai, A.; Kobayashi, Y.; Takeuchi, M. *Chem. Commun*. **2013**, *49*, 8447-8449.
5. Schulman, E. M.; Walling, C. *Science* **1972**, *178*, 53-54.
6. Love, L. J. C.; Skrilec, M.; Habarta, J. G. *Anal. Chem*. **1980**, *52*, 754-759.
7. Mitchell, C. A.; Gurney, R. W.; Jang, S. H.; Kahr, B. *J. Am. Chem. Soc*. **1998**, *120*, 9726-9727.
8. Dewhirst, M.W.; Fraser, C. L. *Nat. Mater*. **2009**, *8*, 747-751.
9. Turro, N. J. *Modern Molecular Photochemistry*, University Science Books, Sausalito, **1991**, pp. 99-100.
10. Kçhler, A.; Wilson, J. S.; Friend, R. H. *Adv. Mater*. **2002**, *14*, 701-707.
11. Yuan, W. Z.; Shen, X. Y.; Zhao, H.; Lam, J. W. Y.; Tang, L.; Lu, P.; Wang, C.; Liu, Y.; Wang, Z.; Zheng, Q.; Sun, J. Z.; Ma, Y.; Tang, B. Z. *J. Phys. Chem. C* **2010**, *114*, 6090-6099.
12. Bolton, O.; Lee, K.; Kim, H. J.; Lin, K. Y.; Kim, J. *Nat. Chem*. **2011**, *3*, 205-210.
13. Gong, Y.; Tan, Y.; Li, H.; Zhang, Y.; Yuan, W.; Zhang, Y.; Sun, J.; Tang, B. Z. *Sci. China Chem*. **2013**, *56*, 1183-1186.

14. Bergamini, G.; Fermi, A.; Botta, C.; Giovanella, U.; Di Motta, S.; Negri, F.; Peresutti, R.; Gingras, M.; Ceroni, P. *J. Mater. Chem. C* **2013**, *1*, 2717-2724.
15. Gao, H. Y.; Zhao, X. R.; Wang, H.; Pang, X.; Jin, W. J. *Cryst. Growth Des*. **2012**, *12*, 4377-4387.
16. Horie, K.; Mita, I. *Chem. Phys. Lett*. **1982**, *93*, 61-65.
17. Horie, K.; Morishita, K.; Mita, I. *Macromolecules* **1984**, *17*, 1746-1750.
18. Hirata, S.; Totani, K.; Zhang, J.; Yamashita, T.; Kaji, H.; Marder, S. R.; Watanabe, T.; Adachi, C. *Adv. Funct. Mater*. **2013**, *23*, 3386-3397.
19. Lee, D.; Bolton, O.; Kim, B. C.; Youk, J. H.; Takayama, S.; Kim, J. *J. Am. Chem. Soc*. **2013**, *135*, 6325-6329.
20. Khutoryanskiy, V. V.; Staikos, G. *Hydrogen-Bonded Interpolymer Complexes: Formation, Structure and Application*, World Scientific, Singapore, **2009**.
21. Nakanishi, S.; Miyawaki, Y.; Nishikawa, M.; Amano, M.; Fujiwara, S.; Jitou, M.; Itoh, H.; Kawase, M. *J. Chem. Phys*. **1994**, *100*, 3442-3445.
22. Sreeja, S.; Sreedhanya, S.; Smijesh, N.; Philip, R.; Muneera, C. I. *J. Mater. Chem. C* **2013**, *1*, 3851-3861.
23. Bhajantri, R. F.; Ravindrachary, V.; Harisha, A.; Crasta, V.; Nayak, S. P.; Poojary, B. *Polymer* **2006**, *47*, 3591-3598.

CHAPTER 5

A Novel Optical Ozone Sensor Based on Purely Organic Phosphor

This chapter describes an optical ozone sensor based on organic phosphorescence. As an environmentally clean oxidant or disinfectant, ozone has been widely used in the sterilization and deodorization of drinking water. Unfortunately, ozone is toxic to humans, but is regularly generated indoors by office machinery. Conventional inorganic ozone sensors detect ozone by monitoring the conductance decrease or resistance increase resulting from inorganic surface oxidation. Thus, they must be accompanied by an integrated heating system in order to reduce the oxidized surface for reversible usage, which makes this inorganic sensor expensive. Even though optical ozone sensors, based on UV or IR absorption and chemiluminescence or photoluminescence, have attracted interest, they still have practical limitations such as slow response times, low sensitivity, and lack of portability. On the other hand, our novel phosphorescence-based ozone sensor has numerous advantages such as high sensitivity (~ 1ppm), low cost fabrication, and by integration with polymer film it can be disposable and portable like litmus paper sensors.

Parts of this chapter appear in: Lee, D.; Jung, J.; Bilby, D.; Kwon, M. S.; Yun, J.; Kim, J. *submitted*.

5.1. Introduction

Ozone sensing has recently attracted great interest because ozone, which is hazardous to humans, is produced by many industrial processes such as surface cleaning of semiconductor devices and biomaterials.[1-3] As an environmentally clean oxidant or disinfectant, ozone is also used in the sterilization and deodorization of drinking water.[4-6] Furthermore, ozone is generated indoors by office machinery such as photocopiers and laser printers. However, long-time exposure to ozone at high concentration can cause health problems like pulmonary edema, so it is of great importance to detect accurate environmental ozone concentration.[7] Ozone has been widely sensed by monitoring conductance changes in metal oxide-based inorganic semiconductor devices which feature high sensitivity, low cost and simple fabrication.[8-10] Among metal oxides, zinc oxide (ZnO) received more attention as a gas sensor due to its high sensitivity, non-toxicity and high chemical stability.[11-13] In order to further enhance the sensitivity of ZnO-based ozone sensors, nanostructure fabrication has been developed.[14-16]

Ozone is by nature a highly unstable and reactive oxidizing species with a much higher oxidation power than that of oxygen. It is difficult to reversibly reduce the oxidized surface of metal oxides, which limits reversible sensing.[17] Therefore, the conventional semiconductor-based sensors require high temperature operation, above 200 °C, so as to reduce the oxidized surface for reversible sensing.[18-20] These conventional metal oxide based sensors are not suitable for low cost fabrication due to their integrated heating systems, and are not portable due to their high operating temperatures and the high power consumption of the heating system. As an alternative to heating, these metal oxides can be reduced by UV light and re-oxidized by ozone exposure, which enables reversible sensing at room temperature.[21] In this case, the conventional thermal reactivation process of the sensing layer is substituted with external UV irradiation. This photoassisted reversible oxidation and reduction mechanism has been further investigated.[22,23] Bender et al. showed that a ZnO ozone sensor was photo-reduced by UV light exposure in vacuum and the conductivity was recovered accordingly.[22] Wang et al. used a 400 nm light-emitting diode to reduce the oxidized surface of an In_2O_3 ozone sensor.[23]

Optical ozone detection has been garnering interest because optical detection is free from electromagnetic noise and compatible with optical fibers for remote sensing.[24-26] Several optical ozone detection methods have been reported including UV absorption photometry[27,28], IR absorption photometry[29], chemiluminescence[30,31], and photoluminescence (fluorescence)[32,33]. UV or IR absorption methods are not suitable for compact and low cost devices, in spite of their relatively accurate and reliable operation. Chemiluminescence and photoluminescence are highly sensitive, but these methods commonly lack reversibility. Amos reported ozone sensing by means of 2-diphenylacetyl-1,3-indandione-1-hydrazone as a fluorophor, but their sensor suffered from rather slow response and mediocre sensitivity.[32] Guoquan et al. utilized fluorescence quenching to detect atmospheric ozone using 2’,7’-dichlorofluorescein, which required precise pH control.[33] Moreover, fluorescence based photometry must be conducted in solution, which is incompatible with a portable and facile sensory platform. Therefore, small-size portable ozone sensors, especially those can be integrated with any kind of mobile devices, are of great interest.

In this contribution, we present our recent development of a rapid, sensitive, cost-effective, and portable sensory system based on organic phosphorescence to detect ozone gas and ozonated water. We synthesized a purely organic phosphor (Br6A) using a previously reported method.[34] In a doped crystal with its analogous host material (Br6), Br6A shows bright green phosphorescence emission with high photoluminescent quantum efficiency. However, it is easily oxidized by ozone exposure resulting in a decreased phosphorescence quantum yield (QY). This phosphorescence drop is induced by oxidation of aldehyde, its triplet generating core moiety. In order to obtain a free-standing sensory film, the phosphor (Br6A) was blended with an amorphous glassy polymer, isotactic poly(methyl methacrylate) (iPMMA).[35] The resulting blend film showed a predictable and quantifiable quantum efficiency change with increased ozone exposure time in the same fashion as the doped Br6A crystal did. The free-standing film is applicable to monitor ozone concentration in the form of gas or solution. To the best of our knowledge, this unique ozone sensor is the first solid state sensor with signal transduction via organic phosphorescence change. As a free-standing, disposable, and colorimetric sensory film like a litmus paper, this would be one of the most convenient platforms as a portable ozone sensor, and the cost effectiveness can compensate for the limited reversibility.

5.2. Experimental Section

5.2.1. Materials

An organic phosphor (Br6A), 2,5-dihexyloxy-4-bromobenzaldehyde, and matrix material (Br6), 2,5-dihextloxy-1,4-dibromobenzene, were synthesized following previously reported synthetic routes.[34] Isotactic PMMA (iPMMA) (Sigma Aldrich, M_w = 120 kg/mol) was used as polymer matrix without further purification. Potassium iodide was purchased from Sigma Aldrich and sodium thiosulfate pentahydrate ($Na_2S_2O_3{\cdot}5H_2O$) was purchased from Acros Organics. They were used without further purification.

5.2.2. Measurement and Characterization

Proton NMR was conducted on a Varian Inova 500 equipped with a Varian indirect detection probe using $CDCl_3$ solvent with chemical shifts identified relative to 0.05 v/v%

tetramethylsilane standard (0.00 ppm). Photoluminescent (PL) emission, excitation, and quantum yield (QY) data were collected using a Photon Technologies International (PTI) Quantamaster system equipped with an integrating sphere. QY was measured using an integrated sphere whose accuracy was verified using a 10 mM Rhodamine 6G/ethanol solution. Samples for QY measurement were prepared by dropping 0.1 g/mL chloroform solutions of the desired compounds, mixed in the weight ratios reported, onto an unmodified glass substrate.

5.2.3. Ozone Sensing

An ozone sensing doped crystal film was prepared by dropcasting 1 wt % of chloroform solution consisting of 10 wt % of Br6A versus Br6 onto a glass substrate followed by drying in vacuum for 24 h. The pristine phosphorescence of the crystalline film had a 50.4% quantum yield before ozone exposure. The film was dipped in an 8 mL of deionized water in a petri dish. An ozone sensing film of amorphous polymer was prepared by dropcasting 1 wt % of chloroform solution consisting of 5 wt % of Br6A versus iPMMA onto a glass substrate. After drying for 15 min at room temperature, it was annealed at 100 ^oC for 10 min. The resulting amorphous film showed a 6.5% quantum yield. Ozone was generated using a UV-Ozone Procleaner (BioForce Nanosciences) with varying irradiation time, resulting in ozonated water with different ozone concentration. The concentration of ozonated water was determined by titration.[36] The ozonated water containing KI and a few drops of an aqueous starch solution showed a yellow color originating from the formation of I_3^- species via the ozone. A 5×10^{-3} M $Na_2S_2O_3$ solution was used for titration. Using a micro pipet, the exact volume of $Na_2S_2O_3$ solution was quantified by monitoring the color change from yellow to colorless. From the amount of$Na_2S_2O_3$ solution, the amount of ozone was determined, and then ozone concentration was defined as a mass fraction versus given amount of water.

5.3. Results and Discussion

As a purely organic phosphor, Br6A is weakly emissive under ambient conditions due to the dominant vibrational loss pathway even though it contains a good triplet generating moiety, the aromatic ketone. However, it emits bright room temperature phosphorescence once it is intermixed with an analogous dibromo compound (Br6), which has a good crystalline character and forms a well-defined doped crystal.[34] In the doped crystal, vibration is efficiently suppressed by halogen bonding and intersystem crossing is also facilitated by the heavy atom effect induced by halogen bonding. These effects make the doped crystal relatively robust under ambient atmosphere, unlike other purely organic alternatives. Br6A is also quite emissive at room temperature if it is embedded into a glassy polymer matrix like isotactic PMMA.[35] In this composite, vibration is suppressed by the rigidity of the matrix polymer, and intersystem crossing is enhanced at a certain mixing concentrations through intermolecular halogen bonding.[35,36] This amorphous phosphorescence system has a number of advantages over crystal-based phosphorescence, such as easy free-standing film formation and no need for stringent crystal growth. Its phosphorescence emission also shows good stability in ambient conditions partly due to the rigidity of polymer, limited oxygen permeability through the polymer matrix, and suppression of the associated phosphorescence quenching pathways.

Interestingly, these two phosphorescence systems are quite sensitive to ozone, a highly active species, and show a predictable emission efficiency drop by varying ozone concentration. First, we prepared doped crystals consisting of 10 wt % of Br6A versus Br6 to detect ozonated water with different ozone concentration. This crystalline sample has a 50.4% initial QY at room temperature. After submerging the sample in deionized water, ozone was generated and adsorbed into the water. The resulting sample was rinsed with deionized water and dried at room temperature, followed by QY measurement. Ozone concentration was determined by a titration method with a $Na_2S_2O_3$ solution using ozonated water containing KI and starch.[37] As shown in Figure 5.1, QY tends to decrease as a function of ozone concentration. QY decreased more rapidly, with a rate of 4.21% per 1 ppm of ozone, at low concentration (below 6 ppm) than at high concentration (0.90% QY decrease per 1 ppm of ozone above 6 ppm). We believe that at the early stage of ozone exposure, most of the adsorbed ozone can easily react with the crystal film surface, leading to fast QY drop. However, at the later stage with higher ozone concentration slow penetration of the adsorbed ozone through the crystal structure combined with the fact that water is a poor solvent for the crystal result in the slower QY drop. As one can clearly see, the QY drop up to the ozone concentration of 6.07 ppm shows a very good linear correlation implying possible quantitative detection of ozone concentrations of 0.1 ppm - the threshold concentration that damages human tissue and respiratory organs.

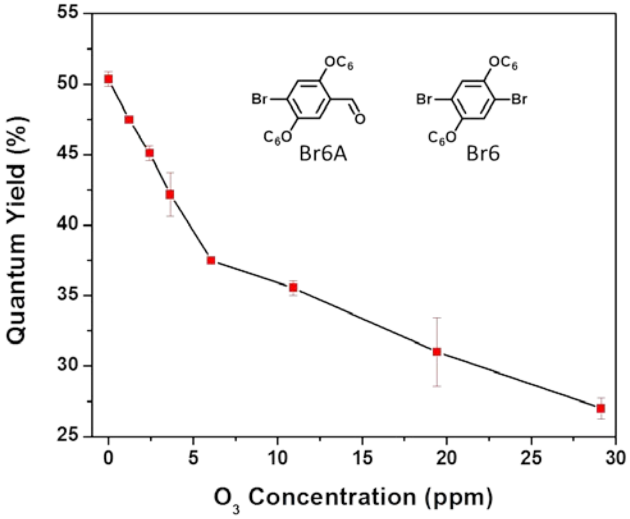

Figure 5.1. Phosphorescence QY change of doped crystal as a function of ozone concentration. Chemical structures of Br6 and Br6A are shown. The excitation wavelength was 365 nm, and the phosphorescence emission was collected in the range of 450 nm to 620 nm.

It has been well-known that aldehyde is easily oxidized to carboxylic acid or peroxy acid by ozone.[38,39] The ozonation mechanism is explained by two competitive pathways. The first one is acyl hydrogen abstraction followed by forming a hydrotrioxide as an intermediate, finally converted to carboxylic acid.[40,41] The other is stepwise cycloaddition leading to a tetroxolane intermediate followed by ring opening of the tetroxolane, finally producing carbonyl oxide.[42] Based on the knowledge from those references, we hypothesized that aldehyde, a critical triplet producing moiety, was oxidized by ozone, resulting in consequential phosphorescence quenching. In order to investigate aldehyde oxidation with ozone, we collected NMR spectra of each sample as shown in Figure 5.2.

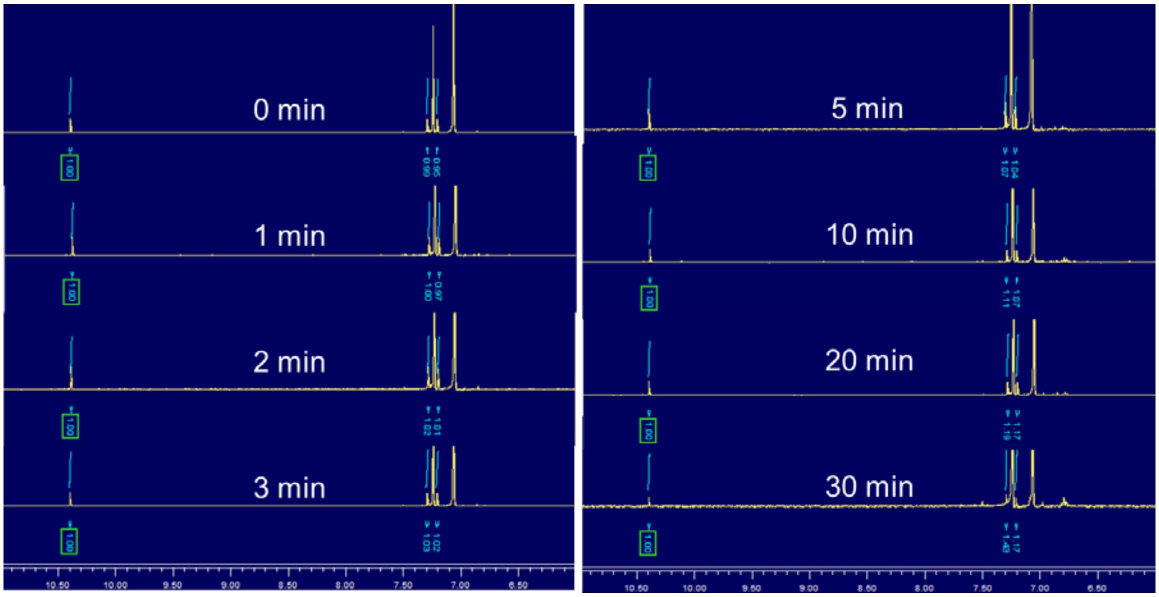

Figure 5.2. ^{1}H NMR spectra of mixed crystal dropcast from Br6 and Br6A solution after exposed in ozonated water for a given time. Each peak was integrated and normalized by aldehyde peak appearing around 10.40 ppm.

Aldehyde and aromatic hydrogen peaks appear at 10.40 ppm, 7.29 ppm, and 7.21 ppm, respectively. Notably, the aldehyde proton peak area decreased relative to that of the aromatic hydrogen. To analyze quantitatively, each peak was integrated and normalized by the aldehyde hydrogen area. The degree of oxidation was defined as

$$(1 - I_{air} / I_{ozone}) * 100 \qquad (1)$$

where I_{air} and I_{ozone} represent relative peak area of the aromatic hydrogen to the aldehyde under air and ozone atmosphere at a given concentration, respectively. Our data clearly show that the degree of oxidation tends to increase with ozone concentration, as shown in Figure 5.3. This increase of oxidation with ozone concentration is closely related with the QY decrease as shown in Figure 5.1. Compared to the later stage above 6 ppm ozone, the aldehyde is more rapidly oxidized at the early stages below 6 ppm, which is likely attributed to the different accessibility of adsorbed ozone to the surface and the inside of the crystal.

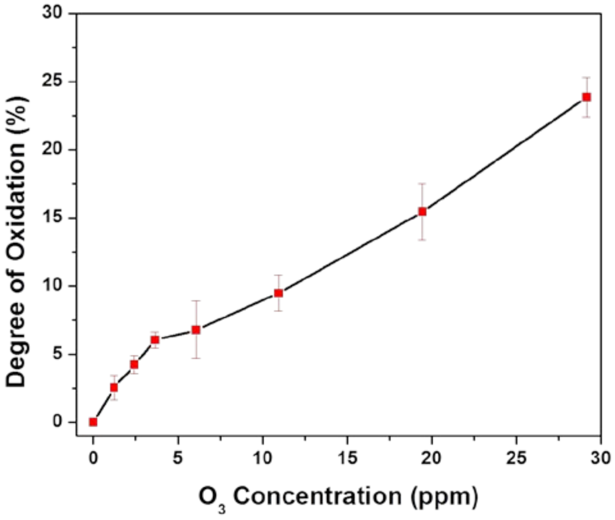

Figure 5.3. Degree of oxidation of the aldehyde moiety in Br6A as a function of ozone concentration based on areal integration of NMR data. Aldehyde and aromatic hydrogen peaks appear at 10.40 ppm, 7.29 ppm, and 7.21 ppm respectively.

In order to investigate morphological change by ozone exposure, we collected fluorescence microscope images as shown in Figure 5.4. The green phosphorescence intensity clearly decreased after the doped crystals were submerged in 6.07 ppm ozonated water while there was no significant change in morphology. This finding implies that QY drop is solely attributed to chemical oxidation of aldehyde, not by physical appearance change.

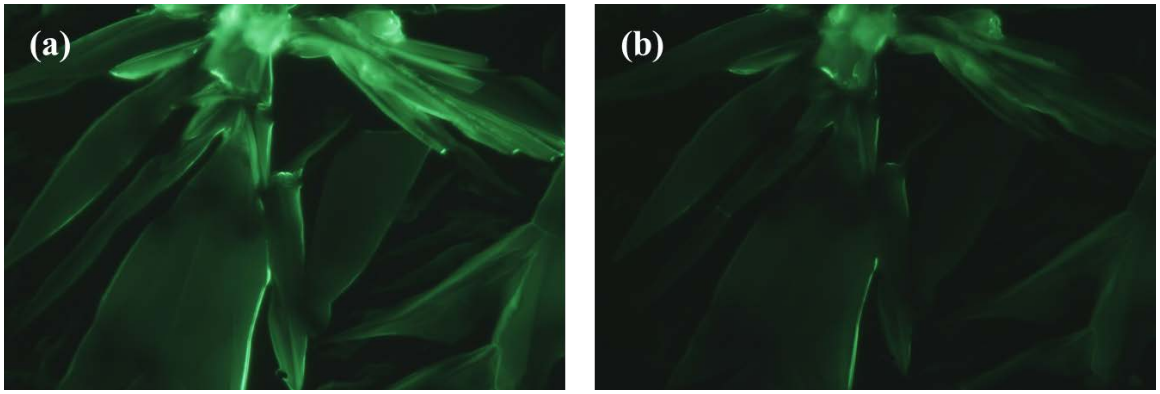

Figure 5.4. Fluorescence microscope images of (a) pristine doped crystal and (b) ozone treated doped crystal in 6.07 ppm ozonated water.

In order to further investigate the oxidation of the aldehyde moiety, we prepared a slowly grown pure Br6A crystal having a phosphorescence QY of 2.9%. Interestingly, we found that Br6A itself was not oxidized (supported by NMR data in Figure 5.5) even after being treated for 30 min in ozonated water and no phosphorescence change was observed. We hypothesized that Br6 in the doped crystal plays a key role in the aldehyde oxidation. It is has been reported that catalytic oxidation of aldehydes, can be promoted by Lewis acids.[43–45] In our system, by acting as a Lewis acid Br6 promotes the oxidation of the Lewis basic, the aldehyde functional group of Br6A. Thus, we concluded that proximity between Br6 and Br6A by intermolecular halogen bonding facilitates Lewis acid catalyzed ozonation of Br6A.

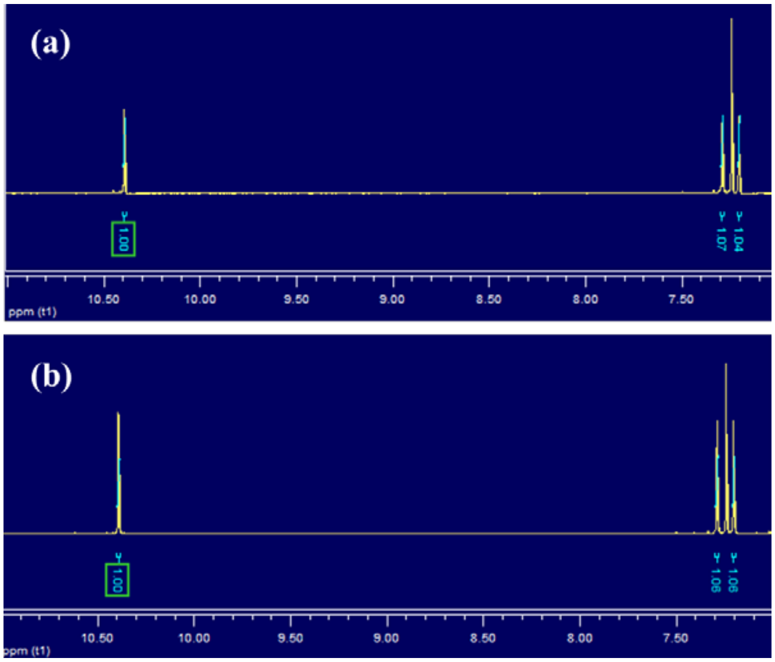

Figure 5.5. 1H NMR spectra of (a) slowly grown Br6A crystal and (b) after being exposed in ozonated water for 30 min. Each peak was integrated and normalized by aldehyde peak appearing around 10.40 ppm.

Even though the crystal-based optical ozone sensor has many advantages, such as rapid response time and high sensitivity, it must be fabricated by dropcasting or spin coating onto a substrate. As a free-standing sensor without any substrate, an amorphous phase optical sensor consisting of a phosphor as a sensory unit embedded in a polymer matrix was developed. Here, PMMA not only acts as a rigid matrix to suppress triplet vibration of Br6A, but it also provides good processability and the propensity to form free-standing phosphorescence films sensitive to ozone. This feature enables the fabrication of a portable and low cost sensor like litmus paper. A 1 wt % chloroform solution containing 5 wt % Br6A to polymer mass was prepared and dropcast on a silicon wafer substrate and dried at room temperature followed by thermal annealing at 100 ^{o}C for 10 min. The resulting film was easily peeled off from the substrate and showed 6.5%

green phosphorescence QY under ambient conditions. It was exposed directly to ozone gas generated by a UV-Ozone Procleaner. As shown in Figure 5.6, the green phosphorescence emission intensity decreases with increasing ozone exposure time and it loses most of its phosphorescence after exposure for 5 min. Data clearly shows a linear correlation between QY and ozone exposure time from the initial state to 3 min ozone exposure. From the proton NMR spectra in Figure 5.7, we found that most of the aldehyde peak disappeared after 5 min ozone exposure.

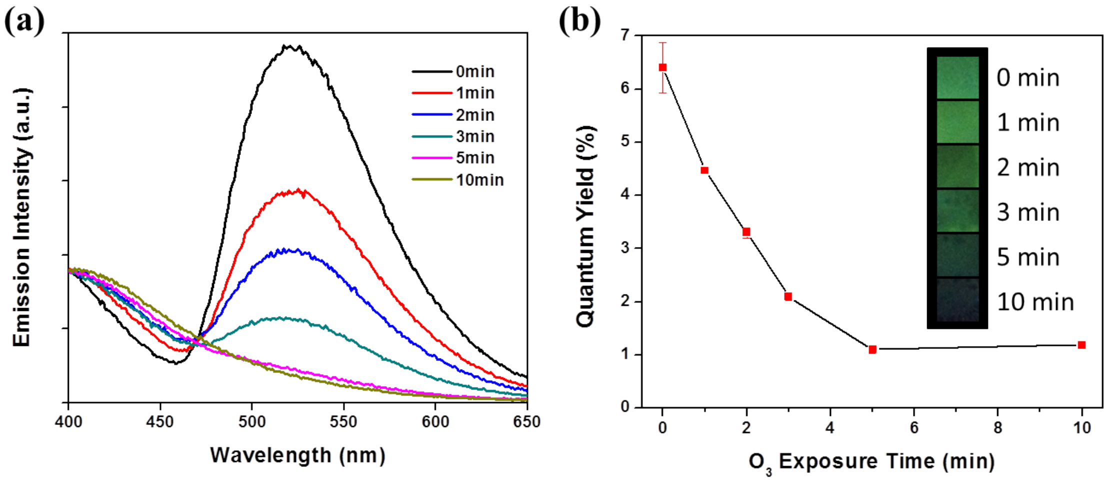

Figure 5.6. (a) Phosphorescence emission intensity change and (b) QY change of amorphous ozone sensor as a function of ozone concentration (inset: fluorescence microscope images were taken under 365 nm light). The excitation wavelength was 365 nm, and phosphorescence emission was collected in the range of 450 nm to 620 nm.

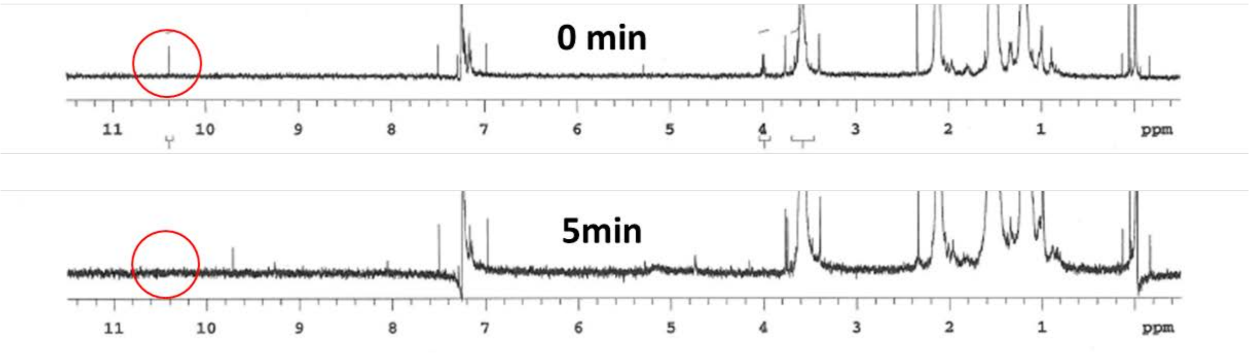

Figure 5.7. ^{1}H NMR spectra of amorphous ozone sensor made from iPMMA and Br6A after exposed in ozone gas for a given time.

5.4. Conclusions

In summary, we developed an optical ozone sensor based on a purely organic phosphor showing high sensitivity and linear correlation between QY and ozone concentration. The observed phosphorescence QY drop is due to oxidation of the aldehyde moiety of the organic phosphor that is the main triplet generating functional group of Br6A. It can quantitatively detect both ozone gas and ozonated water. The sensitivity of the system can detect ozone concentrations of 0.1 ppm that is the threshold concentration harmful to human tissue and respiratory organs. This novel sensor has a number of benefits over conventional conductance-based inorganic sensors including portability, easy fabrication, and low cost. Like a litmus paper, this ozone sensor can be fabricated as a free-standing and disposable film. The development of this sensor technology should enable facile ozone detection, which will help improve the quality of life and safety for workers in ozone producing industries. The low cost of this sensor is suitable for broad adaption as a means of identifying malfunctioning of ozone producing equipment and indicating overexposure to this harmful chemical.

5.5. References

1. John R.; Vig, J. *Vac. Sci. Technol. A* **1985**, *3*, 1027-1034.
2. Linderback, P.; Harmankaya, N.; Askendal, A.; Areva, S.; Lausmaa, J.; Tengvall, P. *Biomaterials* **2010**, *31*, 4795-4801.
3. Aoyagi, Y.; Takeuchi, M.; Yoshida, K.; Kurouchi, M.; Araki, T.; Nanishi, Y.; Sugano, H.; Ahiko, Y.; Nakamura, H. *J of environmental protection* **2012**, *3*, 695-699.
4. Andreozzi, R.; Caprio, V.; Insola, A.; Marotta, R. *Catalysis Today* **1999**, *53*, 51-59.
5. Stucki, S.; Theis, G.; Kotz, R.; Devantay, H.; Christen, H. J. *J. Electrochem. Soc*. **1985**, *132*, 367-371.
6. Glaze, W. H. *Environ. Sci. Technol*. **1987**, *21*, 224-230.
7. Yu, J. H.; Yang, H. J.; Mo, H. S.; Kim, T. S.; Jeong, T. S.; Youn, C. J.; Hong, K. J. *J of electronic materials* **2013**, *42*, 720-725.
8. Xu, Y.; Zhou, X.; Sorensen, O. T. *Sens. Actuators. B*. **2000**, *65*, 2-4.
9. Franke, M.; Koplin, T.; Simon, U. *Small* **2006**, *2*, 36-50.
10. Barsan, N.; Weimar, U. *J. Electroceram*. **2001**, *7*, 143-167.
11. Moseley, P. T. *Meas. Sci. Technol*. **1997**, *8*, 223-237.
12. Takahashi, Y.; Kanamori, M.; Kondoh, A.; Minoura, H.; Ohya, Y. *Jpn. J. Appl. Phys*. **1994**, *33*, 6611-6615.
13. Kwon, T.; Park, S.; Ryu, J.; Choi, H. *Sens. Actuators. B* **1998**, *46*, 75-79.
14. Kenanakis, G.; Vernardou, D.; Koudoumas, E.; Kiriakidis, G.; Katsarakis, N. *Sens. Actuators B* **2007**, *124*, 187-191.
15. Kang, B. S.; Heo, Y. W.; Tien, L. C.; Norton, D. P.; Ren, F.; Gila, B. P.; Pearton, S. J. *Appl. Phys. A* **2005**, *80*, 1029-1032.

16. Cheng, X. L.; Zhao, H.; Huo, L. H.; Gao, S.; Zhao, J. G. *Sens. Actuators B* **2004**, *102*, 248-252.
17. Ando, M. *Trends Anal. Chem*. **2006**, *25*, 937-948.
18. Kim, S.; Hong, H.; Kwon, C. H.; Yun, D. H.; Lee, K.; Sung, Y. K. *Sens. Actuators B* **2000**, *66*, 59-62.
19. Takada, T.; Suzuki, K.; Nakane, M. *Sens. Actuators B* **1993**, *13*, 404-407.
20. Atashbar, M. Z.; Gong, B.; Sun, H. T.; Wlodarski, W.; Lamb, R. *Thin solid films* **1999**, *354*, 222-226.
21. Xirouchaki, C.; Moschovis, K.; Chatzitheodoridis, E.; Kiriakidis, G.; Boye, H.; Morgen, P. *J. Electro. Mat*. **1999**, *28*, 26-34.
22. Bender, M.; Gagaoudakis, E.; Douloufakis, E.; Natsakou, E.; Katsarakis, N.; Cimalla, V.; Kiriakidis, G.; Fortunato, E.; Nunes, P.; Marques, A.; Martins, R. *Thin Solid Films* **2002**, *418*, 45-50.
23. Wang, C. Y.; Cimalla, V.; Kups, T.; Rohlig, C. C.; Stauden, T. Ambacher, O.; Kunzer, M.; Passow, T.; Schirmacher, W.; Pletschen, W.; Kohler, K.; Wagner, J. *Appl. Phys. Lett*. **2007**, *91*, 103509.
24. Ando, M.; Swart, C.; Pringsheim, E.; Mirsky, V. M.; Wolfbeis, O. S. *Solid State Ionics* **2002**, *152-153*, 819-822.
25. Schillinger, E. F. J.; Wright, J. D. *Sens. Actuators B* **2004**, *98*, 262-268.
26. Wolfbeis, O. S. *Anal. Chem*. **2004**, *76*, 3269-3284.
27. Toda, K.; Yoshioka, K.; Ohira, S. *Anal. Chem*. **2003**, *75*, 4050-4056.
28. Ando, M.; Swart, C.; Pringsheim, E.; Mirsky, V. M.; Wolfbeis, O. S. *Sens. Actuators. B* **2005**, *108*, 528-534.

29. El-Sherbiny, M. M.; Ballik, E. A.; Shewchun, J.; Garside, B. K.; Reid, J. *Appl. Opt*. **1979**, *18*, 1198-1203.
30. Takayanagi, T.; Su, X.; Dasgupta, P. K.; Martinelango, K.; Li, G.; Al-Horr, R. S.; Shaw, E. W. *Anal. Chem*. **2003**, *75*, 5916-5925.
31. Hill, E. A.; Nelson, J. K.; Birks, J. W. *Anal. Chem*. **1982**, *54*, 541-546.
32. Amos, D. *Anal. Chem*. **1970**, *42*, 842-844.
33. Guoquan, G.; Qingzhi, Z.; Huaigong, W. *Anal. Chim. Acta* **1994**, *298*, 135-139.
34. Bolton, O.; Lee, K.; Kim, H.-J.; Lin, K. Y.; Kim, J. *Nat. Chem*. **2011**, *3*, 205-210.
35. Lee, D.; Bolton, O.; Kim, B. C.; Youk, J. H.; Takayama, S.; Kim, J. *J. Am. Chem. Soc*. **2013**, *135*, 6325-6329.
36. Kwon, M. S.; Lee, D.; Seo, S.; Jung, J.; Kim, J. *Angew. Chem. Int. Ed*. **2014**, *53*, 11177-11181.
37. Ibanez, J. G.; Mayen-Mondragon, R.; Moran-Moran, M. T.; Alatorre-Ordaz, A.; Mattson, B.; Eskestrand, S. *J. Chem. Educ.* **2005**, *82*, 1546-1548.
38. Dick, C. R.; Hanna, R. F. *J. Org. Chem*. **1964**, *29*, 1218-1220.
39. White, H. M.; Bailey, P. S. *J. Org. Chem*. **1965**, *30*, 3037-3041.
40. Stary, F. E.; Emge, D. E.; Murray, R. W. *J. Am. Chem. Soc*. **1974**, *96*, 5671-5672.
41. Erickson, R. E.; Bakalik, D. Richards, C.; Scanlon, M. *J. Org. Chem*. **1966**, *31*, 461-466.
42. Voukides, A. C.; Konrad, K. M.; Johnson, R. P. *J. Org. Chem*. **2009**, *74*, 2108-2113.
43. Kasprzyk-Hordern, B.; Ziolek, M.; Nawrocki, J. *Appl. Catal. B: Environ.***2003**, *46*, 639-669.
44. Corma, A.; Garcia, H. *Chem. Rev*. **2002**, *102*, 3837-3892
45. Biella, S.; Prati, L.; Rossi, M. *J. Mol. Catal. A: Chemical* **2003**, *197*, 207-212.

CHAPTER 6

The Effects of Extended Conjugation Length of Purely Organic Phosphors on Their Phosphorescence Emission Properties

This chapter describes the effects of the extended conjugation length of organic phosphor on their phosphorescence properties at 77 K. In this work, we focus on the first intersystem crossing, triplet harvesting, which is one of the key processes in realizing phosphorescence emission. A series of bromobenzaldehydes are prepared in order to investigate photophysical properties and computational methods are utilized to calculate intersystem crossing rate and electron density difference between ground states and excited states. Our data clearly shows that phosphorescence intensity decreases with red-shifted emission as the conjugation length increases. Our computational results imply that this correlation is related to intersystem crossing rate determined by spin-orbit coupling strength rather than simple energy difference between the lowest lying singlet and triplet states. TD-DFT calculations show that the $S_1 \rightarrow T_1$ transition more dominantly occurs than $S_1 \rightarrow T_2$ transition for all cases. Moreover, singlet excited states are localized on aldehyde functional group regardless of the conjugation length while triplet excited states are evenly distributed over the conjugated backbone, and therefore, the conjugation length largely affect the intersystem crossing rate.

Parts of this chapter appear in: Lee*, D.; Ma*, X.; Jeong, E. J.; Hashemi, H.; Kieffer, J.; Kim, J. *submitted*. The computational work in the chapter was carried out by Xiao Ma.

6.1. Introduction

Organometallic phosphorescence has attracted much interest for organic light emitting diodes (OLED) application because it offers theoretically 4 times better efficiency than fluorescence counterparts.[1-4] However, organometallic phosphors have some challenges such as identifying new metallic elements and strict ligand design for color tuning. Also, organometallic phosphors for higher energy emission in the blue and near UV regions have poor stability and resulting limited lifetime.[5-6] Purely organic phosphors offer an attractive alternative in terms of synthesis flexibility, good stability, and relatively easier color tuning by controlling band-gap and electron density. However, purely organic phosphorescence has been rarely reported because spin-orbit coupling is not efficiently activated in the absence of a heavy atom, such as a metal, which promotes spin-flipping and phosphorescence emission against dominant vibrational losses.[7-8]

To achieve bright purely organic phosphorescent materials, there are two critical requirements: (i) promoting intersystem crossing (ISC) from excited singlet states to triplet states and (ii) radiative decay via the second ISC event from the triplet states to ground states. Aromatic ketones exhibit efficient spin-orbit coupling at the carbonyl oxygen due to energy proximity between S_1 and T_2.[9] Therefore aromatic ketones are unique moieties in designing organic phosphorescent materials. Even though triplets are generated from aromatic ketones through ISC, they inevitably experience non-radiative decay during the second ISC. More specifically, enhancing spin-orbit coupling is the most important and challenging aspect of creating purely organic phosphorescent materials.

Organic phosphorescence has been mostly observed under cryogenic conditions or for well-confined inorganic crystals where vibrational pathways are minimized.[10-13] Kabe et al. have shown enhanced phosphorescence in dibenzophosphole chalcogenide mixed crystals at low temperature.[14] Room temperature phosphorescence (RTP) from crystals was detected in slowly grown halogenated benzophenone crystals and Boc and N,N′-dicyclohexylurea capped γ-amino acid crystals grown in common organic solvents.[15-16] Bolton et al. designed well-defined phosphorescent crystals by incorporating a directed intermolecular halogen bonding reaching up to 55% efficient quantum yield (QY) in an ambient condition at room temperature.[17] However, these materials are still impractical because the required crystallinity can only be achieved and preserved under limited conditions. Accordingly, achieving phosphorescence in amorphous structures would be desirable, especially in view of practical applications such as OLED, solid-state lighting, and bio imaging. Even though RTP has been observed in amorphous materials in which strong hydrogen bonding is incorporated between phosphors and matrix polymers, the absolute QY was very low (~ 1%) or not even reported.[18-20] More efficient amorphous RTP was reported by Lee et al. by embedding a bromobenzaldehyde derivative in a glassy poly(methyl methacrylate) (PMMA) matrix.[21] They demonstrated that the degree of β-relaxation of PMMA, which depends on the tacticity, strongly affects phosphorescence efficiency of the embedded organic phosphors. The ensuing temperature dependence of this property provides the basis for an optical temperature sensor integrated into microfluidic devices. Recently, more efficient RTP with 24% of QY was achieved by introducing rationally designed hydrogen bonding and halogen bonding with amorphous polymer matrix.[22] Hirata et al. showed that, by acting as an oxygen barrier and by providing mechanical rigidity, β-estradiol as a host material minimizes the nonradiative decay pathways of highly deuterated fluorene derivatives.[23] They realized persistent RTP with a long lifetime (> 1 s) and high QY (> 10%) at ambient conditions. However, thus far, all efforts have been focused on reducing vibrational decay pathways by imparting intermolecular interactions between an organic phosphor and an amorphous host material. Going forward, it is crucial to optimize the structure of phosphors so as to maximize triplet generation.

In organometallic phosphorescence, a few studies were carried out to elucidate the structure-property relationship, mainly for platinum containing phenyl-ethynyl oligomers.[24-25] For example, Rogers et al. investigated the effects of increased conjugation and the influence of the platinum atom on the electronic structure by varying ligand length. However, there is no systematic study about the effect of extended conjugation in purely organic phosphors.

In this contribution, we focus on the first ISC event, triplet harvesting, which is one of the key processes in order to realize bright phosphorescence emission. To investigate the effect of the conjugation length on phosphorescence, a series of bromobenzaldehydes with different conjugation lengths were synthesized, as shown in Figure 6.1. We observed that the phosphorescence intensity decreases as the conjugation length of the organic phosphor is extended, under cryogenic conditions. We concluded that triplet generation via the first ISC is somehow diminished with increasing conjugation length because vibrational decay pathways should be effectively turned off at the liquid nitrogen temperature of 77 K and thereby the second ISC from T_1 to S_0 should be efficient.

This conclusion is also evident based on computational explorations. We first calculated the excited state energy levels of S_1, T_1 and T_2, as well as the spin orbit coupling of $S_1 \rightarrow T_1$ and $S_1 \rightarrow T_2$ transitions. From those results, the rate constant of ISC for each molecule is then determined. It shows that $S_1 \rightarrow T_1$ transition is the dominant process of the first ISC and the rate constant of $S_1 \rightarrow T_1$ decreases as the conjugation length increases, which agrees with the experimental findings. We also identified the distribution of singlets and triplet state locations over each molecule by calculating the total electron density difference between ground state and excited states. The magnitude of ISC rate is strongly correlated to the localization of the singlet and delocalization of the triplet.

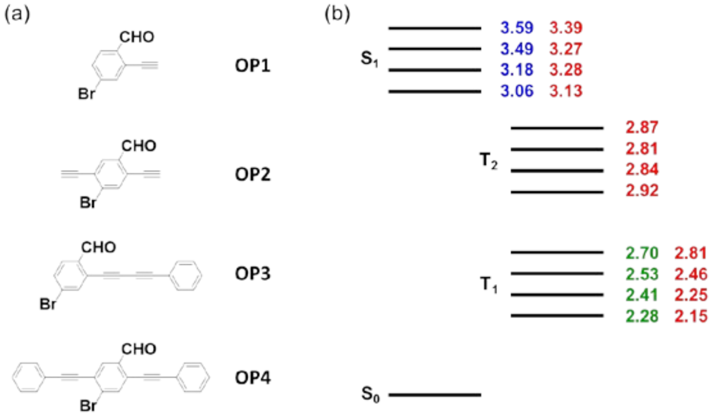

Figure 6.1. (a) Chemical structure of organic phosphors. (b) Excited energy levels relative to the corresponding ground state energy level for OP1 to OP4 in the top-down order; blue: experimental data measured by UV absorption; green: experimental data measured by max. PL emission; red: calculated data by TD-DFT calculation.

6.2. Experimental Section

6.2.1. Synthetic Procedure

We synthesized the series of bromobenzaldehydes as shown in Figure 6.2 to systematically vary the conjugation length of the phosphors and synthetic details are described as follows.

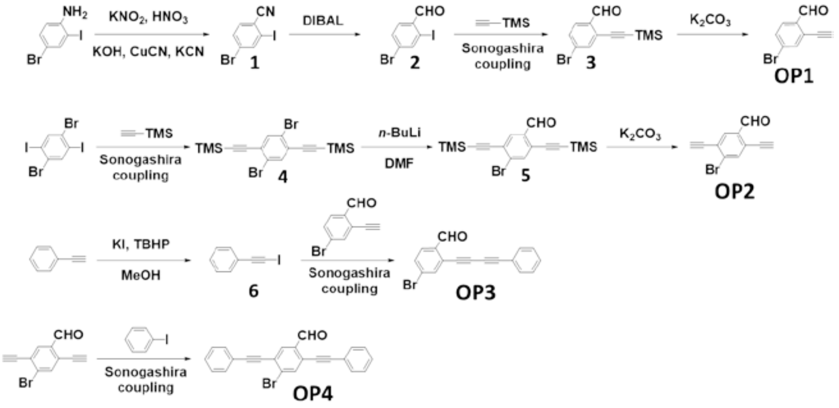

Figure 6.2. Synthetic routes for organic phosphors.

4-bromo-2-iodobenzonitrile (1). A solid mixture of 4-bromo-2-iodoaniline (3 g, 10.07 mmol) and potassium nitrite (0.90 g, 10.57 mmol) was slowly added to a chilled (0 °C) solution of 90% HNO_3 (10 mL) and water (10 mL). The reaction mixture was stirred for 60 min and then poured into ice water (100 mL). The resulting mixture was filtered and then added slowly to a solution of copper cyanide (1.08 g, 12.08 mmol) and potassium cyanide (2.36 g, 36.25 mmol) in water (50 mL) at 70 °C. The reaction mixture was stirred at 70 °C for 30 min under basic conditions while adding 12 M aqueous potassium hydroxide and then cooled to room temperature. The aqueous layer was extracted with ethyl acetate and the organic layer was dried over $MgSO_4$. The product was obtained from column chromatography after evaporating solvent under vacuo (1.55 g, 50%). ^1H NMR (400 MHz, $CDCl_3$): δ 8.11 (s, 1H), 7.60 (d, 1H), 7.43 (d, 1H).

4-bromo-2-iodobenzaldehyde (2). DIBAL (1M in hexane, 14 mL) was added to a solution of **1** (1.55g, 5.03 mmol) in THF (10 mL) at 0 °C. The solution was stirred for 30 min at the same temperature and then warmed to room temperature and stirred overnight. MeOH (2 mL) was added to the mixture to quench the reaction, and the solution was stirred for 30 min. The white precipitate was filtered off and purified by column chromatography (0.40 g, 25%). ^1H NMR (400 MHz, $CDCl_3$): δ 9.98 (s, 1H), 8.15 (s, 1H), 7.72 (d, 1H), 7.60 (d, 1H).

4-bromo-2-((trimethylsilyl)ethynyl)benzaldehyde (3). Bis(triphenylphosphine)palladium(II) dichloride) (25 mg, 0.035 mmol), copper iodide (5 mg, 0.003 mmol), triethylamine (3 mL) and trimethylsilylacetylene (0.12 mL, 0.846 mmol) were added to a solution of **2** (0.22 g, 0.705 mmol) in THF (3 mL) at room temperature. The solution was stirred for 2 h at the same temperature. The resulting mixture was extracted with ethyl acetate and the organic layer was dried over $MgSO_4$. The oily product was obtained from column chromatography after evaporating solvent under vacuo (0.17 g, 86%). ^{1}H NMR (400 MHz, $CDCl_3$): δ 10.47 (s, 1H), 7.75 (m, 2H), 7.57 (d, 1H), 0.30 (s, 9H).

4-bromo-2-ethynylbenzaldehyde (OP1). Potassium carbonate (0.128 g, 0.924 mmol) was added to a solution of **3** (0.13 g, 0.462 mmol) in THF (2 mL) and MeOH (2 mL) at room temperature and stirred for 30 min. The reaction mixture was extracted with ethyl acetate and the organic layer was dried over $MgSO_4$. The brown powder was obtained from column chromatography after evaporating solvent under vacuo (0.087 g, 90%). ^{1}H NMR (400 MHz, $CDCl_3$): δ 10.43 (s, 1H), 7.78 (m, 2H), 7.48 (d, 1H), 3.55 (s, 1H).

((2,5-dibromo-1,4-phenylene)bis(ethyne-2,1-diyl))bis(trimethylsilane) (4). Bis(triphenylphosphine)palladium(II) dichloride) (0.14 g, 0.204 mmol), copper iodide (0.025 g, 0.131 mmol), diisopropylamine (15 mL) and trimethylsilylacetylene (1.2 mL, 8.58 mmol) were added to a solution of 1,4-dibromo-2,5-diiodobenzene (2 g, 4.08 mmol) in THF (15 mL) at room temperature. The solution was stirred for 2 h at the same temperature. The resulting mixture was extracted with ethyl acetate and the organic layer was dried over $MgSO_4$. The oily product was obtained from column chromatography after evaporating solvent under vacuo (1.48 g, 85%). ^{1}H NMR (400 MHz, $CDCl_3$): δ 7.68 (s, 2H), 0.30 (s, 18H).

4-bromo-2,5-bis((trimethylsilyl)ethynyl)benzaldehyde (5). n-BuLi (2.5 M in hexanes, 0.43 mL, 1.08 mmol) was added dropwise to a solution of **4** (0.42 g, 0.98 mmol) in THF (5 mL) at - 78 °C under argon purge. After stirring for 30 min at - 78 °C, anhydrous DMF (0.11 mL, 1.47 mmol) was added slowly and then reaction mixture was allowed to slowly warm to room temperature and stirred for 1 h. The resulting mixture was extracted with ethyl acetate and the organic layer was dried over $MgSO_4$. The oily product was obtained from column chromatography after evaporating solvent under vacuo (0.16 g, 44%). ^1H NMR (400 MHz, $CDCl_3$): δ 10.43 (s, 1H), 7.96 (s, 1H), 7.80 (s, 1H), 0.30 (s, 18H).

4-bromo-2,5-diethynylbenzaldehyde (OP2). Potassium carbonate (0.117 g, 0.848 mmol) was added to a solution of **5** (0.16 g, 0.424 mmol) in THF (2 mL) and MeOH (2 mL) at room temperature and stirred for 30 min. The reaction mixture was extracted with ethyl acetate and the organic layer was dried over $MgSO_4$. The brown powder was obtained from column chromatography after evaporating solvent under vacuo (0.092 g, 93%). ^1H NMR (400 MHz, $CDCl_3$): δ 10.42 (s, 1H), 8.06 (s, 1H), 7.90 (s, 1H), 3.60 (s, 1H), 3.54 (s, 1H).

(Iodoethynyl)benzene (6). Aqueous tert-butyl hydroperoxide (TBHP) (1.21 g, 9.41 mmol) was added dropwise to a solution of phenylacetylene (0.64 g, 6.27 mmol) and potassium iodide (1.14 g, 6.87 mmol) in MeOH (20 mL) at room temperature. The solution was stirred for 2 h at the same temperature followed by adding saturated aqueous sodium thiosulfate to quench the reaction. The resulting mixture was extracted with ethyl acetate and brine, and then the organic layer was dried over Na_2SO_4. The solid product was obtained from column chromatography after evaporating solvent under vacuo (1.01 g, 71%). ^1H NMR (400 MHz, $CDCl_3$): δ 7.52 (d, 2H), 7.42 (m, 3H).

4-bromo-2-(phenylbuta-1,3-diyn-1-yl)benzaldehyde (OP3). Bis(triphenylphosphine)palladium(II) dichloride) (3 mg, 0.004 mmol), copper iodide (1 mg, 0.005 mmol), triethylamine (2 mL) and **6** (0.02 g, 0.087 mmol) were added to a solution of **OP1** (0.016 g, 0.077 mmol) in THF (2 mL) at room temperature. The solution was stirred for 2 h at the same temperature. The resulting mixture was extracted with ethyl acetate and the organic layer was dried over $MgSO_4$. The solid product was obtained from column chromatography after evaporating solvent under vacuo (5 mg, 21%). ^{1}H NMR (400 MHz, $CDCl_3$): δ 10.44 (s, 1H), 7.80 (m, 2H), 7.55 (m, 5H).

4-bromo-2,5-bis(phenylethynyl)benzaldehyde (OP4). Bis(triphenylphosphine)palladium(II) dichloride) (1.5 mg, 0.002 mmol), copper iodide (0.4 mg, 0.002 mmol), diisopropylamine (3 mL) and iodobenzene (0.012 mL, 0.11 mmol) were added to a solution of **OP2** (0.01 g, 0.043 mmol) in toluene (3 mL) at room temperature. The solution was stirred for 2 h at the same temperature. The resulting mixture was extracted with ethyl acetate and the organic layer was dried over $MgSO_4$. The solid product was obtained from column chromatography after evaporating solvent under vacuo (10.4 mg, 63%). ^{1}H NMR (400 MHz, $CDCl_3$): δ 10.52 (s, 1H), 8.10 (s, 1H), 7.92 (s, 1H), 7.58 (m, 4H), 7.40 (m, 6H).

6.2.2. Measurement and Characterization

NMR spectra were obtained from an Inova 400 MHz FT-NMR spectrometer. UV-visible absorption spectra were measured at room temperature by using a Varian Cary 50 Bio UV-Vis spectrophotometer. Photoluminescent excitation and emission spectra at 77 K were collected on a Photon Technologies International (PTI) QuantaMaster equipped with Dewar flask. Time-resolved phosphorescence decay curves were collected with a delay time of 150 μs after excitation of each molecule at 77 K and the phosphorescence lifetime was calculated assuming a single decay mechanism.

6.3. Computational Section

6.3.1. Intersystem Crossing Rate

In phosphorescence, triplet states are populated by a non-radiative transition from a singlet to a triplet $S_k \rightarrow T_n$, i.e. the intersystem crossing. The transition between the different spin states is facilitated by spin orbit coupling. Perturbation theory suggests that for the transition between spin states to occur efficiently the energy difference between the two states must be small.[26] Therefore, based on the energy level diagrams of Figure 6.1, given that injected electrons predominantly create S_1 singlet states, the ISC can occur from S_1 to T_1 or from S_1 to T_2. Several formalisms are given in the literature for estimating the ISC rate. The most simplified form is given as[27],

$$k_{ISC} \propto \frac{\langle S_k | H_{SO} | T_n \rangle^2}{(\Delta E)^2} \qquad (1)$$

where H_{SO} is the spin-orbit operator for calculating the coupling between *k*th singlet S_k and *n*th triplet T_n, and ΔE is the energy difference of the two states. It will give an estimate of the ISC rate for simple comparison. In order to perform a full ISC rate calculation, we will use the Fermi's golden rule expression for radiationless transitions by considering Franck-Condon effect[28],

$$k_{ISC} = \frac{2\pi}{\hbar} \rangle S_k | H_{SO} | T_n \langle^2 [FCWD] \qquad (2)$$

where *FCWD* is the Franck-Condon weighted density of states. There are two main computational methodologies for determining Franck-Condon factor, either by applying displaced-oscillator model[29] or by considering the Duschinsky rotation effect[30]. In this work, we use the displaced-oscillator model to calculate the intersystem crossing rate:

$$k_{ISC} = \frac{\left\langle S_k \middle| H_{SO} \middle| T_n \right\rangle^2}{\hbar^2} \int_{-\infty}^{\infty} dt \exp\left\{ \frac{i\Delta E t}{\hbar} - \sum_j S_j [(2n_j + 1) - n_j e^{-iw_j t} - (n_j + 1) e^{iw_j t}] \right\} \tag{3}$$

where

$$n_j = \frac{1}{e^{\frac{\hbar w_j}{k_B T}} - 1} \tag{4}$$

n_j is the occupation number of jth intramolecular phonon mode with frequency w_j, and S_j is the Huang-Rhys factor measuring the electron-vibration coupling strength. Note that displaced-oscillation model is widely used in transition rate calculation between two states, e.g. simulating charge transfer reactions. Nan et al.[31] and Wang et al.[32] have demonstrated a good agreement between experiments and calculations of charge mobility in organic crystal (e.g. pentacene, rubrene) by including the displaced-oscillation model.

6.3.2. Computation Detail

The excited energy levels, normal mode and electron density of the molecules were calculated using Gaussian09,[33] and visualized the results using GaussView 05 or Multiwfn.[34-35] All calculations were carried out using B3LYP exchange correlation function, and 6-311G* contracted Gaussian basis set with polarization functions. The molecular geometries for both ground and excited states were optimized in the Cartesian coordinate system without any symmetry constraints (maximum degrees of freedom). Following that, a dynamic analysis of the optimized structures was performed to confirm their stability by ascertaining the absence of imaginary frequency modes. Next, the excited energy levels were calculated using a single-point time dependent density functional theory (TD-DFT) calculation based on the ground state geometry. The Huang-Rhys factors corresponding to different normal mode frequencies were obtained using the DUSHIN program developed by Reimers.[36] Finally, The electron density distribution of the ground and excited states were generated based on the optimized structure in that state.

The spin orbit coupling strength between two different excited states were calculated using the Dalton program.[37] The double residue of the quadratic response function was applied when the two states were both excited states, while the single residue of the linear response was applied when one of the two states was ground state.

6.4. Results and Discussion

6.4.1. Photophysical Properties

In the series of bromobenzaldehydes we prepared as described in Figure 6.2, the purpose of incorporating acetylene and benzene moieties is to systematically vary the conjugation length of the molecules. In each case, the π-conjugated parts of ground-state molecular structures optimized using first-principles calculations adopt a planar configuration, which allows us to unequivocally define and compare their conjugation lengths. The CHO functional group lies in the same plane as the conjugated backbone, with the C=O bond pointing away from the triple bond. This is due to the repulsive interaction between the lone pair electrons on oxygen atom and π-electrons in triple bonds. In the OP1 molecule, for example, the local optimal state when making them close to each other raises the energy by 108 meV over the ground state.

Comparing the excited states energy levels obtained from TD-DFT calculations with experimental measurements (Figure 6.1), we observe a good match for both S_1 and T_1

energy levels relative to the respective S_0 levels. We also note that the energy levels for S_1 and T_1 consistently decrease with increasing conjugation length, but for each state keep close to each other within a narrow range. From OP1 to OP4, S_1 only decreases by 0.53 eV in experiments and 0.26 eV in calculations, and T_1 by 0.42 eV in experiments and 0.66 eV in calculations. Hence, we can expect that the optoelectronic properties of these molecules are dominated by the interplay between their conjugation backbones and CHO or Br functional groups, and that the conjugation length plays a subtler role. Conversely, the calculated T_2 energy level for every molecule is lower than its S_1 level and higher than T_1 level, which would favor the intersystem crossing if this process was solely controlled by the singlet-to-triplet energy difference. To complete the assessment, however, we need to account for the spin orbit coupling strength, as discussed below.

Experimental UV absorption spectra are depicted together with extinction coefficients in Figure 6.3. Each solution was diluted to around 10^{-5} M with chloroform to avoid aggregation effects and measured at room temperature. As conjugation length increases, the absorption wavelength is red-shifted from 310 nm for OP1 to 360 nm for OP4 and extinction coefficient increases in S_0-S_1 transition region.

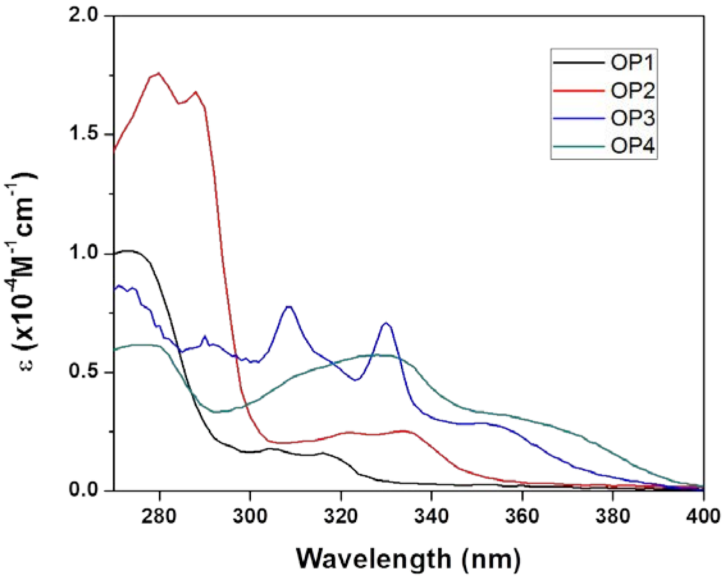

Figure 6.3. UV absorption spectra were measured in chloroform solution at room temperature and plotted with extinction coefficient.

Figure 6.4 shows steady state phosphorescence spectra collected at 77 K and ambient pressure. Each solution was diluted to around 10^{-5} M with chloroform and excited at the maximum excitation wavelength respectively. The emission intensity was calibrated so as to clearly show phosphorescence difference at the same absorbance. The fluorescence emission spectra due to the S_1-S_0 transition were cut off to clearly see phosphorescence emission. As the conjugation length increases, emission is red-shifted from blue for OP1 to pink for OP4. The above trend is consistent with the predictions of electronic states based on TD-DFT calculations as shown in Figure 6.1.

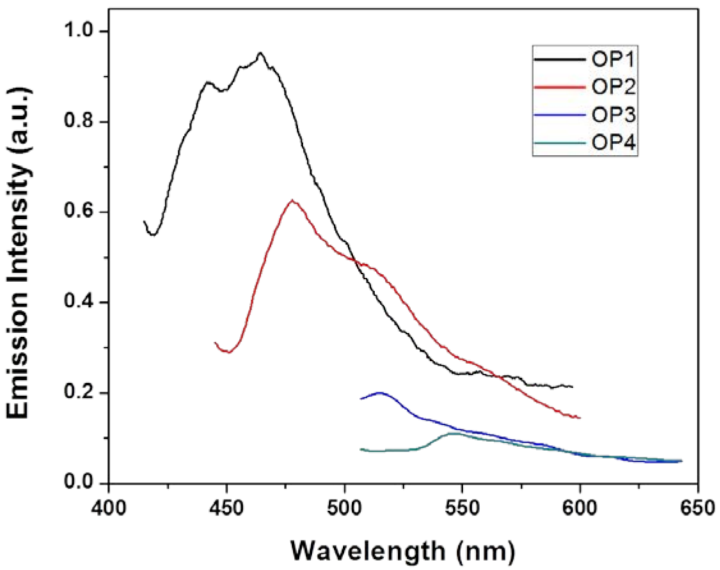

Figure 6.4. Phosphorescence spectra were measured at 77 K with same absorbance. Each molecule was excited at 320, 336, 350, and 360 nm respectively.

At the same time, the phosphorescence intensity dramatically decreases with increasing conjugation length. Since the energetics of the triplet and singlet states for the various molecules do not vary in a commensurate fashion, these intensity differences must be rather due to the conjugation length dependence of first ISC rates. In these measurements, vibrational decay pathways have been effectively eliminated by collecting data at liquid nitrogen temperatures of 77 K. To confirm the existence of phosphorescence, the gated lifetime was measured at 150 μs after excitation of each molecule. Figure 6.5 shows time-resolved phosphorescence decay, including data fitting curves, for long-lived components. Lifetimes were observed in the range from 7.24 to 13.53 ms.

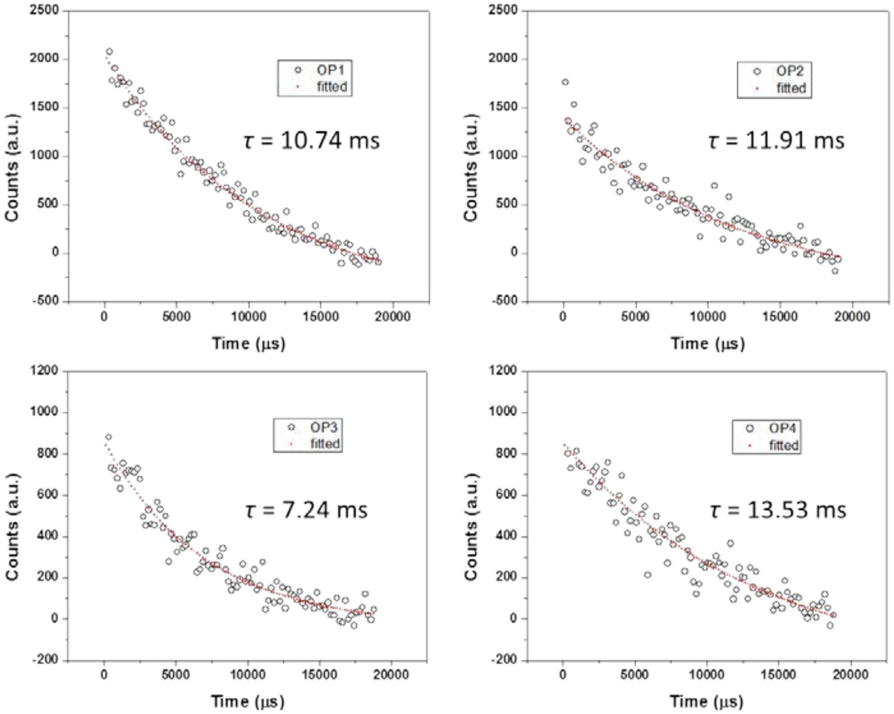

Figure 6.5. Time-resolved phosphorescence decay curve for OP1-OP4 and phosphorescence lifetime obtained from curve-fitting.

6.4.2. Spin Orbit Coupling Matrix Elements and ISC Rate

TD-DFT based methods were used to calculate the ISC rate constants for comparison with experimental findings. In Table 6.1 we show the SOC matrix elements for the $S_1 \rightarrow T_1$ and $S_1 \rightarrow T_2$ transitions. We use x, y, z to represent different polarizations of the spin orbit coupling, which leads to differently polarized light when electrons are quenched from triplet to ground states.[38] As we can see, $S_1 \rightarrow T_1$ coupling is more than an order of magnitude stronger than $S_1 \rightarrow T_2$ coupling, yielding mainly the x- and y-polarized light for the phosphorescence emission.

Table 6.1 SOC matrix elements (10^{-5}*a.u.) for $S_1 \rightarrow T_1$ and $S_1 \rightarrow T_2$ transition in different polarization directions

	$\langle S_1 \vert H_{SO}^{k} \vert T_1 \rangle_{k=x,y,z}$			$\langle S_1 \vert H_{SO}^{k} \vert T_2 \rangle_{k=x,y,z}$		
	x	y	z	x	y	z
OP1	1.6	-8.8	0	0	0	-0.12
OP2	3.1	9.7	0	0	0	0.14
OP3	4.69	-0.665	0	-0.002	0	-0.073
OP4	0	0	-0.006	0	0	0.013

The ISC rate is then calculated using equation (3). To obtain the total rate constant, we add the contributions from all three polarization directions. Figure 6.6a shows the rate constants for $S_1 \rightarrow T_1$ and $S_1 \rightarrow T_2$ transitions plotted versus the type of molecule in the order of increasing conjugation length. We also calculated a dimensionless factor contributing to ISC rate constants according to equation (1), as shown in the Figure 6.6b. First, we observe that the intersystem crossing rate for $S_1 \rightarrow T_1$ is much larger than that for $S_1 \rightarrow T_2$ (Note the different scales for the rates of the two processes). The dominant factor for this behavior is the large discrepancy in SOC between the two transitions, compared to the slight change in the energy difference. This finding strongly suggests that, at least at low temperatures, the phosphorescence efficiency is mostly determined by the $S_1 \rightarrow T_1$ ISC rate. Secondly, our simulation results perfectly parallel the experimentally observed dependence of phosphorescence efficiency on conjugation length, in that the $S_1 \rightarrow T_1$ ISC rate decreases as the conjugation length increases from OP1 to OP4. Hence, the additional insight derived from simulations implies that increasing conjugation compromises the phosphorescence efficiency by slowing down the dominant $S_1 \rightarrow T_1$ ISC process. We also noticed that the $S_1 \rightarrow T_1$ rate of OP3 and OP4 has been much lower than the first three molecules. This could perfectly explain the much weakened emission spectrum of OP3 and OP4, as shown in Figure 6.4. Finally, by comparing the result of the dimensionless factor with the actual ISC rate as shown in Figure 6.6b, we found that the Franck Condon effect is not so influential as the spin-orbit coupling and energy difference in our study, since we obtained the same trend when increasing the conjugation length.

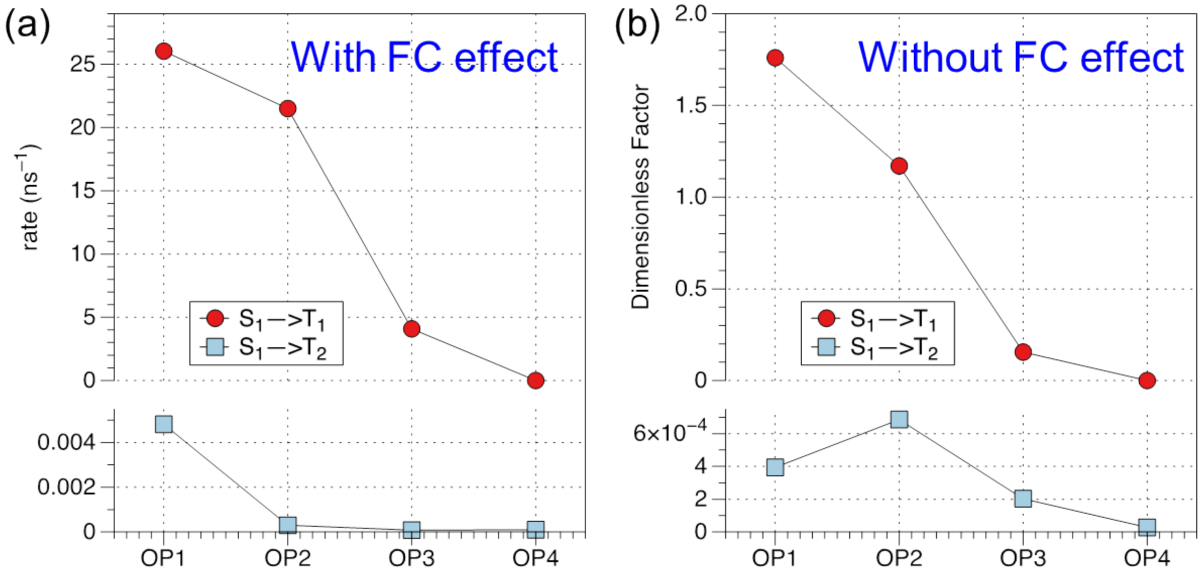

Figure 6.6. (a) The rate constants of intersystem crossing for $S_1 \rightarrow T_1$ and $S_1 \rightarrow T_2$ transitions (Inset) calculated according to equation (3). The value of $S_1 \rightarrow T_1$ for OP4 is 1×10^{-4} ns^{-1}. (b) The dimensionless factor ($*10^{-5}$) contributing to rate constants according to equation (1).

6.4.3. Steric Aspects of ISC

To further investigate the mechanism by which conjugation length affects the ISC process, we calculated the electron densities surrounding the molecular constituents for the ground state and for different excited states of the four molecules under consideration. The electron density of the ground state serves as a reference, and by subtracting it from that of the excited states, we obtain the electron density difference that pinpoints the locations populated by electrons as a direct consequence of the excitation. For this spatially resolved electron density difference to be meaningful, we must ascertain that the geometries of the molecules do not change significantly between the ground and excited states. Indeed, upon optimizing the atomic positions of the molecules in their excited states atoms shift from their ground state positions by less than 0.4Å for all molecules as shown in Figure 6.7.

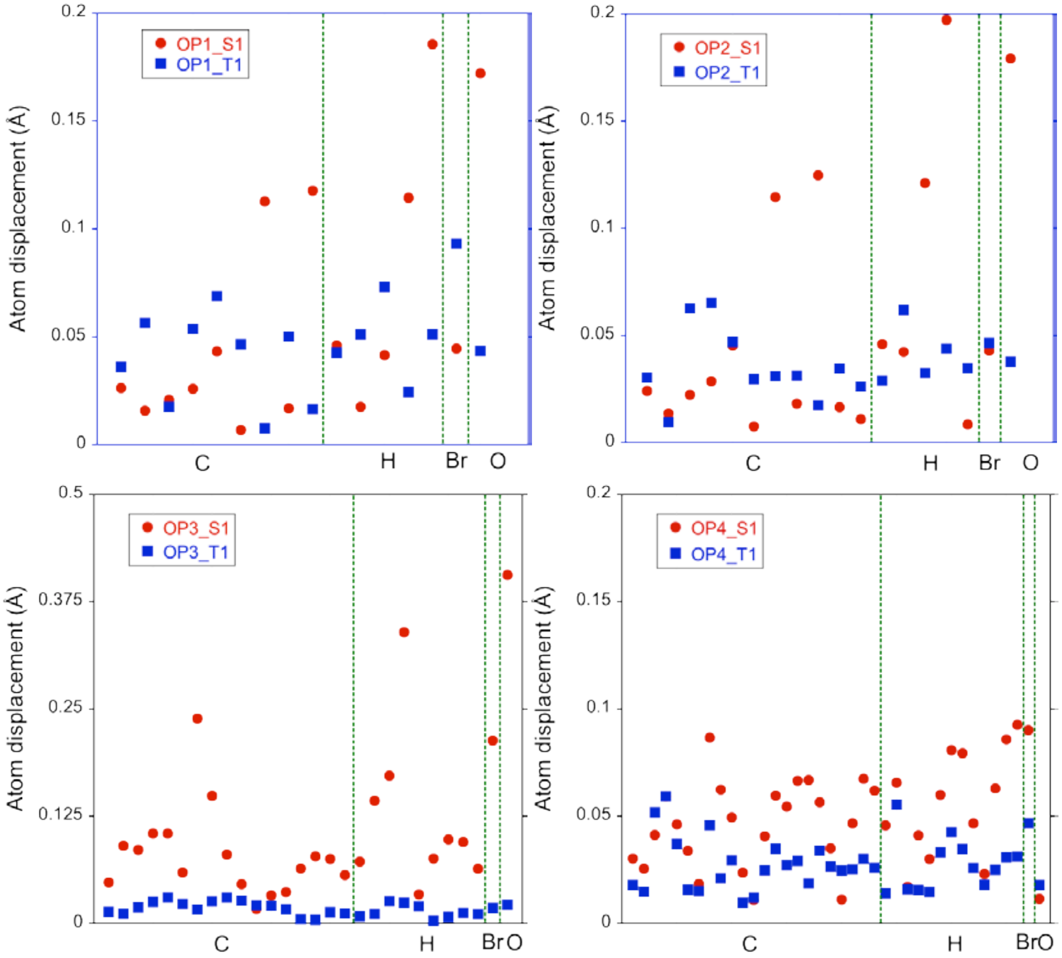

Figure 6.7. The atom displacements of OP1-OP4 between excited states (S_1, T_1) and ground state (S_0). The x-axis is divided into four regions, each containing the same atom type.

Figure 6.8 shows the electron density differences for the $S_0 \rightarrow S_1$ and $S_0 \rightarrow T_1$ transitions. Two different iso-density surfaces are shown to provide a measure for the definition of the charge distribution. The blue color depicts regions with a net gain in electron density upon transition, whereas pink identifies regions that incur an electron density loss. For the $S_0 \rightarrow S_1$ transition at the lower iso-density value, a distinctly large singlet-populated space can be identified around the CHO functional group and to a small extent, singlets are manifest in other region on the conjugation backbone.

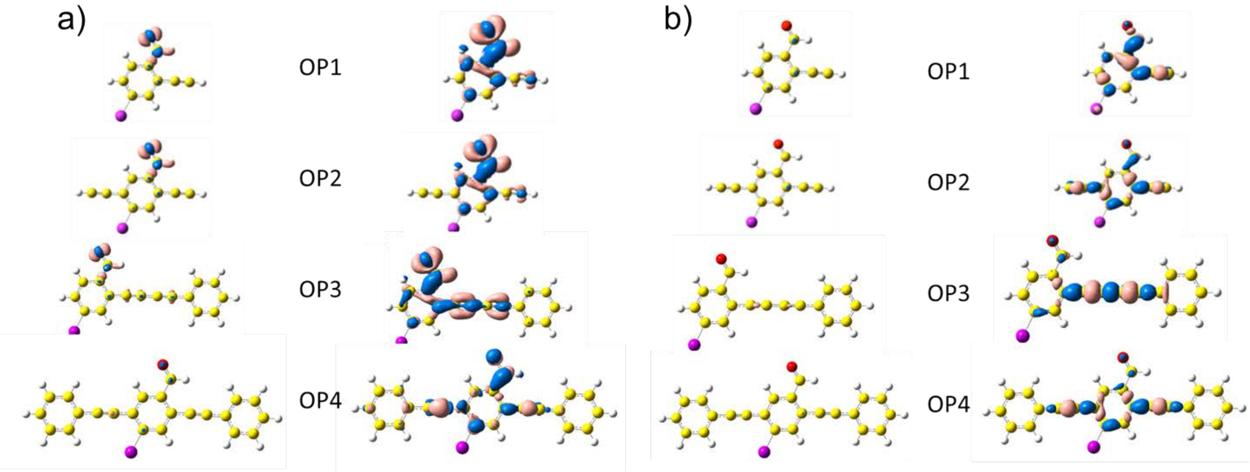

Figure 6.8. Plot of the total electron density difference between ground state and excited states, isovalue is in the unit of electrons/Å^3 (a) $S_0 \rightarrow S_1$, left: isovalue = 0.01, right: isovalue = 0.002 (b) $S_0 \rightarrow T_1$, left: isovalue = 0.01, right: isovalue = 0.002. The pink represents where loses electrons during the transition, and the blue represents where gains the electrons during the transition.

Conversely, at the higher iso-density value, the singlets appear only on the CHO functional group. From this comparison we conclude that the singlet excited states are strongly localized on CHO functional group, and this is consistently the case for all the five molecules. Carrying out the same analysis for the $S_0 \rightarrow T_1$ transition, on the other hand, we find excited electrons evenly distributed over the conjugated backbone, for both low and high iso-density values, which means that the T_1 excited state is delocalized. Importantly, the degree of delocalization is stronger the higher the conjugation length. Delocalization is most pronounced in OP4, where the triplet population is spread over the entire conjugation backbone. Hence, while the singlet states remain localized, independent of conjugation length, triplet states become increasingly delocalized with growing conjugation length. Consequently, for large conjugation lengths orbitals that host electrons excited into triplet states are spatially further removed from those that host electrons in the singlet state, leading to reduced spin orbit coupling strength and thus low ISC rates and low phosphorescence emission efficiency. This finding can explain our experimental results, and indeed, is consistent with observations for other molecular systems reported in the literature.[24]

This work is more extensively studied using different kinds of functional groups such as hexyloxy and acetylene moieties to vary conjugation length of bromobenzaldehyde derivatives (Figure 6.9). Our data implies that extended conjugation causes red-shifted phosphorescence with decreased intensity (Figure 6.10) and it is also attributed to decreased S_1 to T_1 ISC rate (Figure 6.11) calculated by equation (1) and (3) in a same way with previous molecule set. The total electron density difference shows that singlet excited states are localized on aldehyde group while triplet states are delocalized along the conjugated backbone (Figure 6.12). This finding implies that our hypothesis is generally applied regardless of polarity effect from different functional groups such as hexyloxy, acetylene, and benzene ring.

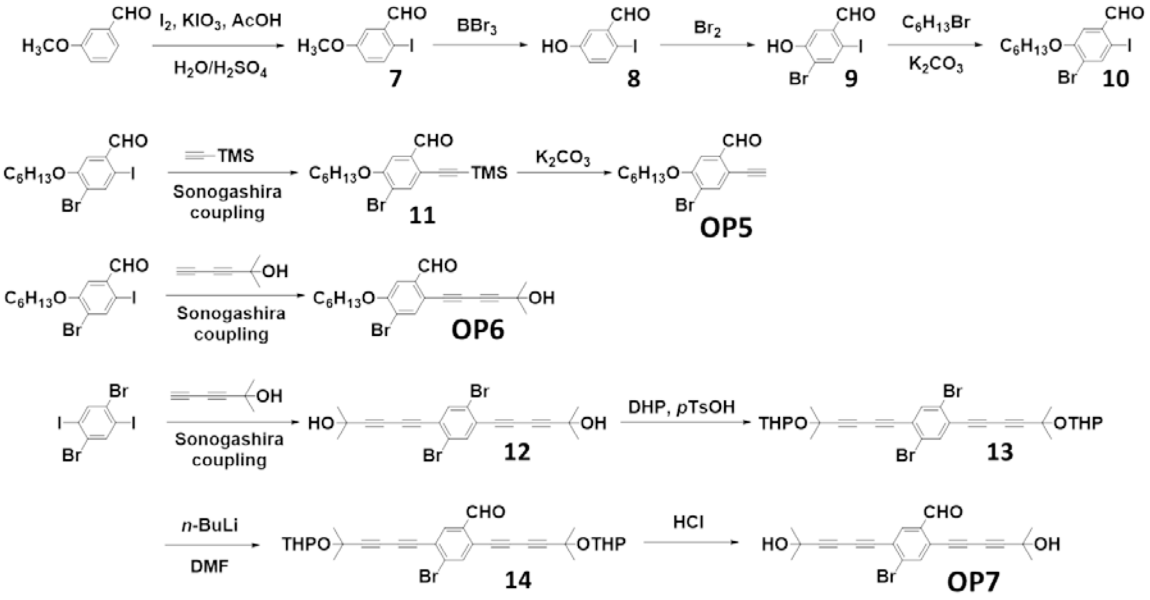

Figure 6.9. Synthetic routes for organic phosphors with different functional groups.

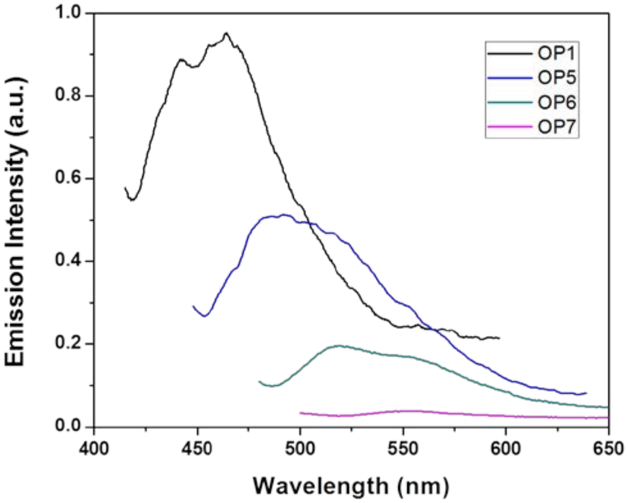

Figure 6.10. Phosphorescence spectra were measured at 77 K with same absorbance. Each molecule was excited at 320, 350, 362, and 360 nm respectively.

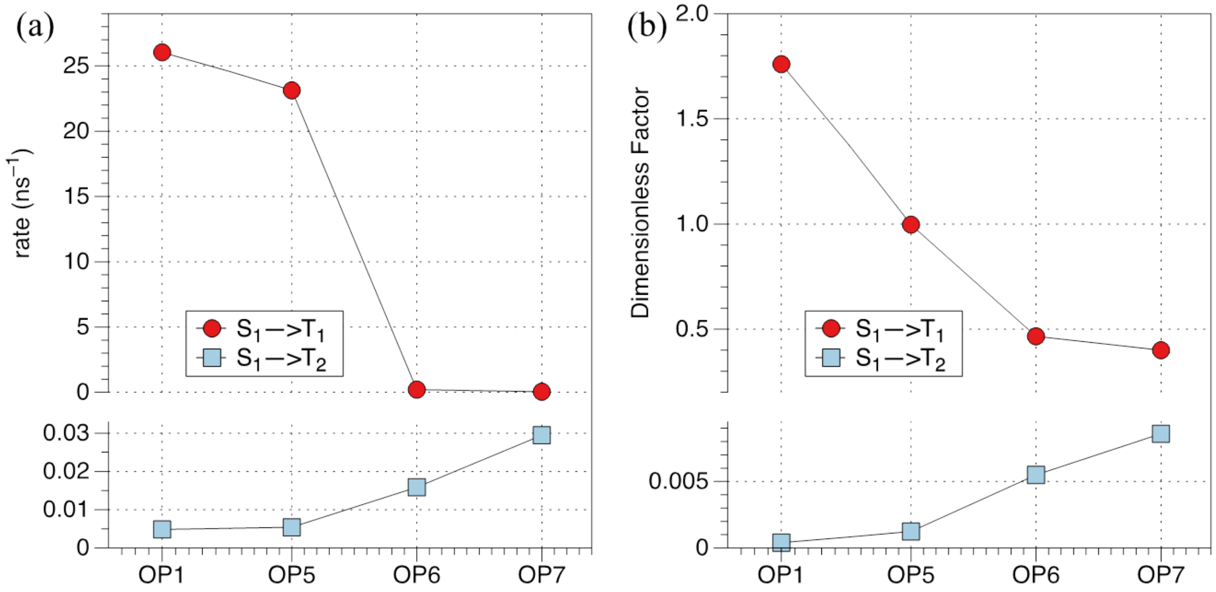

Figure 6.11. (a) The rate constants of intersystem crossing for $S_1 \rightarrow T_1$ and $S_1 \rightarrow T_2$ transitions (Inset) calculated according to equation (3) and (b) the dimensionless factor (*10^{-5}) contributing to rate constants according to equation (1).

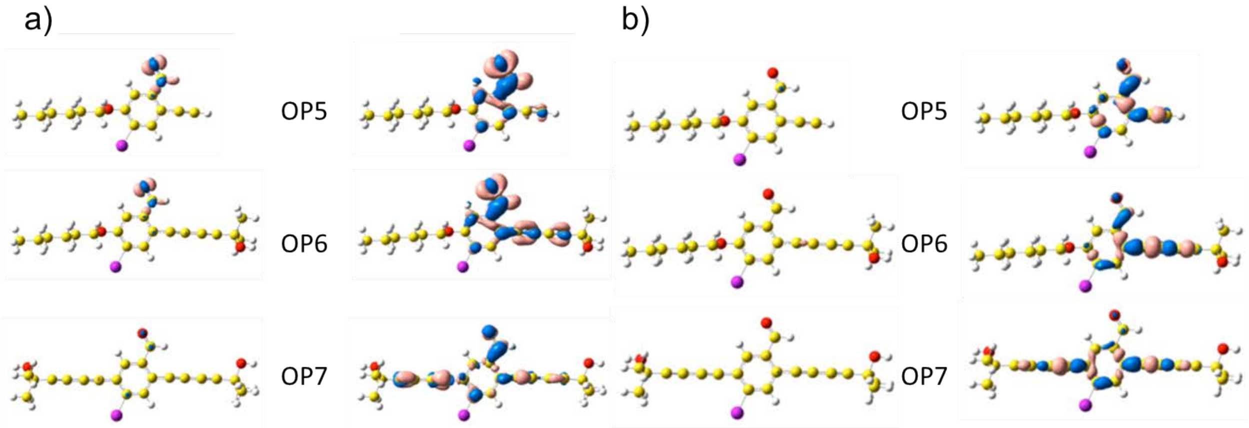

Figure 6.12. Plot of the total electron density difference between ground state and excited states, isovalue is in the unit of electrons/Å^3 (a) $S_0 \rightarrow S_1$, left: isovalue = 0.01, right: isovalue = 0.002 (b) $S_0 \rightarrow T_1$, left: isovalue = 0.01, right: isovalue = 0.002. The pink represents where loses electrons during the transition, and the blue represents where gains the electrons during the transition.

6.5. Conclusions

We synthesized a series of purely organic bromobenzaldehydes for which the conjugation length is systematically varied. We found that the phosphorescence efficiency decreases and the emission color is red-shifted with increasing conjugation length. These observations are interpreted based on results from first-principles electronic structure calculations. The ISC rates are dominated by the SOC strength and not by the energy difference between lowest lying singlet and triplet states. Computations revealed that the $S_1 \rightarrow T_1$ transition rate is the highest for all molecules. Furthermore, while the singlet state remains localized for all molecules, the triplet state becomes progressively more delocalized with increasing conjugation length in the molecule. The ensuing spatial separation between singlet and triplet orbitals in molecules with longer conjugation length reduces the SOC strength and consequently the $S_1 \rightarrow T_1$ ISC rate. In combination, our findings also revealed that the ISC rate determines the phosphorescence efficiency in these molecules.

6.6. References

1. Tang, C. W.; VanSlyke, S. A. *Appl. Phys. Lett*. **1987**, *51*, 913.
2. Baldo, M. A.; O'Brien, D. F.; You, Y.; Shoustikov, A.; Sibley, S.; Thompson, M. E.; Forrest, S. R. *Nature* **1998**, *395*, 151.
3. Adachi, C.; Baldo, M. A.; Forrest, S. R.; Thompson, M. E. *Appl. Phys. Lett.* **2000**, *77*, 904.
4. You, Y.; Han, Y.; Lee, Y.-M.; Park, S. Y.; Nam, W.; Lippard, S. J. *J. Am. Chem. Soc*. **2011**, *133*, 11488.

5. Kawamura, Y.; Yanagida, S.; Forrest, S. R. *J. Appl. Phys*. **2002**, *92*, 87.
6. Sivasubramaniam, V.; Brodkorb, F.; Hanning, S.; Loebl, H. P.; Elsbergen, V.; Boerner, H.; Scherf, U.; Kreyenschmidt, M. *J. Fluor. Chem.* **2009**, *130*, 640.
7. Turro, N. J. *Modern Molecular Photochemistry*, University Science Books, Sausalito, CA, **1991**.
8. Kohler, A.; Wilson, J. S.; Friend, R. H. *Adv. Mater*. **2002**, *14*, 701.
9. Kiritani, M.; Yoshii, T.; Hirota, N.; Baba, M. *J. Chem. Phys*. **1994**, *98*, 11265.
10. Kahr, B.; Gurney, R. W. *Chem. Rev*. **2001**, *101*, 893.
11. Love, L. J. C.; Skrilec, M.; Habarta, J. G. *Anal. Chem*. **1980**, *52*, 754.
12. Schulman, E. M.; Walling, C. *Science* **1972**, *178*, 53.
13. Mitchell, C. A.; Gurney, R. W.; Jang, S.-H.; Kahr, B. *J. Am. Chem. Soc*. **1998**, *120*, 9726.
14. Kabe, R.; Lynch, V. M.; Anzenbacher Jr. P. *CrystEngComm* **2011**, *13*, 5423.
15. Yuan, W. Z.; Shen, X. Y.; Zhao, H.; Lam, J. W. Y.; Tang, L.; Lu, P.; Wang, C.; Liu, Y.; Wang, Z.; Zheng, Q.; Sun, J. Z.; Ma, Y.; Tang, B. Z. *J. Phys. Chem. C* **2010**, *114*, 6090−6099.
16. Maity, S. K.; Bera, S.; Paikar, A.; Pramanik, A.; Haldar, D. *Chem. Commun*. **2013**, *49*, 9051.
17. Bolton, O.; Lee, K.; Kim, H.-J.; Lin, K. Y.; Kim, J. *Nat. Chem*. **2011**, *3*, 205−210.
18. Gahlaut, R.; Joshi, H. C.; Joshi, N. K.; Pandey, N.; Arora, P.; Rautela, R.; Suyal, K.; Pant, S. *J. Lumin*. **2013**, *138*, 122.
19. Yong, G.; She, W.; Zhang, Y. *Dye Pigment* **2012**, *95*, 161.
20. Al-Attar, H. A.; Monkman, A. P. *Adv. Funct. Mater*. **2012**, *22*, 3824.

21. Lee, D; Bolton, O.; Kim, B. C.; Youk, J. H.; Takayama, S.; Kim, J. *J. Am. Chem. Soc*. **2013**, *135*, 6325.
22. Kwon, M. S.; Lee, D.; Seo, S.; Jung, J.; Kim, J. *Angew. Chem. Int. Ed*. **2014**, *53*, 11177.
23. Hirata, S.; Totani, K.; Zhang, J.; Yamashita, T.; Kaji, H.; Marder, S. R.; Watanabe, T.; Adachi, C. *Adv. Funct. Mater*. **2013**, *23*, 3386.
24. Rogers, J. E.; Cooper, T. M.; Fleitz, P. A.; Glass, D. J.; McLean, D. G. *J. Phys. Chem. A* **2002**, *106*, 10108.
25. Jones, S. C.; Coropceanu, V.; Barlow, S.; Kinnibrugh, T.; Timofeeva, T.; Bredas, J.-L.; Marder, S. R. *J. Am. Chem. Soc*. **2004**, *126*, 11782.
26. Zhao, J.; Wu, W.; Sun, J.; Guo, S. *Chem. Soc. Rev*. **2013**, *42*, 5323.
27. Chen, Y.-L.; Li, S.-W.; Chi, Y.; Cheng, Y.-M.; Pu, S.-C.; Yeh, Y.-S.; Chou, P.-T. *ChemPhysChem*. **2005**, *6*, 2012.
28. Beljonne, D.; Shuai, Z.; Pourtois, G.; Bredas, J. L. *J. Phys. Chem. A*. **2001**, *105*, 3899.
29. Lin, S. H.; Chang, C. H.; Liang, K. K.; Chang, R.; Shiu, Y. J.; Zhang, J. M.; Yang, T. S.; Hayashi, M.; Hsu, F. C. *Adv. Chem. Phys.* **2002**, *121*, 1.
30. Peng, Q.; Niu, Y.; Shi, Q. *J. Chem. Theory Comput.* **2013**, *9*, 1132.
31. Nan, G.; Yang, X.; Wang, L.; Shuai, Z.; Zhao, Y. *Physical Review B* **2009**, *79*, 115203.
32. Wang, L.; Li, Q.; Shuai, Z.; Chen, L.; Shi, Q. *Phys. Chem. Chem. Phys.* **2010**, *12*, 3309.

33. Frisch, M. J.; Trucks, G. W.; Schlegel, H. B.; Scuseria, G. E.; Robb, M. A.; Cheeseman, J. R.; Scalmani, G.; Barone, V.; Mennucci, B.; Petersson, G. A.; Nakatsuji, H.; Caricato, M.; Li, X.; Hratchian, H. P.; Izmaylov, A. F.; Bloino, J.; Zheng, G.; Sonnenberg, J. L.; Hada, M.; Ehara, M.; Toyota, K.; Fukuda, R.; Hasegawa, J.; Ishida, M.; Nakajima, T.; Honda, Y.; Kitao, O.; Nakai, H.; Vreven, T.; Montgomery Jr., J. A.; Peralta, J. E.; Ogliaro, F.; Bearpark, M.; Heyd, J. J.; Brothers, E.; Kudin, K. N.; Staroverov, V. N.; Kobayashi, R.; Normand, J.; Raghavachari, K.; Rendell, A.; Burant, J. C.; Iyengar, S. S.; Tomasi, J.; Cossi, M.; Rega, N.; Millam, N. J.; Klene, M.; Knox, J. E.; Cross, J. B.; Bakken, V.; Adamo, C.; Jaramillo, J.; Gomperts, R.; Stratmann, R. E.; Yazyev, O.; Austin, A. J.; Cammi, R.; Pomelli, C.; Ochterski, J. W.; Martin, R. L.; Morokuma, K.; Zakrzewski, V. G.; Voth, G. A.; Salvador, P.; Dannenberg, J. J.; Dapprich, S.; Daniels, A. D.; Farkas, Ö.; Foresman, J. B.; Ortiz, J. V.; Cioslowsk, J.; Fox, D. J. *Gaussian 09, Revision A.02*, Gaussian, Inc., Wallingford CT, **2009**.
34. Lu, T.; Chen, F. *J. Comp. Chem.* **2012**, *33*, 580.
35. Lu, T.; Chen, F. *J. Mol. Graph. Model.* **2012**, *38*, 314.
36. Reimers, J. R. *J. Chem. Phys.* **2001**, *115*, 9103.
37. Dalton, a molecular electronic structure program, Release DALTON2013.0 **2013**, http://daltonprogram.org.
38. Jansson, E.; Minaev, B.; Schrader, S.; Ågren, H. *Chem. Phys.* **2007**, *333*, 157.

CHAPTER 7

High Thermal Conductivity in Amorphous Polymer Blends by Engineered Interchain Interactions

This chapter describes one of the important but has been neglected engineering properties of polymers, thermal conductivity (*k*). Polymers are 1-dimensional molecules and the major force holding polymers in bulk objects and thin films is weak Van der Waals force. Therefore, thermal energy cannot efficiently transport through polymer matrix due to the loosely bound intermolecular packing structure. Accordingly thermal conductivity of polymers is rather low due to resulting heat dissipation through various vibrational modes. Conventionally in order to obtain high thermal conductivity, high *k* fillers such as ceramic or metal particle have been blended into polymer matrix about their percolation threshold. However, this strategy also significantly alters other properties such as optical, electrical, and mechanical properties. In this chapter, high thermal conductivity in thin (up to 70 nm) amorphous polymer films is investigated by incorporating hydrogen bonding and its homogeneous distribution between two polymers. Thermal conductivity up to 1.5 $Wm^{-1}K^{-1}$ has been achieved, which is an order of magnitude higher than conventional polymers.

Parts of this chapter appear in: Kim*, G.-H; Lee*, D.; Shanker*, A.; Shao, L.; Kwon, M. S.; Gidley, D.; Kim, J.; Pipe, K. P. *Nature Materials* **2014**, in press.

7.1. Introduction

Thermal conductivity is an important property for polymers, since it often affects product reliability (e.g., electronics packaging), functionality (e.g., thermal interface materials), and/or manufacturing cost[1]. However, polymer thermal conductivities primarily fall within a relatively narrow range (0.1 – 0.5 $Wm^{-1}K^{-1}$) and are largely unexplored. Here, we show that a blend of two polymers with high miscibility and appropriately chosen linker structure can yield a dense and homogeneously distributed thermal network. A sharp increase in cross-plane thermal conductivity is observed under these conditions, reaching over 1.5 $Wm^{-1}K^{-1}$ in typical spin-cast polymer blend nanoscale films, which is approximately an order of magnitude larger than that of other amorphous polymers.

A common method to enhance a polymer's thermal conductivity (κ) is to blend it with high-κ fillers such as metal[2] or ceramic[3] particles, yielding reported values of κ that range from 1 to 10 $Wm^{-1}K^{-1}$.[2,3] However, the large amount of fillers required to exceed the percolation threshold can not only significantly increase the material cost (e.g., nylon6,6: \$2/kg vs. alumina particles: \$100/kg) but may also change other important characteristics such as electrical and optical properties. Alignment of polymer chains[4-7] has been another route explored to realize high κ in polymers, although these high values of κ are limited to the direction of chain orientation and require certain fabrication techniques (e.g., electrospinning[4], nanoscale templating[5], mechanical stretching[8]). For practical applications, high-κ polymers that are more compatible with conventional manufacturing processes (e.g., solution casting) are desired, yet no such materials with κ>0.6 $Wm^{-1}K^{-1}$ have been reported without the aid of high-κ fillers.

The underlying mechanisms of thermal conductivity in amorphous materials are not completely understood, with separate studies indicating important contributions to heat transfer by the diffusion of energy through non-propagating vibrational modes[9,10], the anharmonic coupling of localized modes[11], and the ballistic propagation of delocalized modes[12]. In polymer systems, high κ measured in aligned systems[4-7] suggests much more efficient heat transfer along a covalently bonded chain, compared with interchain heat transfer via weak van der Waals (VDW) bonds. Increasing the strength of a molecular bond has been shown to improve its thermal conductance in a nanomolecular monolayer[13]; improvements in interchain thermal conductance may likewise contribute to improvements in bulk polymer thermal conductivity. However, interchain bond strength alone does not dictate κ in bulk polymers, as evidenced by miniscule improvements in κ for cross-linked polymers[14] as well as low values of κ for numerous polymers capable of strong hydrogen bonding (e.g., nylon6,6: 0.25 $Wm^{-1}K^{-1}$)[15]. Rather, maximizing interchain thermal conductance in a bulk polymeric material requires that strong intermolecular bonds used to replace weak VDW interactions must connect as closely as possible to the polymer backbones through a low-mass and short chemical linker. Furthermore, it is critical that a homogeneous distribution of these bonds is achieved at a concentration above the percolation threshold in order to form a continuous thermal network (Figure 7.1a).

Hydrogen bonding (H-bonding) is approximately 10 to 100 times stronger than the VDW interaction.[16] There are numerous available H-bonding capable moieties and linker units, allowing sufficient design flexibility to investigate thermally conductive interchain connections. In order to achieve a large number of interpolymer H-bonds in a bulk film, the H-bond donating and accepting polymers should have high number densities of H-bond capable moieties. To realize a uniform and homogeneous distribution of H-bonds, the H-bond accepting and donating polymers are required to be not only homogeneously dispersed but also miscible at the molecular level to allow polymers to intertwine within the radius of gyration[17].

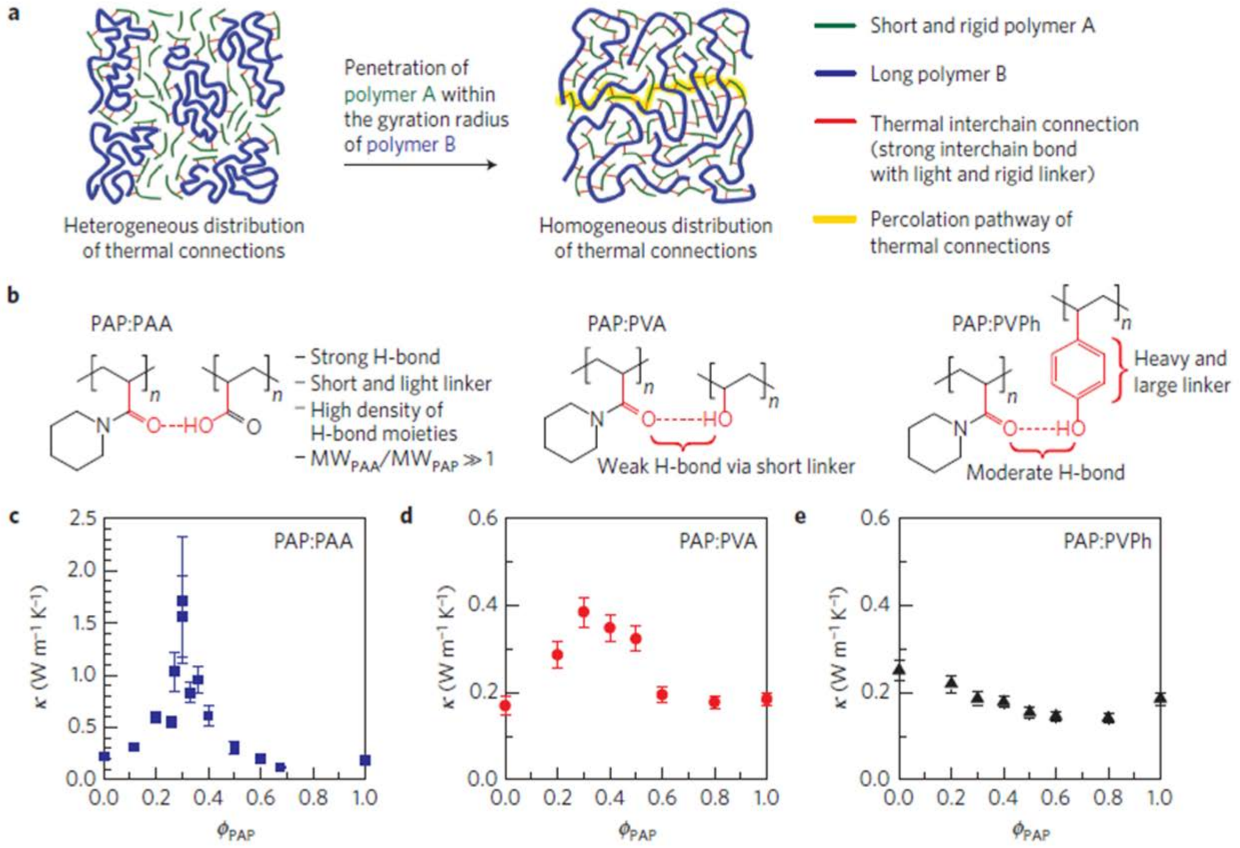

Figure 7.1. **High thermal conductivity in amorphous polymer blends by engineered interchain interactions**. a) Illustrations of heterogeneous (left) and homogeneous (right) distributions of thermally conductive interchain connections at the same concentration of H-bonding moieties, showing how the homogeneity of the bonding distribution can affect the formation of percolating thermal pathways. The relatively short and rigid polymer A penetrates within the gyration radius of a longer polymer B[31] and holds it in an extended conformation by means of strong interchain bonds, improving both intrachain and interchain heat transfer. b) Polymer pairs designed to exhibit interchain H-bonding (dashed lines). The –OH group is closely connected to the main chain for PAA and PVA, whereas it is attached to the backbone via a benzene ring linker for PVPh. The molecular weights (MWs) of PAP, PAA, PVA and PVPh as synthesized were 58,000, 450,000, 10,000 and 25,000 gmol^{-1}, respectively. Measured thermal conductivities of spin-cast PAP:PAA (c), PAP:PVA (d) and PAP:PVPh (e) films at various monomer mole fractions of PAP (ϕ_{PAP}). Error bars were estimated based on uncertainties associated with the film thickness, the temperature coefficient of electrical resistance for the heater, and the heater width.

7.2. Experimental Section

1 wt % of PAP, PAA, PVA, and PVPh were separately dissolved in DMF. Solutions of PAA, PVA, and PVPh were then separately mixed with the PAP solution. The mixture ratio (i.e., ϕ_{PAP}) was calculated as (# PAP monomers) / (# PAP monomers + # H-bond donating monomers). DMF was chosen as a solvent to avoid polymer aggregation due to strong H-bonding between the two polymers, thereby helping PAP and H-bonding donating polymers to homogeneously distribute in the 1 wt % solution. The mixed solutions at various ϕ_{PAP} were spin-cast on a pre-cleaned silicon substrate at 1500 rpm for 30 s. The spin-cast films were thermally annealed at 150 ˚C for 15 min, and kept in a vacuum chamber for 30 min. The spin-casting and thermal annealing steps were performed in nitrogen gas. Part of the spin-cast film was removed by a steel blade; the residual discontinuous film in this area was then further removed by a swab soaked in acetone and isopropanol subsequently, resulting in a shiny substrate surface with no polymer residuals. Thin metal lines were patterned using photolithography (width: 2–4 µm) or shadow-masking (50 µm), and deposited by electron-beam deposition (5 nm thick Ti / 300 nm thick Au) simultaneously on both sample and reference regions.

κ in the spin-cast polymer films was measured using conventional differential 3ω method in ambient condition. Three different sample configurations with varied interfaces and heater widths were used to ensure reliable differential 3ω measurement and thermal conductivity data. The thicknesses of the spin-cast films were measured by three methods: surface profilometry (Dektak XT), ellipsometry (Woollam M-2000DI ellipsometer), and AFM (Bruker ICON). FTIR was performed by a Nicolet 6700 spectrometer at a grazing angle of 85˚. Glass transitions of PAP:PAA at various ϕ_{PAP} were studied based on DSC curves measured under nitrogen gas by a TA Instruments Discovery Series DSC. Temperature dependent κ was measured using a Janis

VPF-100 cryostat chamber. Grazing-incidence small angle (GISAXS) and wide angle (GIWAXS) X-ray scattering measurements for spin-cast PAP:PAA thin films were carried out on a Rigaku Rotating Anode X-Ray Diffractometer (X-ray wavelength: 1.54 Å). PALS data for PAP:PAA and PAP:PVPh blends were acquired with a focused positron beam using a positron implantation energy of 1.2 keV. Tapping-mode AFM (Bruker ICON) was used to simultaneously obtain topography and phase shift images using the same tip and measurement settings.

7.3. Results and Discussion

We systematically investigated these hypotheses using rationally designed polymer pairs in which the H-bond acceptor polymer is fixed (poly(acryloyl piperidine) (PAP)) while the H-bonding donor polymer is varied (poly(acrylic acid) (PAA), poly(vinyl alcohol) (PVA), or poly(4-vinyl phenol) (PVPh)) to examine the effects of several different H-bonding strategies on κ (Figure 7.1b). PAP has a strong H-bond accepting amide functional group as a side chain on every other carbon atom along its backbone, allowing a direct thermal connection to its backbone. Its piperidine ring is expected to make its backbone rigid[18] and promote extended conformation for polymers with which it interacts through strong H-bonds (Figure 7.1a). PAA, PVPh, and PVA each have an H-bond donating –OH group associated with every other carbon atom along their backbones; however, they differ both in how the –OH group attaches to the polymer backbone and in the H-bond donating power of the –OH group. The high acidity of the carboxylic acid (–COOH) in PAA and the phenol (–PhOH) in PVPh gives its –OH groups a stronger H-bond donating power than the –OH groups in PVA. While the –OH is directly connected to the backbone in PAA and PVA, it is linked to the backbone via a benzene ring in PVPh.

As discussed in detail below, certain blends of PAP:PAA yielded an exceptionally homogeneous distribution of strong H-bonds at a concentration that exceeded the percolation threshold. For these blends, κ was measured to be greater than 1.5 $Wm^{-1}K^{-1}$, which is nearly an order of magnitude larger than that of its constituent components, PAP (0.19 ± 0.02 $Wm^{-1}K^{-1}$) and PAA (0.22 ± 0.02 $Wm^{-1}K^{-1}$) (Figure 7.1c).

To fabricate films for measurement, the H-bond accepting PAP was dissolved in *N,N*-dimethylformamide (DMF) and mixed with DMF solutions of H-bond donating PAA, PVA, or PVPh in such a way that various mole ratios of the donor (–OH) and acceptor (=N–C=O) moieties could be formed, allowing control of the H-bonding concentration in the blend films.

To characterize H-bonding and species miscibility, Fourier transform infrared (FTIR) spectroscopy and differential scanning calorimetry (DSC) were employed, both of which are standard analytical tools commonly used for these purposes[16,17]. As can be seen in Figure 7.2a, the shift of the carbonyl (C=O) stretching band in PAP due to H-bond formation is the largest in PAP:PAA (45 cm^{-1}), modest in PAP:PVPh (33 cm^{-1}), and small in PAP:PVA (2 cm^{-1}), consistent with their reported H-bond strengths[16]. These relative H-bond strengths are further confirmed by the peak shift due to –OH single bond stretching, which is the largest in PAP:PAA (500–1000 cm^{-1}) and similar in PAP:PVPh (200–350 cm^{-1}) and PAP:PVA (210 cm^{-1}). Notably, the glass transition temperature (T_g) of PAP:PAA was observed to greatly increase for blends near a PAP monomer mole ratio (ϕ_{PAP} = number of PAP monomers / number of PAP monomers and H-bond donating monomers) of 0.3 (Figure 7.2b), indicating exceptionally strong H-bonding between PAP and PAA at that ratio. In fact, the observed 48 ˚C increase for $\phi_{PAP} = 0.3$ (where $T_g = 158$ ˚C) relative to the theoretical value of 110 ˚C predicted by the Flory-Fox equation is extraordinary among polymer blends in the literature[19,20].

Cross-plane thermal conductivities (perpendicular to the centrifugal force during spin-casting) of the polymer films were measured by the differential 3ω method, which extracts an induced temperature rise across a layer of interest that can have a thickness as small as several nanometers[21-24]. Figures 1c-e summarizes the measured thermal conductivities of PAP blend films with PAA, PVA, or PVPh at various ϕ_{PAP}. While PAP:PVA shows a trend of increased similar to PAP:PAA, its thermal conductivity gain is much smaller ($\kappa_{\max}$ = 0.38±0.04 $\mathrm{Wm^{-1}K^{-1}}$), consistent with its weaker H-bond strength.

In contrast, the thermal conductivity of PAP:PVPh, which forms stronger H-bonds than PAP:PVA, shows no enhancement relative to values for the pure PAP and PVPh constituents. As discussed in more detail below, we attribute this in part to the fact that the H-bond donating hydroxyl group does not attach directly to the PVPh backbone but rather via a benzene ring as a linker, similar to cross-linked polystyrene[25].

The maximum measured κ of PAP:PAA is much larger than that of conventional cross-linked[14] or H-bond forming polymers (e.g., nylon6,6: κ = 0.25 $\mathrm{Wm^{-1}K^{-1}}$)[15]. In our derivation of κ, we assumed that interfacial thermal resistances were negligible compared to the film thermal resistance; the derived κ therefore represents a lower bound for the film thermal conductivity[26]. For pure PAP and pure PAA, the underestimation of κ is estimated to be 5% using interfacial thermal resistances previously measured for similar interfaces[13,26,27]. Comparisons between the film thicknesses used and the polymers' radii of gyration do not indicate a contribution of reduced thermal boundary resistance[28] to the measured thermal conductivity enhancements.

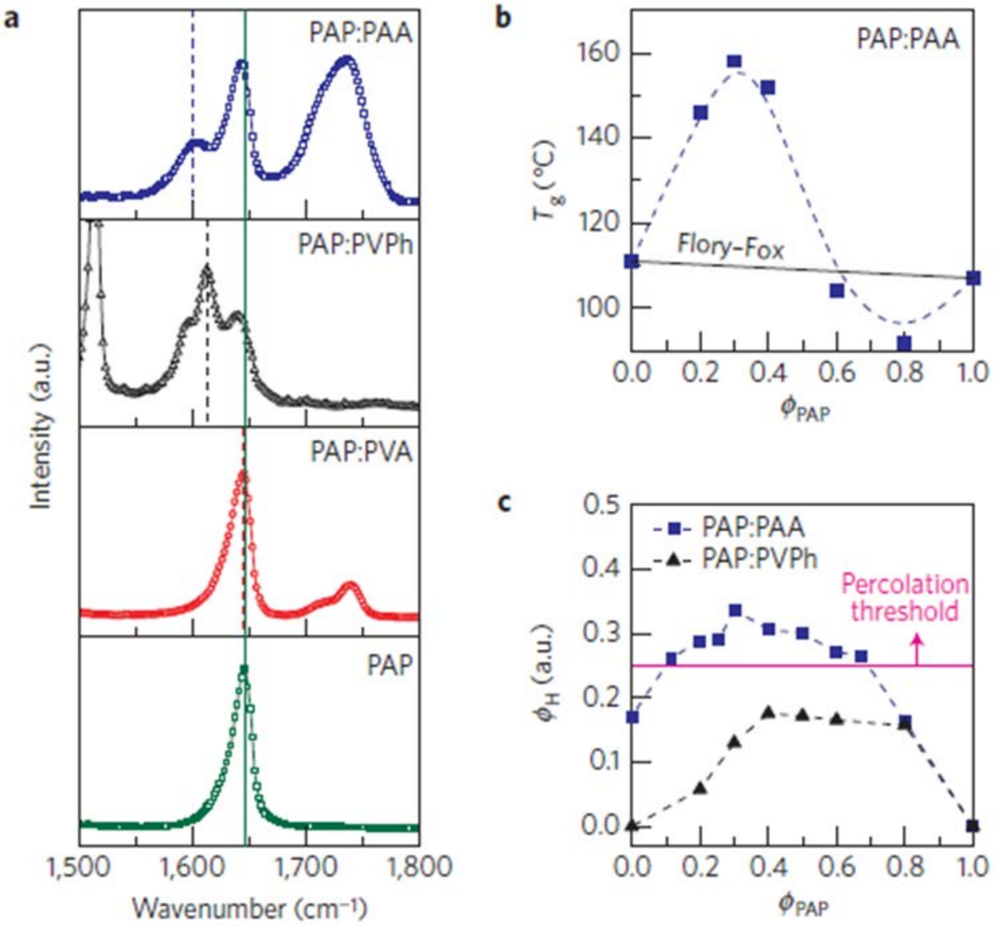

Figure 7.2. **Comparison of H-bond strengths in PAP:PAA, PAP:PVA and PAP:PVPh**. a) FTIR spectroscopy data for PAP:PAA, PAP:PVPh and PAP:PVA at ϕ_{PAP} = 0.3. The peak at 1,645 cm^{-1} (solid line) corresponds to PAP carbonyl stretching in the absence of H-bonding, whereas the dashed lines indicate peak locations for carbonyl stretching in H-bonded PAP (1,604 cm^{-1} for PAP:PAA, 1,612 cm^{-1} for PAP:PVPh, and 1,643 cm^{-1} for PAP:PVA). The relatively large peak shift for carbonyl stretching in PAP:PAA implies that its H-bond strength is the largest among the three pairs. b) Glass transition temperatures (T_g) measured for PAP:PAA at various ϕ_{PAP}, indicating extraordinarily strong H-bonding for $\phi_{PAP} \approx 0.3$. The solid line indicates T_g as predicted by the Flory–Fox equation, with the dashed line drawn to illustrate the data trend. c) Fraction of H-bonded monomer unit (ϕ_H) in PAP:PAA and PAP:PVPh as calculated by areal integrations of the deconvoluted H-bonded and pristine carbonyl stretching bands shown in a. Also shown is the bonding percolation threshold for a simple cubic lattice (solid line)[29].

As shown in Figure 7.3a, κ in PAP:PAA at ϕ_{PAP} = 0.3 increases with T, which is consistent with amorphous character (Figure 7.3b). Note that the crystalline PE fiber data shown in Figure 7.3a exhibits a strong negative temperature dependence, indicating that the anharmonic scattering of acoustic modes dominates.[6] The small $d\kappa/dT$ for ϕ_{PAP} = 0.3 relative to that for ϕ_{PAP} = 0.7 may indicate a lesser contribution of localized vibrational modes[11] as weak VDW bonds are replaced by a homogeneous network of strong H-bonds with less acoustic contrast relative to the backbone covalent bonds. As discussed below, this network has a concentration greater than the percolation threshold as evidenced by FTIR (Figure 7.2c) and a homogeneous distribution as evidenced by glass transition data (Figures 7.3e, 7.3f) and exceptionally smooth atomic force microscopy (AFM) phase data (Figure 7.4). Positronium annihilation lifetime spectroscopy (PALS) data shown in Figure 7.3c indicates a smooth change in mass density between pure PAA and pure PAP, with no anomalies present that would suggest a density-related contribution to the sharply-peaked increase in κ near ϕ_{PAP} = 0.3.

The fraction of intermolecular bonds that are H-bonds (ϕ_H) in PAP:PAA was estimated from the areal ratio of H-bond bands to pristine carbonyl stretching bands in FTIR data (Figure 7.4). We note that a certain number of H-bonds in PAP:PAA are self-associated within PAA (Figure 7.4c). Accounting for the fact that PAP cannot form H-bonds with these self-associated PAA units, the largest number of H-bonds between PAP and PAA is expected to occur at ϕ_{PAP} = 0.33, which is close to the observed maximum shown in Figure 7.2c at ϕ_{PAP} = 0.3. For this blend, ϕ_H reaches 0.34, which is greater than the bonding percolation threshold for a simple cubic lattice (0.25)[29].

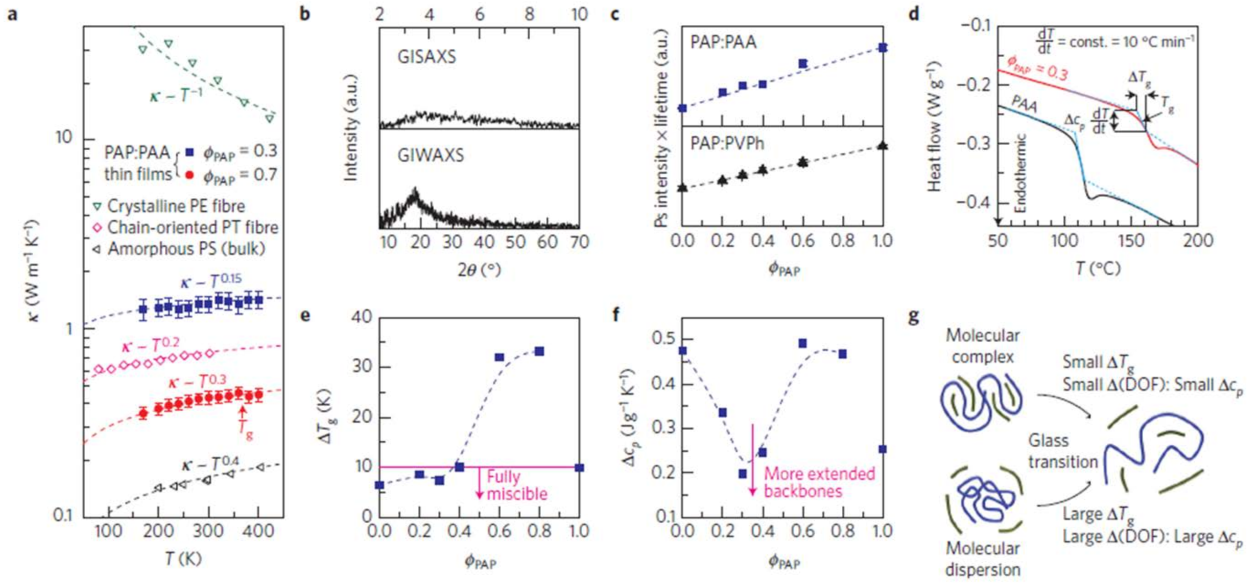

Figure 7.3. **Thermal and structural properties of PAP:PAA**. a) $\kappa(T)$ in PAP:PAA at ϕ_{PAP} = 0.3 and 0.7 (closed symbols), compared with $\kappa(T)$ in other crystalline (polyethylene6 (PE)) and amorphous (polythiophene[5] (PT), polystyrene[34] (PS)) polymers (open symbols). Dashed lines represent T^x. b) Grazing-incidence small- and wide-angle X-ray scattering (GISAXS, GIWAXS) data for a PAP:PAA spin-cast film at ϕ_{PAP} = 0.3, suggesting the absence of short- and long-range order, respectively. We note that the broad peak observed in GIWAXS, known as an amorphous halo, is characteristic of amorphous materials. c) Positronium annihilation lifetime spectroscopy data for PAP:PAA and PAP:PVPh blends at various ϕ_{PAP}. The product of positronium (P_s) intensity and lifetime increases monotonically with ϕ_{PAP} for both blends, indicating a smooth change in density. Dashed lines are linear fits. d) Differential scanning calorimetry (DSC) data for PAP:PAA at various ϕ_{PAP}. T_g was set to the middle point of the solid line that connects two asymptotic dashed lines. Glass transition width (ΔT_g) (e) and change in specific heat capacity during glass transition (Δc_p) (f) for PAP:PAA at various ϕ_{PAP}. Polymer blends with ΔT_g less than 10 °C are fully miscible, whereas those with ΔT_g greater than 32 °C approach immiscibility[17]. Blends with larger Δc_p experience greater changes in their molecular degrees of freedom (DOF), indicating a transition from an unextended to an extended conformation. Dashed lines were drawn to illustrate the data trend. g) Illustration of glass transitions in polymer blends with different degrees of miscibility and entanglement.

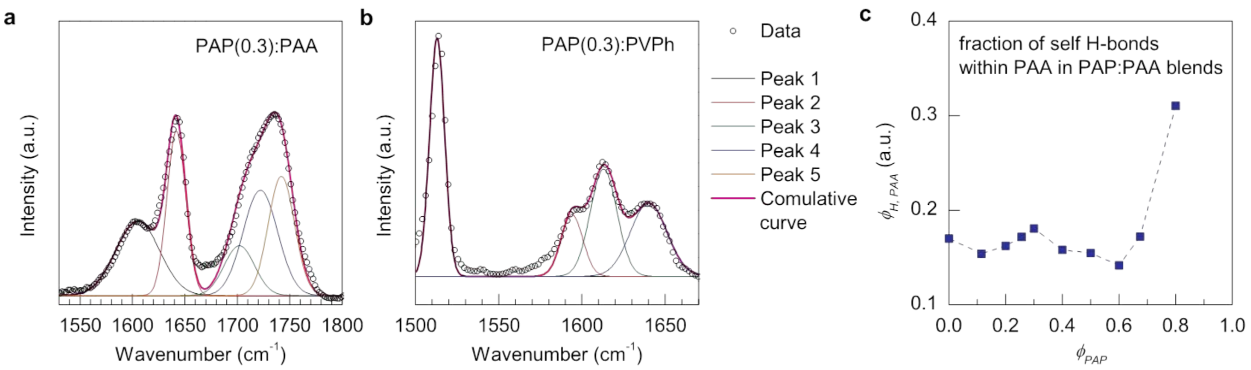

Figure 7.4. **Representative FTIR spectra with deconvoluted peaks.** a) FTIR spectrum of PAP(0.3):PAA. C=O stretching peaks occur in H-bonded PAP (Peak 1, 1602 cm^{-1}), non H-bonded PAP (Peak 2, 1642 cm^{-1}), self-associated H-bonded PAA (Peak 3, 1702 cm^{-1}), pristine PAA (Peak 4, 1720 cm^{-1}), and PAA H-bonded with PAP (Peak 5, 1742 cm^{-1}). b) FTIR spectrum of PAP(0.3):PVPh. C=C stretching peaks corresponding to the PVPh benzene ring occur at 1513 cm^{-1} (Peak 1), 1596 cm^{-1} (Peak 2), and 1612 cm^{-1} (Peak 3). Peak 3 at 1612 cm^{-1} overlaps with the H-bonded PAP C=O stretching peak. Peak 4 (1640 cm^{-1}) corresponds to non H-bonded PAP. c) Fraction of self-associated H-bonded units within PAA in PAP:PAA blends, obtained from the areal ratio of Peak 3 to Peak 4 in a).

The glass transition of a polymer blend provides information regarding the miscibility of its constituent polymers[17]. For all PAP:PAA mixture ratios, the glass transition was found to occur at a single temperature (T_g), indicating uniform physical dispersion of PAP and PAA. Furthermore, the temperature range over which the glass transition occurs (ΔT_g) was found to be narrow for $\phi_{PAP} \leq 0.4$ (Figure 7.3e), indicating that PAP strongly interacts and intermixes with PAA within the PAA radius of gyration for this range of blends[17]. The change in specific heat capacity during the glass transition (Δc_p) was found to considerably decrease as ϕ_{PAP} approaches 0.3 (Figure 7.3f). A primary contributor to a change in specific heat during a polymer's glass transition is a change in the degrees of freedom that occurs when a polymer transitions from a highly self-entangled state (Figure 7.3g) to a state in which the backbone is extended, as observed in polystyrene[30]. The minimum Δc_p at ϕ_{PAP} = 0.3 therefore suggests that the backbones of both PAP and PAA are mostly extended for this blend prior to the glass transition at 158 ˚C. In fact, Δc_p for PAP:PAA at $\phi_{PAP} = 0.3$ is similar to that of pure PAP but far lower than that of pure PAA, implying that the relatively rigid and short PAP chains penetrate within the PAA gyration radius and hold the flexible PAA chains in an extended state by means of strong H-bonds[31]. This extension of the PAA backbones is expected to improve intrachain heat transport similar to previous work in aligned polymers[4-7], in contrast with studies of polymers at high hydrostatic pressures in which the diffusion of energy through non-propagating vibrational modes was shown to dominate heat transfer[10].

The homogeneity of the H-bond distribution was assessed by studying phase shifts in AFM tapping mode data, which can characterize spatial variations in surface stiffness[32] and thereby distinguish regions of stiff H-bonds from regions of weaker VDW bonds[33]. Because the AFM tip interacts with soft materials longer, a negative phase shift (appearing as a dark color in the phase images of Figure 7.5a) represents a VDW-rich region, while a positive phase shift (appearing as a bright color) corresponds to an H-bond rich region. The phase images of PAP:PAA are observed to get smoother (i.e., exhibiting a smaller standard deviation (σ_{SDEV}) in phase) as ϕ_{PAP} approaches 0.3, the fraction at which both the maximum ϕ_H and the maximum ϕ_{PAP} are observed. Also, the mean phase shift (θ_{mean}) becomes significantly positive at $\phi_{PAP} = 0.3$, which together with low σ_{SDEV} indicates a homogeneously distributed dense network of H-bonds. As shown in Figure 7.5d, κ strongly depends on the homogeneity of the H-bond distribution (i.e., σ_{SDEV}) when ϕ_H exceeds the percolation threshold.

While T_g exceeds the Flory-Fox prediction for $\phi_{PAP} \leq 0.4$ (Figure 7.2b), indicating strong H-bonding, the fact that it is smaller than the Flory-Fox prediction for $\phi_{PAP} > 0.4$ suggests phase inversion from a PAA matrix to a PAP matrix for this high range of PAP concentrations. Reduction in T_g due to phase inversion has previously been observed[20]. Likewise, ΔT_g, Δc_p, and σ_{SDEV} become large for $\phi_{PAP} > 0.4$, suggesting heterogeneous rather than homogeneous blends of PAP and PAA; as a consequence of phase inversion, the relatively flexible PAA chains, which have a large molecular weight and large radius of gyration, do not penetrate efficiently into the matrix of smaller PAP chains, leading to heterogeneous blends. Consequently, κ in PAP:PAA did not exhibit a meaningful increase for $\phi_{PAP} > 0.4$.

Although PAP:PVPh was observed to form stronger H-bonds than PAP:PVA (Figure 7.2a), several observed features likely explain why it did not show enhanced κ. First, it has significant phase roughness, indicating a lack of homogeneity, and a large negative phase shift, indicating film softness (likely due to interference between the piperidine and benzene rings which disrupts PAP and PVPh chain conformations). Second, it has an H-bond threshold below the percolation threshold (Figure 7.2c), indicating that a continuous network of strong bonds which would contribute to thermal conductivity or film stiffness is not present. Finally, the heavy benzene ring presents a large impedance contrast to vibrational modes which transfer energy between PAP and PVPh. PALS measurements (Figure 7.3c) indicate a smooth reduction in density from pure PVPh to pure PAP, consistent with the measured decline in κ. To provide supporting evidence for the thermal properties of linker structures containing benzene, PAP mixed with poly(vinylbenzoic acid) (PVBA), which contains a benzene ring like PVPh and a strong H-bond donating carboxyl group like PAA, likewise showed only a minuscule increase in κ.

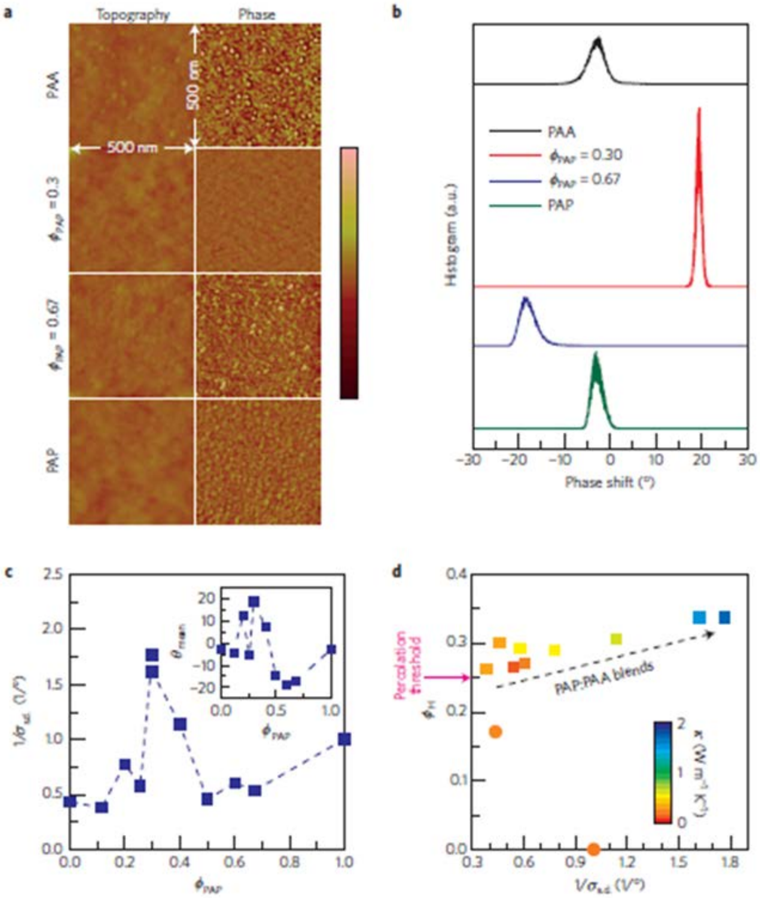

Figure 7.5. **Tapping-mode AFM data for PAP:PAA blends.** a) Topography (left) and phase (right) images having a scanning area of 500 nm × 500 nm; images were flattened (i.e., shifted to give zero mean value) for illustration purposes. The color bar ranges from -5 nm to 5 nm for topography, and from -10˚ to +10˚ for phase images. b) Histograms of AFM phase shifts for PAP:PAA blends (before flattening), normalized to have the same peak area. c) Inverse of standard deviation ($1/\sigma_{SDEV}$) of AFM phase data, indicating bonding homogeneity. Inset plots the mean phase shift (θ_{mean}), before image flattening, versus ϕ_{PAP}. PAP:PAA at ϕ_{PAP} = 0.3 has the smallest σ_{SDEV} and largest θ_{mean}, indicating a dense and homogeneously distributed network of strong H-bonds. Dashed lines were drawn for guidance. d) (color scale) of PAP:PAA (squares) as a function of σ_{SDEV} and ϕ_H (obtained from Figure 7.2c), showing its strong dependence on bonding homogeneity (i.e., $1/\sigma_{SDEV}$) above the percolation threshold, including unmixed PAP and PAA (circles).

7.4. Conclusions

In summary, large increase in κ was observed in amorphous polymers when a continuous network of thermally conductive interchain connections forms. Both the strong interchain bond and the appropriate linker structure are required to prompt thermally conductive interchain connection, while a large concentration of these thermal connections and their homogeneous distribution are essential to form a percolating network. We note that the large κ was realized in films up to 70nm thick; further optimization of materials synthesis and processing are required to scale network formation to bulk films of large thickness.

7.5. References

1. Chanda, M.; Roy, S. K. *Plastics technology handbook 4th edn*. CRC Press/Taylor & Francis Group, **2007**.
2. Mamunya, Y. P.; Davydenko, V. V.; Pissis, P.; Lebedev, E.; *Eur Polym J* **2002**, *38*, 1887-1897.
3. Wong, C. P.; Bollampally, R. S. *J. Appl. Polym. Sci*. **1999**, *74*, 3396-3403.
4. Shen, S.; Henry, A.; Tong, J.; Zheng, R. T.; Chen, G. *Nat. Nanotech*. **2010**, *5*, 251-255.
5. Singh, V. et al. *Nat. Nanotech*. **2014**, *9*, 384-390.
6. Wang, X. J.; Ho, V.; Segalman, R. A.; Cahill, D. G. *Macromolecules* **2013**, *46*, 4937-4943.
7. Kurabayashi, K.; Asheghi, M.; Touzelbaev, M.; Goodson, K. E. *J. Microelectromech S* **1999**, *8*, 180-191.
8. Choy, C. L. *Polymer* **1977**, *18*, 984-1004.
9. Allen, P. B.; Feldman, J. L.; Fabian, J.; Wooten, F. *Phil. Mag. B* **1999**, *79*, 1715-1731.

10. Hsieh, W. P. et al. *Phys. Rev. B* **2010**, *83*, 174205.
11. Shenogin, S.; Bodapati, A.; Keblinski, P.; McGaughey, A. J. H. *J. Appl. Phys*. **2009**, *105*, 034906.
12. Regner, K. T. et al. *Nat. Commun*. **2013**, *4*, 1640.
13. O'Brien, P. J. et al. *Nat. Mater*. **2013**, *12*, 118-122.
14. Yamamoto, O.; Kambe, H. *Polym. J*. **1971**, *2*, 623-628.
15. Mark, J. E. *Physical Properties of Polymers Handbook* AIP Press, **1996**.
16. Steiner, T. *Angew. Chem. Int. Ed*. **2002**, *41*, 48-76.
17. Utracki, L. A. *Polymer Blends Handbook* Kluwer Academic Publishers, **2002**.
18. Kunal, K.; Robertson, C. G.; Pawlus, S.; Hahn, S. F.; Sokolov, A. P. *Macromolecules* **2008**, *41*, 7232-7238.
19. Coleman, M. M.; Painter, P. C. *Prog. Polym. Sci*. **1995**, *20*, 1-59.
20. Lin, A. A.; Kwei, T. K.; Reiser, A. *Macromolecules* **1989**, *22*, 4112-4119.
21. Lee, S. M.; Cahill, D. G. *J. Appl. Phys*. **1997**, *81*, 2590-2595.
22. Borca-Tasciuc, T.; Kumar, A. R.; Chen, G. *Rev. Sci. Instrum*. **2001**, *72*, 2139-2147.
23. Jin, Y. S.; Shao, C.; Kieffer, J.; Pipe, K. P.; Shtein, M. *J. Appl. Phys*. **2012**, *112*, 093503.
24. Koh, Y. K. et al. *J. Appl. Phys*. **2009**, *105*, 054303.
25. Kikugawa, G.; Desai, T. G.; Keblinski, P.; Ohara, T. *J. Appl. Phys*. **2013**, *114*, 034302.
26. Losego, M. D.; Moh, L.; Arpin, K. A.; Cahill, D. G.; Braun, P. V. *Appl. Phys. Lett*. **2010**, *97*, 011908.
27. Jin, Y. et al. *Appl. Phys. Lett*. **2011**, *98*, 093305.
28. Liu, J.; Ju, S. H.; Ding, Y. F.; Yang, R. G. *Appl. Phys. Lett*. **2014**, *104*, 153110.

29. Stauffer, D.; Aharony, A. *Introduction to Percolation Theory 2nd edn*. Taylor & Francis, **1992**.

30. Rong, W. R.; Fan, Z. Y.; Yu, Y.; Bu, H. S.; Wang, M. *J. Polym. Sci. Part B: Polym. Phys*. **2005**, *43*, 2243-2251.

31. Lemstra, P. J.; Kleintjens, L. A. *Integration of Fundamental Polymer Science and Technology-2* Elsevier Applied Science, **1988**.

32. Magonov, S. N.; Elings, V.; Whangbo, M. H. *Surf. Sci*. **1997**, *375*, 385-391.

33. Podsiadlo, P. et al. *Science* **2007**, *318*, 80-83.

34. Underwood, W. M.; Taylor, J. R. *Polym. Eng. Sci*. **1978**, *18*, 556-563.

CHAPTER 8

Conclusions and Outlook

8.1. Research Summary

The main theme of my dissertation is to realize room temperature phosphorescence (RTP) in amorphous materials based on understanding of two critical processes: intersystem crossing and vibration suppression. Compared to the widely used organometallic phosphors and the recently discovered crystalline purely organic phosphors, amorphous alternatives are more promising due to the fact that they are easy to design and synthesize and are also stable under ambient operating conditions. However, realizing RTP is challenging in amorphous organic materials because they suffer from weak intersystem crossing without the aid of heavy metals and competing non-radiative decay of long-lived triplets. Therefore, it is very important to choose an efficient triplet generating phosphor to facilitate intersystem crossing as well as devise a possible way to suppress the vibrational dissipation routes. As an extended study of crystal-based phosphorescence[1], doped crystal of dibromobenzene and bromobenzaldehyde derivatives were further investigated with focus on optimizing quantum efficiency and fine-tuning emission color realized by efficient inclusion of purely organic phosphorescent emitters into host materials and replacement of halogen of the emitters, respectively, as discussed in Chapter 2.[2]

In Chapter 3, amorphous phosphorescence was first realized using glassy polymer matrix as a triplet vibration locker.[3] By embedding a purely organic phosphor, Br6A, in rigid polymer matrix like PMMA, bright RTP was achieved. Especially, isotactic PMMA provides most efficient suppression of triplet vibration due to the absence of its beta-relaxation at room temperature and allows the highest quantum yield of 7.5%. The novel amorphous phosphorescent thin films showed temperature-dependent emission property if temperature approaches to the polymer's glass transition temperature because above its T_g polymer becomes more mobile and therefore cannot provide rigid environment required for efficient vibration suppression. This feature enables it to be utilized as an optical temperature sensor integrated into microfluidic devices, which have a number of advantages such as simple structure, reversible response, and easy and economic fabrication.

A more efficient strategy to suppress triplet vibration of purely organic phosphor was demonstrated in Chapter 4.[4] Rather than using weak Van der Waals interactions between polymer matrix and purely organic phosphors as described in Chapter 3, we introduced strong hydrogen bonding by synthesizing a functionalized phosphor and choosing a new polymer having hydrogen bonding capability. In this work, phosphorescence with quantum yield as high as 24% was realized. Interestingly, modulation of hydrogen bonding by water molecules provides unique reversible phosphorescence-to-fluorescence switching behavior, which can be utilized as a ratiometric water sensor.

While most phosphors are overly sensitive to oxygen, our purely organic phosphors are stable in ambient conditions even though the origin of the stability has not been explored thoroughly. Interestingly, we found that our purely organic phosphors are sensitive to ozone, a strong oxidizing species, and revealed the origin of the ozone sensitivity and utilized the finding to develop optical ozone sensory films as described in Chapter 5.[5] Compared to conventional inorganic ozone sensors, our novel phosphorescence-based ozone sensor has numerous advantages such as high sensitivity (~ 1ppm), low cost fabrication, and by integration with polymer film it can be fabricated as a disposable and portable strip like a litmus paper.

As discussed in Chapter 1, as a triplet generating moiety, aromatic ketone cannot guarantee efficient intersystem crossing because ΔE_{ST} can be quite different depending on the molecular structures and hence unpredictable. Therefore, it is of much importance that one finds a design parameter to enhance intrinsic intersystem crossing character besides the efforts to suppress triplet vibration discussed in Chapters 3 and 4. Chapter 6 describes the effect of the extended conjugation length of organic phosphors on their phosphorescence properties at 77 K.[6] Since manipulating conjugation length of organic phosphors is a powerful tool to tune the emission color establishing an understanding on the conjugation length effects on the phosphorescent emission intensity is very meaningful. We focused on the first intersystem crossing, i.e. triplet harvesting, which is one of the key processes in phosphorescent emission. A series of bromobenzaldehydes were prepared and in order to investigate the conjugation length effects on the photophysical properties computational methods were utilized to calculate intersystem crossing rates and electron density difference between the ground states and the excited states. We revealed that phosphorescence intensity decreased with red-shifted emission as the conjugation length increased, which has more correlation with intersystem crossing rate determined by spin-orbit coupling strength rather than singlet-to-triplet energy difference.

We applied our established knowledge of intermolecular interactions like hydrogen and halogen bonding from the purely organic phosphor development to the enhancement of thermal conductivity in amorphous polymers by rationally designing hydrogen donating and accepting polymer pairs in Chapter 7.[7] High *k* filler such as ceramic or metal particle has been widely used in order to enhance polymer's thermal conductivity. However, this traditional strategy inevitably largely alters the mechanical, optical, and electrical properties of polymers in the application where these properties are crucially important. Another conventional strategy is to align polymers in order to utilize fairly good thermal conductivity along the covalently bonded polymer's main chain. However this strategy requires stringent fabrication processes and cannot provide isotropic thermal conductivity. In this work, through effective hydrogen bonding between two polymers and its homogeneous distribution high thermal conductivity up to 1.5 $Wm^{-1}K^{-1}$ in thin (up to 70 nm) amorphous polymers was achieved. The achieved high thermal conductivity is an order of magnitude higher than that of conventional polymers.

8.2. Future Considerations

Some of the topics discussed in my dissertation are worthy of further investigations. First, in amorphous organic phosphorescence, stronger intermolecular interactions than hydrogen bonding such as covalent bonding or ionic bonding can be devised in molecular design to suppress triplet vibration even more efficiently. Through further investigation of radiative and non-radiative decay kinetics with aid of computation and calculation, we may be able to establish a new molecular design principle of organic phosphors that have very efficient singlet-to-triple and triplet-to-singlet intersystem conversion and resulting vibration-insensitive property. Design of purely organic phosphors together with proper hosting molecules for electroluminescence (EL) device application would be a promising direction as an extension of my dissertation work. For that purpose, precise control of HOMO and LUMO level, providing a good conducting property, and establishing a proper thermal stability would be critically important.

8.3. References

1. Bolton, O.; Lee, K.; Kim, H.-J.; Lin, K. Y.; Kim, J. *Nat. Chem*. **2011**, 3, 205-210.
2. Bolton, O.; Lee, D.; Jung, J.; Kim, J. *Chem. Mater*. **2014**, in press.
3. Lee, D.; Bolton, O.; Kim, B. C.; Youk, J. H.; Takayama, S.; Kim, J. *J. Am. Chem. Soc*. **2013**, 135, 6325-6329.
4. Kwon, M. S.; Lee, D.; Seo, S.; Jung, J.; Kim, J. *Angew. Chem. Int. Ed*. **2014**, 53, 11177-11181.
5. Lee, D.; Jung, J.; Bilby, D.; Kwon, M. S.; Yun, J.; Kim, J. submitted.
6. Lee, D.; Ma, X.; Jeong, E. J.; Hashemi, H.; Kieffer, J.; Kim, J. submitted.
7. Kim, G.-H; Lee, D.; Shanker, A.; Shao, L.; Kwon, M. S.; Gidley, D.; Kim, J.; Pipe, K. P. *Nature Materials* **2014**, in press.